5-2016

Development of a Reactor Physics Analysis Procedure for the Plank-Based and Liquid Salt-Cooled Advanced High Temperature Reactor

Cole Andrew Gentry
University of Tennessee - Knoxville, Cole-Gentry@utc.edu

Recommended Citation

Gentry, Cole Andrew, "Development of a Reactor Physics Analysis Procedure for the Plank-Based and Liquid Salt-Cooled Advanced High Temperature Reactor. " PhD diss., University of Tennessee, 2016.
https://trace.tennessee.edu/utk_graddiss/3695

To the Graduate Council:

I am submitting herewith a dissertation written by Cole Andrew Gentry entitled "Development of a Reactor Physics Analysis Procedure for the Plank-Based and Liquid Salt-Cooled Advanced High Temperature Reactor." I have examined the final electronic copy of this dissertation for form and content and recommend that it be accepted in partial fulfillment of the requirements for the degree of Doctor of Philosophy, with a major in Nuclear Engineering.

G. Ivan Maldonado, Major Professor

We have read this dissertation and recommend its acceptance:

Jess C. Gehin, Ronald E. Pevey, Robert Grzywacz

Accepted for the Council:
Dixie L. Thompson

Vice Provost and Dean of the Graduate School

(Original signatures are on file with official student records.)

Development of a Reactor Physics Analysis Procedure for the Plank-Based and Liquid Salt-Cooled Advanced High Temperature Reactor

A Dissertation Presented for the
Doctor of Philosophy
Degree
The University of Tennessee, Knoxville

Cole Andrew Gentry
May 2016

Dedication

To my friends and family for their love and support throughout this exciting endeavor. And especially to my wife Ashley, for her reassurance during the struggles, for her patience during the long nights, for the blessing that is our wonderful son, and for her love.

Acknowledgements

Over the course of my research I have received considerable support from a number of individuals which I would like to recognized. I would like to thank Dr. Ivan Maldonado and Dr. Kang Seog Kim for providing their guidance and support throughout the entirety of this project. Also, I thank the other committee members, Dr. Jess Gehin, Dr. Ronald Pevey, and Dr. Robert Grzywacz for their time and involvement in the completion of this work. I would like to acknowledge Nicholas Luciano and Dr. Keith Ottinger for their amazing help with NESTLE, as well as Dr. Jaakko Leppänen for his exemplary support of SERPENT. Lastly, I would like to thank Dr. Ondrej Chvala for his support with our computing resources and for his inexhaustible patience with my cluster issues.

Some of the work performed in this project was funded by the US Department of Energy under the Nuclear Energy University Program (NEUP) Project 12-3870, under Prime Contract No. DE-AC07-05ID14517. Project Titled: "Fuel and Core Design Options to Overcome the Heavy Metal Loading Limit and Improve Performance and Safety of Liquid Salt Cooled Reactors." The support provided by Dr. Bojan Petrovic and his team at the Georgia Institute of Technology under this grant is kindly appreciated.

Abstract

Presented in this dissertation is the investigation and development of an adapted lattice physics-to-core simulator two-step procedure based on the SERPENT 2 and NESTLE neutronics codes for the rapid analysis of the Advanced High Temperature Reactor (AHTR). AHTR specific characteristics, such as its longer neutron diffusion length and double heterogeneity of TRISO fuel particles, were taken into consideration when adapting the traditional Light Water Reactor (LWR) lattice to nodal diffusion procedure to AHTR applications. The coarse energy group structure was re-optimized from the traditional LWR 2-group structure to an alternative 4-group structures to address the AHTR specific flux spectrum and neutronics characteristics. A more accurate treatment of the interface between fuel and reflector was implemented using simplified 1-D models along with the application of an Equivalence Theory based Assembly Discontinuity Factor (ADF) adjustment of the resultant few group constants. A similar ADF adjustment was also applied to treat the insertion of control blades to properly account for inter-assembly leakage. The developed two-step procedure was tested against multiple transport based high fidelity reference benchmark models and was deemed to provide reasonably accurate results, with the exception of some peripheral radial power discrepancies which have been attributed to the inadequacy of the 1-D radial reflector model to capture a 1/3 symmetric and cyclic power tilt unique to the AHTR fuel assembly design and core layout. For 2-D and 3-D full core models, eigenvalue agreement was within 130 pcm and power distribution errors within 3.5% Root Mean Squared (RMS) error. The final implementation of this two-step procedure was used to perform a representative neutronic and thermal hydraulic coupled simulation which demonstrated the ability of the developed procedure to perform 3-D full core neutronics calculations with coupling to thermal hydraulic feedback in an extremely expedient manner. This work paves the way to ultimately performing fuel cycle, core / assembly design, and safety margin assessments for the AHTR. Additionally, this procedure greatly reduces the computational expense of performing such simulations and opens the door toward AHTR design optimization.

Table of Contents

List of Tables

List of Figures

1. Introduction and General Information

The Advanced High Temperature Reactor (AHTR) is a Generation IV molten salt cooled solid fuel form reactor design, recommended for its distinct advantages of high operational temperature, low operational pressure, and fuel reliability / fission product retention [1]. Preliminary neutronic and core characteristic analyses of this reactor design have been demonstrated with Monte Carlo based core models. However, these models are computationally expensive and not conducive for design optimization studies or direct coupling to thermal hydraulics models for capturing thermal feedback effects [1,2]. As such, it is then necessary to develop a computationally expedient modeling method to provide a means for improved safety and economics analysis. The conventional two-step procedure utilized for modeling Light Water Reactors (LWRs)), which employs deterministic transport theory based “lattice physics” to generate assembly-homogenized and few energy group collapsed cross sections for use in advanced 3-D nodal diffusion simulators [3-5], furnishes a reference approach from which to base a new more efficient modeling method for the AHTR. However, differences between LWR and AHTR core designs and overall neutronics behaviors demands adaption of the original procedure to accurately capture the physics characteristics of the AHTR. This adaption will result in new two-step procedure specifically tailored for AHTR modeling.

AHTR employs graphite for neutron moderation, which provides lower parasitic moderator neutron absorption and increased neutron upscatter in comparison to light water. The lower parasitic moderator neutron absorption leads to generally longer diffusion lengths, increasing reaction rate sensitivity of any given assembly to the neutronic influences of its surrounding neighbor assemblies. The increased up-scattering combined with higher operating temperature as well as the overall change in material cross-sections and their associated energy regions of significance produces a significantly different flux spectrum from those typically experienced in LWR assemblies [6]. Both the difference in flux spectrum and increased sensitivity to neighbor effects leads to a need for reevaluating the coarse energy group structure and most likely optimizing it to an altogether different structure from that typically utilized in the LWR two-step procedure. Additionally, the double heterogeneity of the coated TRISO particles along with increased diffusion length effects on plate-cell models warrants particular lattice physics modeling considerations not typically experienced with LWR lattice models.

The goal of this research then is to develop a AHTR specific two-step procedure similar to the traditional LWR two-step procedure which accurately predicts the neutronics behavior of the AHTR core while allowing for fast full core simulations. With such a tool available, enhanced fuel and core design optimization may be achieved through an expedited iteration process, and improved fuel cycle and safety margin analyses realized by direct coupling of full core neutronics simulations to thermal hydraulics models.

1.1. Molten Salt Reactor History

Generation II nuclear reactors, which make up most if not all of the currently operating nuclear fleet, have demonstrated with few exceptions the value of nuclear power for generating safe, clean, and efficient power since the late 1960's [7]. However, despite their mostly positive track record, generation II reactors still have a number of characteristics that warrant enhancement. Generation III and generation III+ reactor designs such as the Advanced Boiling Water Reactor (ABWR) and AP1000 will help in addressing some of the short comings predominantly by augmenting safety. Ultimately though, Generation IV reactors will be the designs which will substantially address the major goal areas of sustainability, safety / reliability, economic competitiveness, and proliferation resistance / protection [8]. An illustration of the conceptual progression of nuclear power plant designs is summarized in Figure 1-1.

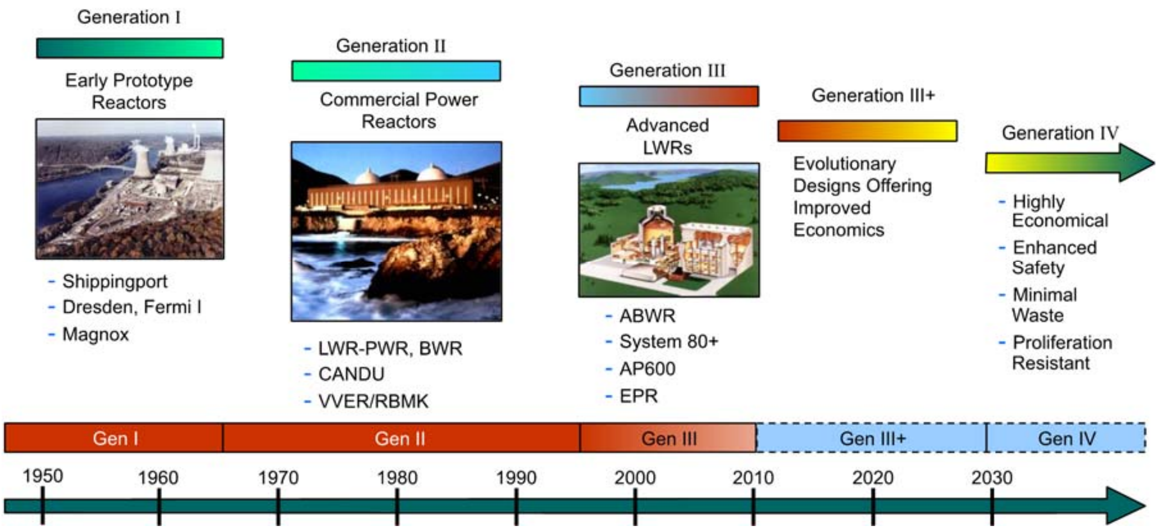

Figure 1-1 Depiction of Progression of Nuclear Plant Design [8]

A variety of Generation IV reactor designs have been postulated and analyzed over the years, including the Very High Temperature gas cooled Reactor, Molten-Salt Reactor, Super Critical Water Reactor, Gas cooled Fast Reactor, Lead cooled Fast Reactor, and Sodium cooled Fast Reactor [9]. A depiction of these designs can be found in Figure 1-2. The focus of the research presented in this report is the Molten Salt Reactor (MSR), which uses molten salt as a coolant with either the fuel being present in some solid fuel form such as lattices, pebbles, or blocks, or as a homogenous mixture with the coolant salt. Possibly the earliest consideration for this design for power production was the Aircraft Nuclear Propulsion project at the Oak Ridge National Laboratory (ORNL) that began in the fall of 1949 [10]. The design used in this project consisted of a $NaF\text{-}ZrF_4\text{-}UF_4$ fuel salt mixture circulated through a beryllium oxide reflecting and moderating region. The fuel would undergo fission as it passed through the beryllium oxide region and generate high temperature power for purposes of aircraft propulsion. An illustration of the reactor concept can be found in Figure 1-3. The Aircraft Reactor Experiment (ARE) operated from October 30 1954 until November 12 1954 and achieved high temperature power production at 2.5 MWt and fuel temperatures at 1133 K with stable reactor behavior and no significant operating issues.

Examination of the molten salt reactor design continued in the 1960's with the Molten-Salt Reactor Experiment (MSRE) [11]. This reactor consisted of a uranium, lithium-7, beryllium, and zirconium fluoride salt mixture that circulated through a graphite moderated reactor, and operated from 1965 to 1969. An illustration of this reactor design is shown in Figure 1-4. During this timeframe, the experiment achieved its goal of demonstrating the safe, reliable, maintainable, and practical operation of a molten salt reactor for high temperature power production and potential future fuel breeding applications. The MSRE was capable of producing 8 MWt at an average salt temperature of 922 K and experienced only minor operating issues during its operating period [12].

Unfortunately, political support for the MSR flagged in favor of the competing Liquid Metal Faster Breeder Reactor resulting in a halt of major ORNL experimental research progress in 1974 [13]. Conceptual analyses continued at ORNL throughout the late 1970's and early 1980's with research even switching from the original breeder reactor design to a converter reactor concept after support for breeding and reprocessing faltered due to nuclear proliferation fears [13-15]. Other countries also analyzed various molten salt reactor designs from the 1980's up through the 2000's [16]. However, not until 2003 did a renewed interest in the molten salt reactor reemerge at ORNL in the form of a molten-salt-cooled Advanced High Temperature Reactor (AHTR) [17].

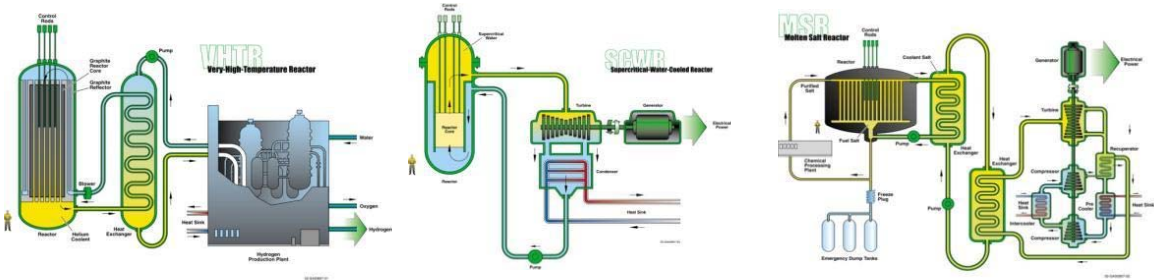

Very High Temperature Reactor *Super Critical Water Reactor* *Molten Salt Reactor*

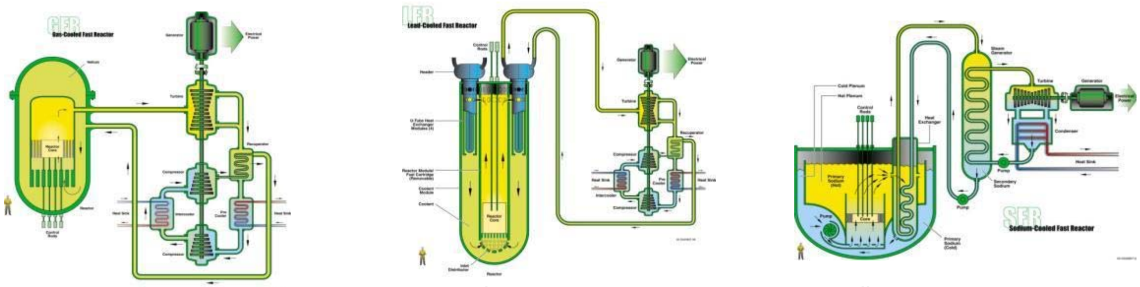

Gas Fast Reactor *Lead Fast Reactor* *Sodium Fast Reactor*

Figure 1-2 Conceptual Images of Generation IV Reactor Designs [9]

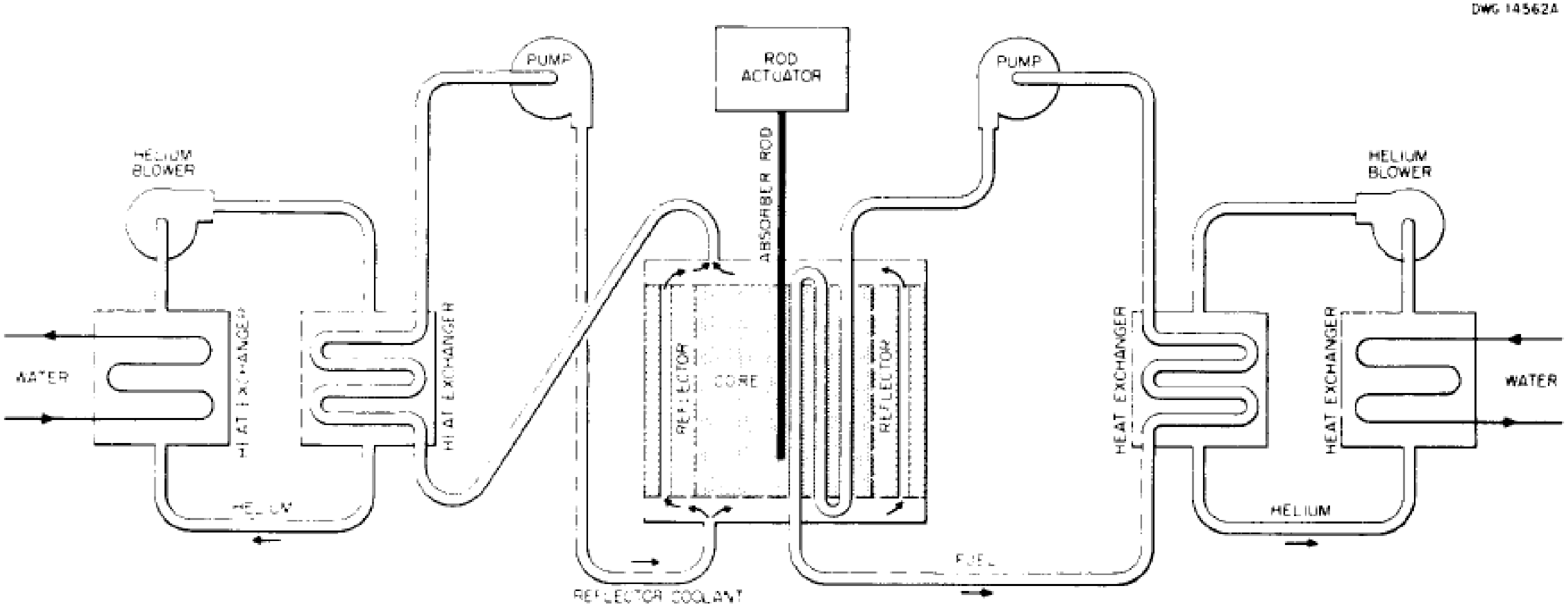

Figure 1-3 Schematic Diagram of ARE Reactor [10]

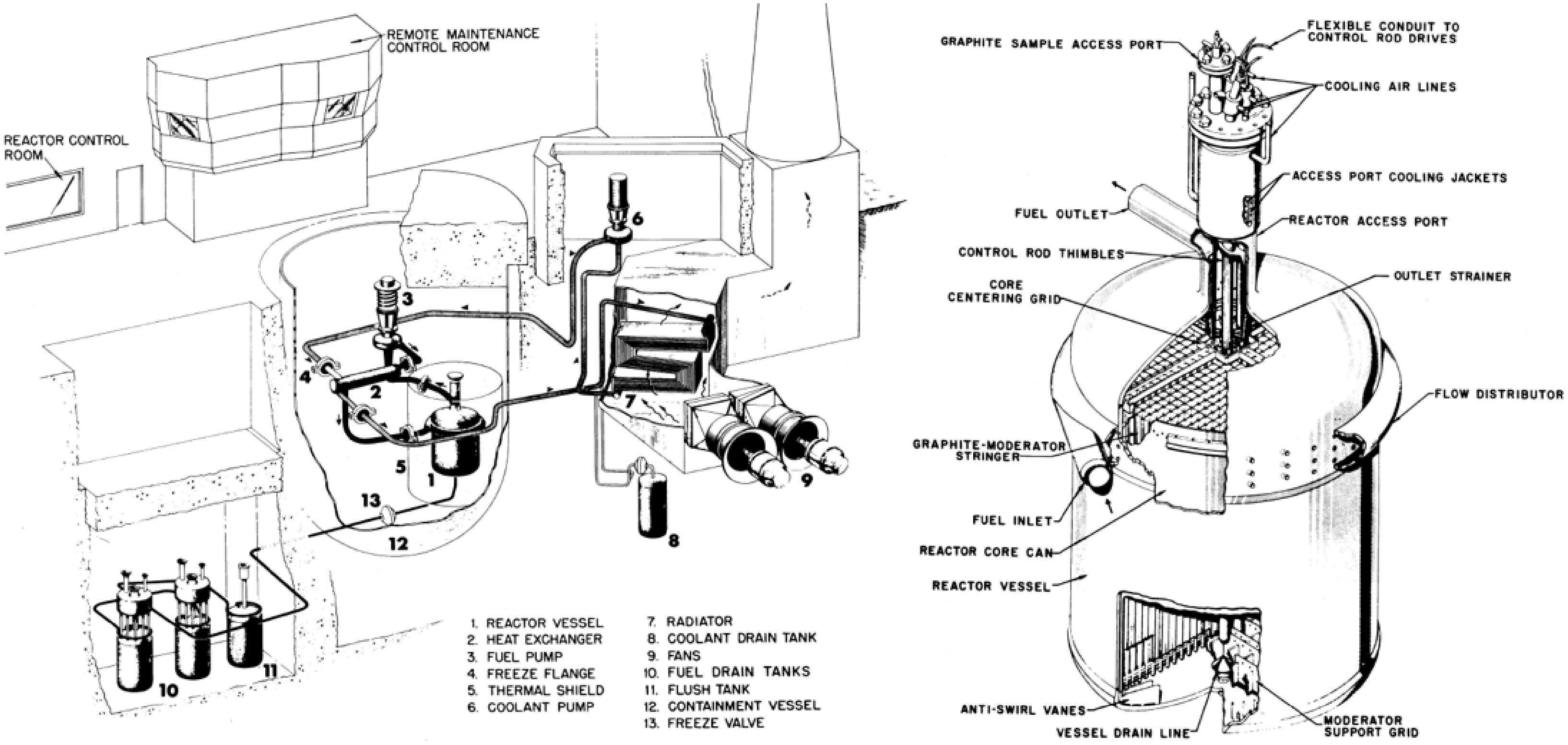

Figure 1-4 Layout of MSRE and Reactor Vessel [12]

1.2. Advanced High Temperature Reactor Concept

The AHTR design was proposed to use a molten salt coolant for its ability to provide very high temperature atmospheric pressure operations along with a solid form fuel of coated particles in a graphite matrix.. The high temperature operability, capable of producing power at 1023 K to 1273 K, would allow for electricity production by means of the high efficiency (>50%) Brayton cycle, as well as thermochemical production of hydrogen. Low operating pressure would help to alleviate the need for thick-walled pressure vessels as well as allow for robust safety through fully passive decay heat rejection systems. The solid fuel form, as opposed to a fuel and salt mixture, would help minimize coolant radioactivity which is greatly beneficial from an operational, maintenance, and safety standpoint. Additionally, the solid fuel form would help minimize the corrosion risk of fission products to the reactor coolant system by inhibiting fission product release to the coolant [17].

When considering the DOE Generation IV design goals of sustainability, safety / reliability, economic competitiveness, and proliferation resistance, the AHTR is expected to perform well. Preliminary economic estimations show the AHTR should have a levelized cost of electicity that is very similar to existing LWRs, with the savings from higher thermal efficiency and availability being offset by the increased fuel cycle costs [18]. AHTRs should match or exceed the safety performance and proliferation resistance of gas cooled reactors due to the fact that AHTRs will also use the coated particle fuel in graphite matrix strategy as do the gas cooled reactors, and subsequently out perform all LWRs [19].

Since its inception, a variety of fuel and core designs have been considered for the AHTR. These considerations have ranged from using pebbles, solid cylinder compacts, annular compacts, and planks, as well as reactors of various sizes and power outputs, and a plethora of salts for coolant [1,20-23]. Though these choices provide a number of possible design combinations, the focus of this research will follow the design concept presented in ORNL/TM-2011/365 and ORNL/TM-2012/320 [1,2]. This layout consists of a large $LiF\text{-}BeF_2$ (“FLiBe”) salt cooled graphite moderated reactor capable of producing 3,400 MW of thermal power with either 253 or 252 assemblies surrounded by a graphite reflector. An illustration of this reactor design can be found in Figure 1-5. FLiBe, though having expensive material and lithium enrichment costs, was chosen for the primary coolant due to its better heat transfer and nuclear performance as well as lower activity post neutron bombardment [20].

The fuel assemblies use a plank or plate based design, shown in Figure 1-6, similar to the design originally proposed in the conceptual design studies of the large Molten Salt Breeder Reactor [14]. Fuel-bearing TRistructural ISOtropic (TRISO) particles are dispersed within two fuel stripe regions located towards the edges of the plate to ensure sufficient heat conduction from the plate to the coolant. These plates are then placed in an assembly with spaces between each plate to provide low-resistance channels for coolant flow. This design allows for greater design flexibility for fuel-to-carbon-to-coolant ratio as well as enhanced passive cooling capabilities when comparing to the pebble bed alternative. It can obtain acceptable levels of fuel burnup under different refueling strategies, but is not expected to achieve as high a level of burnup as a pebble based design [24].

The fuel-bearing TRISO particles, depicted in Figure 1-7, are small multilayered particles used to contain fuel and fission products [25]. TRISO particle kernels are fabricated using a gel formation process and are then coated with the various layers by means of chemical vapor deposition [26,27]. TRISO particles were originally developed for use in modular helium reactors due to their ability to retain fission products in a high temperature environment, and as such have made a natural transition to high temperature molten-salt cooled applications. In addition to fission product retention during fuel operations, TRISO particles encapsulated in a graphite matrix provide superior retention during repository storage as well as enhanced proliferation resistance when compared to current LWR fuel designs [25].

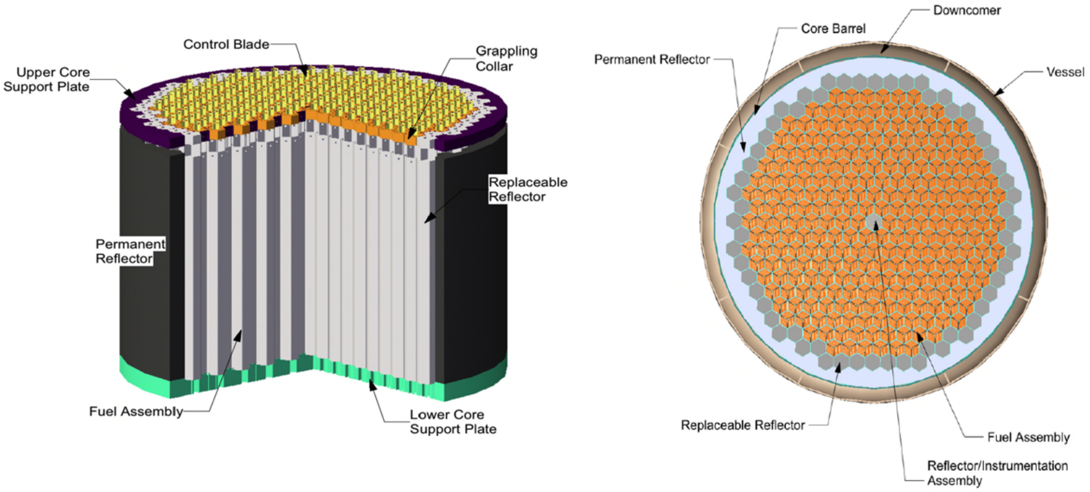

Figure 1-5 AHTR Core Design [1]

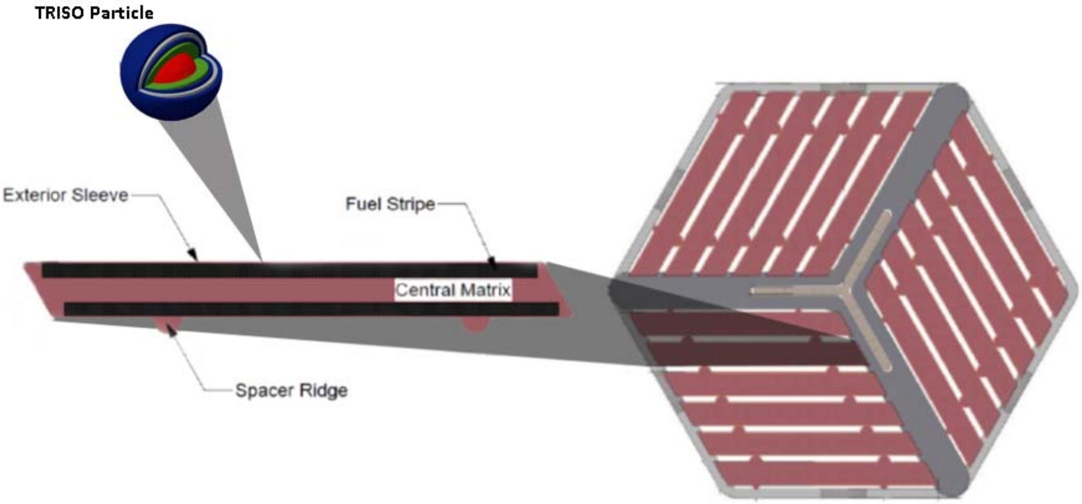

Figure 1-6 AHTR Fuel Assembly Element [1]

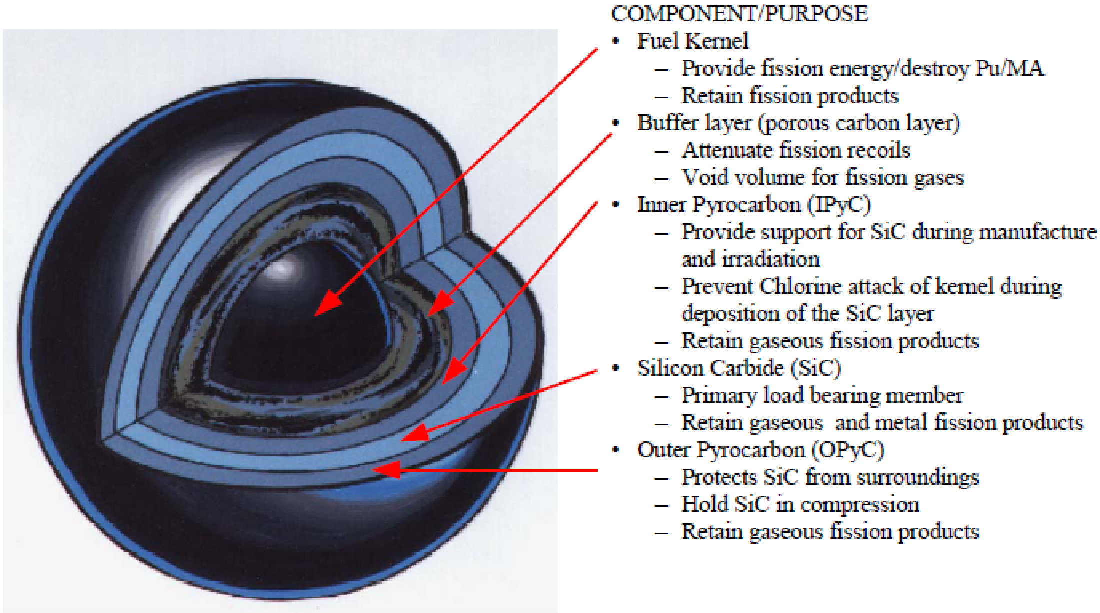

Figure 1-7 Functional Schematic of TRISO Particle [25]

1.3. Previous Analysis and Modeling Techniques

The most current research in the plate based AHTR design comes from the previously mentioned ORNL studies summarized in documents ORNL/TM-2011/365 and ORNL/TM-2012/320 [1,2]. In these studies, neutronic models were simulated for a plate type assembly design based upon thermal-hydraulic and mechanical considerations. This base design was analyzed using two different fuel enrichments (19.75% and 9%), a variety of fuel region thicknesses to adjust the Carbon to Heavy Metal (CHM) ratio, using Europium burnable poison spheres for reactivity hold down, and a variety of core refueling batching schemes. Neutronic performance metrics consisted of reactivity feedback coefficients, power distributions, isotopic burnups, and cycle length assessments. Cycle length approximations were obtained by means of simple Linear and Non-Linear Reactivity models and Equilibrium Core evaluations.

Two major multigroup model types served as the drivers for depletion analysis in this study. One model utilized a Reactivity Physical Transform (RPT) approach in which a combination of both particle homogenization and geometry transformation are applied such that reactivity equivalence with the true model is maintained but the detailed treatment of the TRISO particle is avoided [28]. The RPT approaches considered by the ORNL study are illustrated in Figure 1-8. The second model type maintained explicit treatment of TRISO particles in a regular arrangement, but applied a Dancoff reactivity equivalency factor for the multigroup treatment. For both model types, entire assemblies were represented with a single depletion region, and for full core analysis a single depletion region was often times used to represent multiple assemblies.

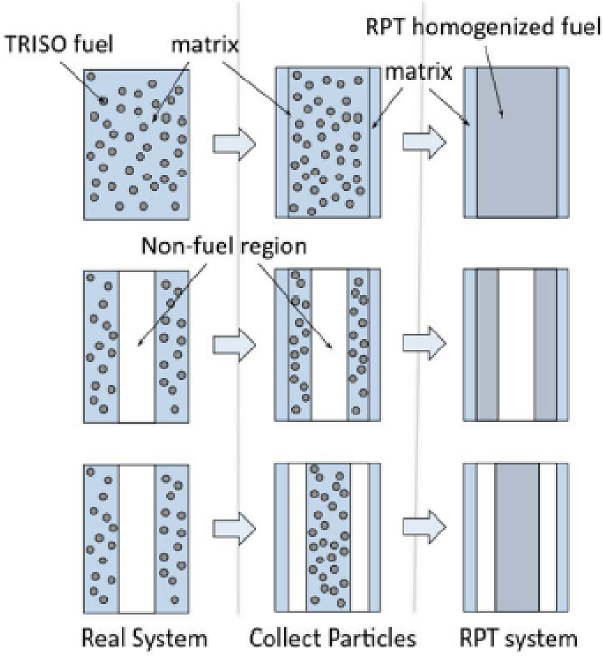

Figure 1-8 Reactivity Physical Transform Strategies Considered in ORNL Study [1]

Though these initial studies are believed to provide meaningful results, and have since been further supplemented by additional analysis by Lewis et. al. [29], it can easily be seen that much analysis still remains both with regards to design optimization and model fidelity improvement. The most problematic issues with the modeling approaches used in the ORNL studies are the simulation runtimes as well as model fidelity. With regards to model fidelity, an RPT treatment loses the ability to reliably predict plate power distributions and is easily defeated by the expected eventual use of burnable poisons within the plates. Additionally, no strong coupling to thermal-hydraulics is present to assess at power steady state and transient safety. With regards to runtimes, simulations of 3-D full core models using the SERPENT 2 Monte Carlo code with explicit TRISO particle treatment, conducted as part of this research, indicate that when even using 19,200 AMD Opteron cores on the ORNL TITAN supercomputer, runtimes can take as long as 1.24 wall clock hours in order to obtain a fairly converged stripe-wise power distribution. The ORNL studies reported a factor of 20 speedup when applying the RPT approximation, however on the aforementioned full core model this would still require minutes of runtime on a comparably large number of processors [1], thus also implying a need for access to world-class supercomputers to perform analyses. It can easily be seen then that simulating multiple state-points (i.e. burnups and / or perturbation cases) along with any sort of strong thermal-hydraulic coupling will take hours if not days to complete. Combined with the desire of seeking equilibrium cycle conditions and iterating over many assembly designs, the problem of design optimization quickly becomes untenable. Therefore it becomes desirable to seek an alternative means of simulation that allows both an improved degree of model accuracy as well as reduced simulation runtime. The classical two-step procedure utilized in LWR modeling is believed to provide such a means of simulation.

1.4. two-step Procedure

Reactor simulations are predominantly conducted in one of two ways; either by use of stochastic Monte Carlo or deterministic methods. Monte Carlo approaches simulate the migration and nuclear interactions of individual neutrons as they traverse the core using random number generators and probability distribution functions dictated by core geometry and composition. Deterministic approaches utilize partial differential equations to describe neutron behavior that are discretized and the resulting algebraic system solved. Monte Carlo methods can faithfully represent geometric and neutron interaction details, but due to their statistical nature require a large number of neutron tracking simulations, and subsequently long computer runtimes to provide results with an acceptably low statistical uncertainty. Deterministic methods, on the other hand, provide an approximate answer due to their reduced degree of neutron energy and angular / spatial discretization, but can be made faster than Monte Carlo techniques through acceptable approximations to the transport equation. As such, deterministic approaches have taken precedence in the realm of reactor design and coupled neutronic and thermal hydraulic simulations [30].

Deterministic methods are founded on solving for the angular flux $\psi(\vec{r}, E, \hat{\Omega})$ in the steady state Boltzmann transport equation for neutrons which is presented below in Equation (1-1):

$$\begin{gathered} \hat{\Omega} \cdot \nabla\psi(\vec{r}, E, \hat{\Omega}) + \Sigma_t(\vec{r}, E)\psi(\vec{r}, E, \hat{\Omega}) = \\ \int_{4\pi} d\hat{\Omega}' \int_0^\infty dE'\Sigma_s(\vec{r}, E' \to E, \hat{\Omega}' \to \hat{\Omega})\psi(\vec{r}, E', \hat{\Omega}') + \\ \frac{\chi(E)}{4\pi k} \int_0^\infty dE'\nu(E')\Sigma_f(\vec{r}, E') \int_{4\pi} d\hat{\Omega}'\psi(\vec{r}, E', \hat{\Omega}')\ , \end{gathered} \tag{1-1}$$

where,

$\hat{\Omega} =$ Directional Unit Vector,

$\Sigma_t(\vec{r}, E) =$ Total Interaction Cross Section,

$\Sigma_s(\vec{r}, E' \to E, \hat{\Omega}' \to \hat{\Omega}) =$ Scattering Cross Section,

$\Sigma_f(\vec{r}, E') =$ Fission Cross Section,

$\chi(E) =$ Fission Neutron Spectrum,

$\nu(E') =$ Avgerage Number of Neutrons per Fission,

$k =$ Multiplication Factor.

The neutron reaction cross sections, fission neutron spectrum, and average number of neutrons per fission have been measured for a variety of isotopes and discrete energies and are tabulated in datasets known as cross section libraries. The underlying nature of the Boltzmann transport equation as well as the complex structure of the cross section data sets leads the equation to having an analytical solution only in very rare and special cases (e.g: one-speed neutrons and homogenous infinite geometries), and so numerical techniques and phase space discretization must be applied to solve for neutron flux in finite heterogeneous reactors. However, it is impractical both from a computational resource and time standpoint to attempt to solve for a full core flux distribution directly using a sufficiently refined spatial mesh that the required mesh sizes would introduce an extraordinary number of simultaneous algebraic equations to solve. This is especially true when considering the detailed nature of many cross sections, Figure 1-9 providing an example, in which hundreds of thousands of energy divisions would be required to capture every facet.

Fortunately, most power reactors exhibit a high degree of geometric regularity, being mainly Cartesian or hexagonal arrays of fuel pins and fuel assemblies, which allows for simplifying assumptions and ultimately a reduction in geometric mesh requirements. This increase of mesh size at the core level is achieved through proper homogenization of geometric and energy details. Reaction rate distributions are the primary concern in reactor simulations and as such must be preserved in any approximations or simplifications that are made. Therefore, an appropriate form of spatial and energy fidelity reduction is by means of a reaction rate preserving homogenization, which can be achieved through flux weighted averaging such as show in Equation (1-2):

$$\langle\Sigma_g\rangle_{cell} = \frac{\int_{E_g}^{E_{g-1}} dE \int_{V_{cell}} d^3r\Sigma(r,E)\phi(r,E)}{\int_{E_g}^{E_{g-1}} dE \int_{V_{cell}} d^3r\phi(r,E)} \text{ where } \phi(\vec{r},\mathrm{E}) = \int_{4\pi} d\hat{\Omega}\psi(\vec{r},\mathrm{E},\hat{\Omega}) \qquad (1\text{-}2)$$

Such a homogenization entails knowing the desired answer $\psi(\vec{r},\mathrm{E},\hat{\Omega})$ prior to the simplification, and would at first seem to defeat the purpose of the fidelity reduction. However, because of the regularity of the reactor geometry and its large size, one can assume that repeating elements, such as fuel pins or fuel assemblies, may be accurately represented as lying within an infinite repeating array, and thus reduce the homogenization problem requirement of simulating a priori the neutron flux distribution of the entire core to only the neutron flux of a single pin or assembly with reflective or periodic boundary conditions.

In LWRs this approach is used to quickly solve the transport equation for the flux distribution on the pin cell level, which then is simplified with respect to energy using the afore mentioned reaction rate preserving homogenization to reduce the energy resolution from the original high resolution cross section data of thousands of energy points to a lower resolution but still accurate multi-group energy structure of only a few hundred energy group averages. Using these simplified cross section sets, the transport equation is then solved for typically a single fuel assembly and the resulting angular flux distribution used to reduce the geometric complexity of the lattice to a single homogenized node and the energy group structure from a multi-group structure down to a few group structure of only tens or fewer averaged cross section values.

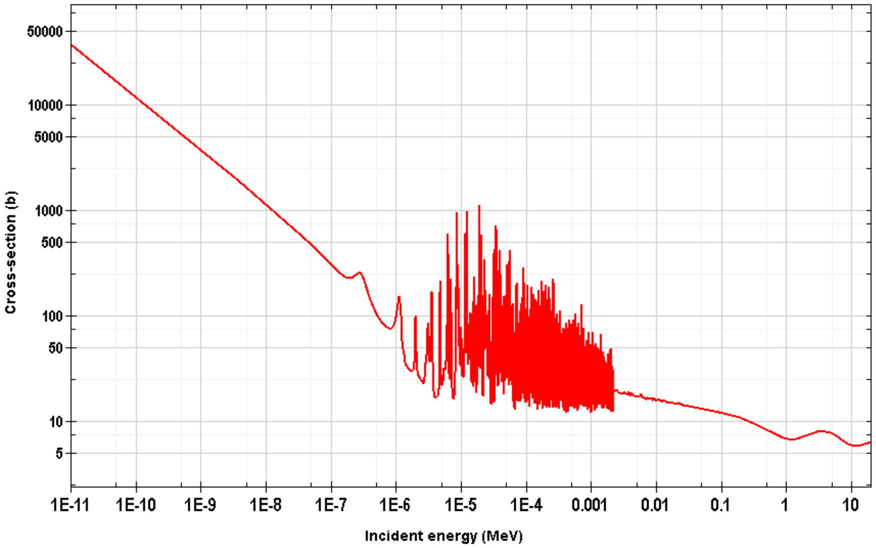

Figure 1-9 Total ^{235}U Neutron Cross Section [31]

This approach could be carried further into solving the transport equation over the entire core using the approximations from the lattice level simulations of every assembly design used in the core, but would still be computationally expensive in regards to the number of spatial and angular subdivisions necessary for an accurate solution. Since the primary concern of reactor simulations is to obtain reaction rate distributions, it is truly only necessary to solve for the scalar flux $\phi(\vec{r}, E)$ rather than the angular flux $\psi(\vec{r}, E, \hat{\Omega})$. As such, a further simplification at this point is to solve for the scalar flux distribution using a diffusion approximation shown in Equation (1-3) rather than solving the transport equation for the angular flux

$$-\nabla \cdot D_g(\vec{r})\nabla\phi_g(\vec{r}) + \Sigma_{Rg}(\vec{r})\phi_g(\vec{r}) = \Sigma_{g'=1}^{g-1}\Sigma_{sg'g}(\vec{r})\phi_{g'}(\vec{r}) + \frac{1}{k}\chi_g\Sigma_{g'=1}^{G}\nu_{g'}\Sigma_{fg'}(\vec{r})\phi_{g'}(\vec{r}) \tag{1-3}$$

where, for a given energy group g

$D_g(\vec{r})$ = Diffusion Coefficient,

$\Sigma_{Rg}(\vec{r})$ = Removal Cross Section,

$\Sigma_{sg'g}(\vec{r})$ = g’ to g Scattering Cross Section,

$\Sigma_{fg'}(\vec{r})$ = Fission Cross Section,

χ_g = Fission Neutron Spectrum,

$\nu_{g'}$ = Average Number of Neutrons per Fission,

k = Multiplication Factor.

Energy group averages of cross sections, fission neutron spectrum, and average number of neutrons per fission may all be approximated from reaction rate preserving averaging with the angular flux solution of the lattice simulations. The diffusion coefficient is typically calculated using Equation (1-4), though it should be noted that alternative methods for calculating this value exist, some of which even allow for multiple directionally dependent diffusion coefficient.

$$D_g(\vec{r}) = \left[3\Sigma_{trg}(\vec{r})\right]^{-1} = \left[3\left(\Sigma_{tg}(\vec{r}) - \bar{\mu}_0\Sigma_{sg}(\vec{r})\right)\right]^{-1} \tag{1-4}$$

where, for a given energy group g

$\Sigma_{trg}(\vec{r})$ = Transport Cross Section,

$\Sigma_{tg}(\vec{r})$ = Total Cross Section,

$\bar{\mu}_0$ =average cosine of scattering angle $\approx 0.07\ A^{2/3}E$,where E is energy in MeV and A is mass number,

$\Sigma_{sg}(\vec{r})$ = Total Scattering Cross Section.

This use of the diffusion approximation removes the need for treating the angular dependency of the neutron flux during full core simulations, but still can suffer from requiring a fine spatial discretization for an accurate solution when employing methods such as standard finite difference. To relax this requirement and allow for larger mesh sizes, a number of various nodal techniques have been developed and employed. However, for this research the Nodal Expansion Method (NEM) combined with Simplified Equivalence Theory will be the primary focus [3-5]. This method, rather than solving the mesh cell or node scalar flux as a flat average value across the node constructs polynomial relationships to describe the flux shape within a node while preserving face-averaged currents and cell averaged fluxes. The polynomial coefficients are determined for each node through the use of the cross-section and diffusion data along with the use of the inter-nodal continuity of current condition, the nodal diffusion equation along with multiple moment-weighted variants of the nodal diffusion equation, and an inter-nodal discontinuity of flux condition with associated surface discontinuity factors defined in Equation (1-5). The heterogeneous and homogenous boundary fluxes can be and are calculated during the lattice transport simulation and subsequently are used to define the discontinuity factors of all node surfaces in the full core diffusion simulation.

$$\phi_{\mathrm{homog}_{\mathrm{node}_1}} f^{+}_{\mathrm{node}_1} = \phi_{\mathrm{homog}_{\mathrm{node}_2}} f^{-}_{\mathrm{node}_2}, \quad f = \frac{\phi_{\mathrm{heter}}}{\phi_{\mathrm{homog}}} \tag{1-5}$$

where,

$\phi_{\mathrm{heter}} =$ Surface flux at Lattice Boundary as calculated using the heterogeneous lattice model,

$\phi_{\mathrm{homog}} =$ Surface flux at Lattice Boundary as calculated using the homogenized lattice model.

It should be noted that nodal approaches have been formulated for hexagonal nodes specifically, however for this research conformal mapping of the hexagonal node to a rectangular node served as the basis for the later discussed primary core simulator. This mapping approach provides a means of avoiding nonphysical singular terms often encountered in conventional nodal formulations for hexagonal nodes as well as allow for reuse of Cartesian based nodal codes [32]. By using NEM, the mesh cells can be sufficiently coarsened such that simulation runtimes are more tractable. Though it would seem that the details concerning the resolution of individual pin power are lost in the lattice geometry homogenization and subsequent mesh coarsening of the NEM method, techniques have been developed to reconstruct the pin powers post full core simulation by using values known as Form Factors [33]. These Form Factors are calculated during the lattice transport simulation by computing the relative pin powers of every pin within a lattice as shows in Equation (1-6). The Form Factors are then used in conjunction with the intra-nodal power shape solved for during the full core diffusion simulation to reconstruct the pin powers as shown in Equation (1-7).

$$\mathrm{FF}(\mathrm{r},\theta)=\frac{\mathrm{p}^{\mathrm{Lattice}}(\mathrm{r},\theta)}{\langle\mathrm{p}\rangle^{\mathrm{Lattice}}} \tag{1-6}$$

where,

$\mathrm{p}^{\mathrm{Lattice}}(\mathrm{r},\theta)$ = Lattice power at radial location "r" and azimuthal location "θ",

$\langle\mathrm{p}\rangle^{\mathrm{Lattice}}$ = Overall lattice average power.

$$\mathrm{p}(\mathrm{r},\theta)=\mathrm{p}^{\mathrm{Intra}}(\mathrm{r},\theta)\times\mathrm{FF}(\mathrm{r},\theta) \tag{1-7}$$

where,

$\mathrm{p}^{\mathrm{Intra}}(\mathrm{r},\theta)$ = Intra-nodal power at radial location "r" and azimuthal location "θ",

$FF(\mathrm{r},\theta)$ = Form Factor at radial location "r" and azimuthal location "θ".

This process of using higher fidelity transport calculations at the pin and lattice level to generate homogenized few-group cross sections, diffusion coefficients, discontinuity factors, and form factors for full core modeling is further extended to capture both the effects of fuel depletion and dynamic changes in operating conditions. Though pin and lattice level transport calculations are performed using the steady state form of the transport equation, the effects of fuel depletion may be simulated by using the resulting angular flux distribution and homogenized cross sections from the lattice simulations to solve a simple 1-D relationship of change in isotopic content with respect to change in time as shown in Equation (1-8). One can define such an equation for all isotopes of interest in a reactor model and by solving the resulting set of simultaneous equations one can describe how the material compositions of the reactor changes during operation, and subsequently can perform lattice transport models for various burnup states. These depletion equations are typically solved using numerical methods such as Predictor-Corrector with finite difference [34].

$$\frac{dN_A}{dt} = -\lambda_A N_A - \left[\sum_g \sigma_{a_g}^A \phi_g\right] N_A + \sum_B \lambda_B N_B + \sum_C \left[\sum_g \sigma_{\gamma_g}^C \phi_g\right] N_C \qquad (1\text{-}8)$$

where, for a given energy group g

N_A = Isotope of Interest Number Density,

λ_A = Isotope of Interest Decay Constant,

$\sigma_{a_g}^A$ = Isotope of Interest microscopic absorption cross section,

N_B = Parent Isotope Number Density,

λ_B = Parent Isotope Decay Constant,

N_C = Transmutable Isotope Number Density,

$\sigma_{\gamma_g}^C$ = Transmutable Isotope microscopic cross section for transmutation to Isotope of interest,

Additionally, lattice level simulations can be performed at every burnup state with an assortment of perturbations, otherwise known as branches, of the other material condition parameters such as coolant temperature and density, fuel temperature, or concentration of coolant soluble poisons to represent the various operating conditions of the reactor. In this way, a library of homogenized cross sections and diffusion simulation parameters can be generated to represent all fuel designs in a given core and the various anticipated operating conditions. These may then be functionalized in the core diffusion simulation as part of the model geometry definition to allow for a form of interpolation between library state points and assembly designs. Ultimately, this allows for both depletion of individual nodes in the core simulation and possible coupling to a thermal hydraulics models to capture neutronic thermal hydraulic feedback effects.

This entire process of using pin and lattice level transport calculations to generate homogenized few group cross section and diffusion parameter libraries for use in a coarse mesh nodal diffusion core simulation represents today's standard analysis approach employed in the commercial nuclear industry and is herein referred to as the "Two-Step" procedure summarized by Figure 1-10. Though some up-front work is required to generate the few group libraries, once created they may be used in a nodal diffusion code to simulate a variety of core designs and operating conditions in mere seconds or minutes on a single computer core as opposed to a more rigorous deterministic transport treatment or Monte Carlo simulations which require thousands of computer cores and hours if not days of runtime. As such, the two-step procedure is very nearly a necessity for core design optimization and thermal hydraulically coupled neutronic safety margin evaluation.

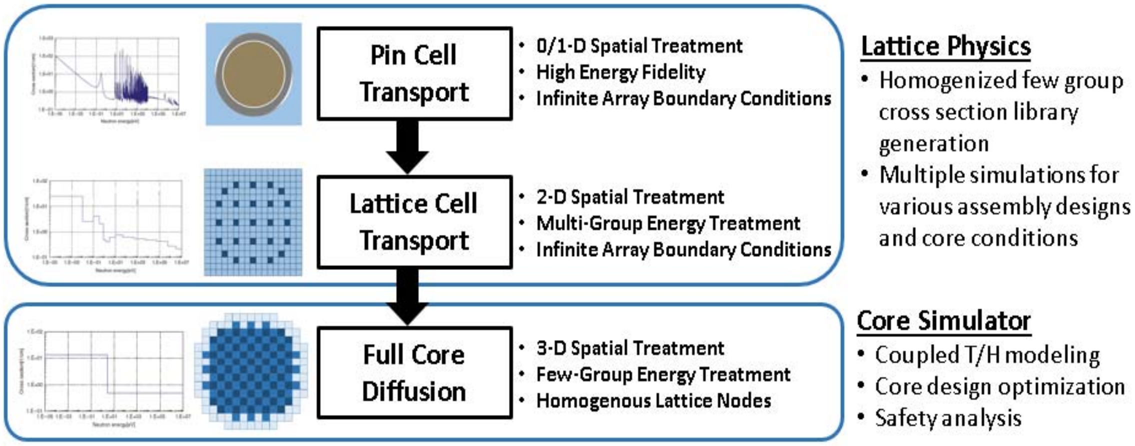

Figure 1-10 Standard LWR two-step Procedure

1.5. Challenges of Developing AHTR two-step Procedure

As evidenced by reviewing the design, it can be readily observed that the AHTR has some significant differences from the typical LWR core, some of which warrant special consideration and require adaption of the traditional LWR two-step procedure.

The first and most obvious of these differences is the use of TRISO particles, which are normally not applied in LWR applications. Growing interest in alternative LWR fuel designs and accident tolerant fuels has led to the development of fairly accurate treatments of TRISO particles in the lattice physics pin-cell calculations, an example of which can be found in the SCALE-NEWT software [34]. However, most production level codes consider TRISOs dispersed strictly in either spheres or cylinders for pebble or pellet applications and not in plates. Though the addition of a plate treatment may seem a small triviality, and in fact should not be difficult to implement, it must be kept in mind that the plates are not all arranged in a nearly 1-D fashion, but rather are rotationally oriented around the assembly center. Combining this fact with the longer neutron diffusion length, contrasted in Table 1-1 versus typical LWR values, it can be seen that deriving an accurate pin-cell model, or in this case plate-cell model, for the initial lattice physics multi-group energy group reduction is considerably more challenging.

The increased diffusion length is essentially a result of using graphite as the primary moderator rather than light water. The carbon in graphite being a larger atom than the hydrogen in water exhibits poorer moderation of neutrons in any individual collision, however graphite as a whole displays a lower parasitic absorption than light water and subsequently an overall superior moderating ratio and subsequently longer diffusion length. Graphite’s solid crystalline structure allows for thermal neutrons to interact with graphite crystals in a coherent scattering manner rather than only individual atom collisions resulting in more complex scattering behaviors and in general greater up-scattering than water. The longer diffusion length not only confounds the accurate simulation of a plate-cell model, but also increases the sensitivity of a given fuel assembly to the influences of its surrounding neighbor assemblies. This leads to a challenging of the infinite assembly assumption employed by the lattice physics calculations, and in order to preserve the accuracy of this assumption one needs to either increase the number of energy groups used in the coarse group structure or consider multi-assembly super cells rather than single assembly cells.

AHTR not only exhibits a longer neutron diffusion length, but the combined effects of graphite’s scattering properties and the AHTR’s higher operating temperature also lead to an altering of the core flux spectrum, as shown in Figure 1-11. We can see in the figure that the thermal spectrum peak is shifted to higher energies as compared to a typical LWR spectrum, which puts it in closer proximity to the low lying plutonium resonances as illustrated for high temperature reactor designs in Figure 1-12. This ultimately means that the energy regions of interest, and subsequently few-group energy boundaries, will be different from those utilized in the LWR two-step procedure.

The need for few-group energy group structure reassessment is further accentuated by the use of an exterior graphite reflector. It can be observed in Figure 1-13 and Figure 1-14 that a large flux gradient exists between the fuel and reflector regions with significant alteration in fuel spectrum which is evident in the outer most assemblies. Therefore, accurately capturing the neutronics of the reflector will require the development of an appropriate reflector model, and a sufficient number of energy groups will be necessary to correctly represent the strong flux gradient between fuel and reflector.

The final challenge, though not entirely unique to the AHTR, is the accurate treatment of control blades throughout the two-step procedure. Given that the FLiBe coolant has a much smaller negative reactivity coefficient than the water in LWRs, as depicted in Figure 1-15, use of a chemical poison shim in the coolant would likely introduce an undesirable positive coolant density reactivity coefficient. Therefore, primary reactivity control must be performed using the control blades. Such a control strategy often does not require the partial insertion of all control elements across the whole core, but rather of only a select few based on fuel burnout and cycle fluctuations. This implies that the infinite assembly assumption for the control blade inserted scenario will be incorrect and in need of adjustment to appropriately account for leakage with the neighboring uncontrolled assemblies.

All of these items must be addressed in order to develop an AHTR adapted two-step procedure. The primary points that can be derived from above is that AHTR requires the development of an appropriate lattice physics model, a re-optimization of the few-group energy group structure, the development of an accurate reflector model, and a leakage adjustment of the control blade insertion lattice results to account for control blade insertion heterogeneity.

Table 1-1 Diffusion Lengths of AHTR compared to LWR

	G	FLUX (1/cm^{2}s)	TOT XS (1/cm)	ABS XS (1/cm)	TRANS XS (1/cm)	D (cm)	MFP (cm)	Diff Length (cm)
	1	1.80E+13	1.96E-01	4.55E-04	1.64E-01	2.03E+00	5.09E+00	66.81
	2	1.20E+14	3.85E-01	2.08E-03	3.59E-01	9.29E-01	2.60E+00	21.16
AHTR	3	4.21E+13	4.01E-01	9.14E-03	3.81E-01	8.75E-01	2.50E+00	9.79
	4	3.02E+12	4.48E-01	2.59E-02	4.43E-01	7.53E-01	2.23E+00	5.40
	1-Group	1.83E+14	3.71E-01	3.92E-03	3.46E-01	9.63E-01	2.69E+00	15.67

	G	FLUX (1/cm^{2}s)	TOT XS (1/cm)	ABS XS (1/cm)	TRANS XS (1/cm)	D (cm)	MFP (cm)	Diff Length (cm)
	1	2.47E+14	5.36E-01	9.94E-03	3.03E-01	1.10E+00	1.87E+00	10.53
LWR	2	3.76E+13	1.36E+00	1.09E-01	9.14E-01	3.65E-01	7.36E-01	1.83
	1-Group	2.84E+14	6.45E-01	2.31E-02	3.84E-01	8.68E-01	1.55E+00	6.13

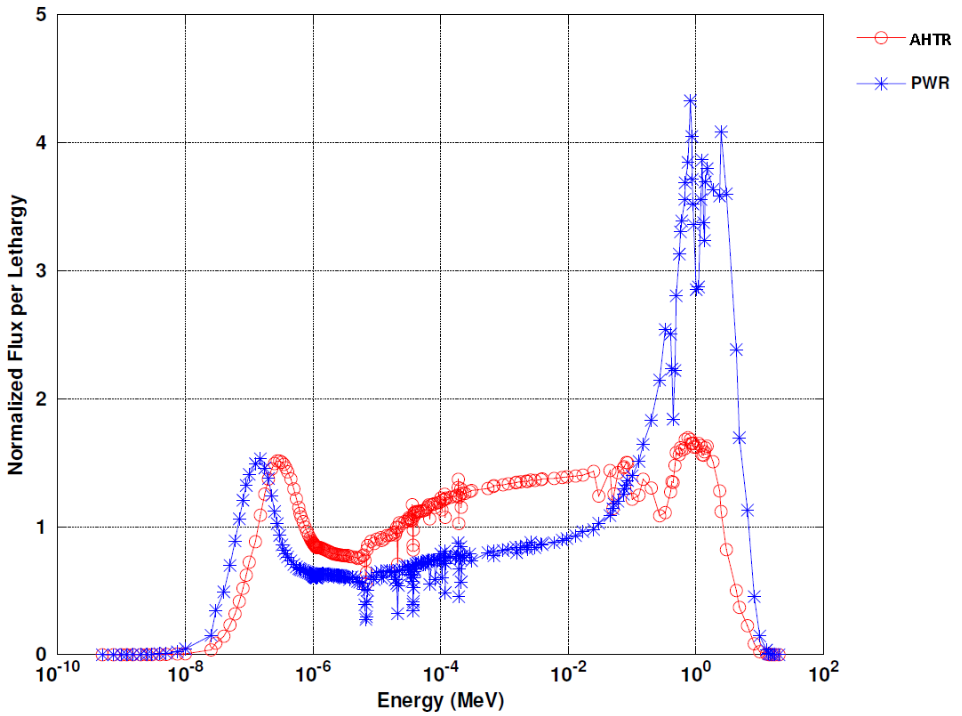

Figure 1-11 Comparison of AHTR and LWR Flux Spectrum

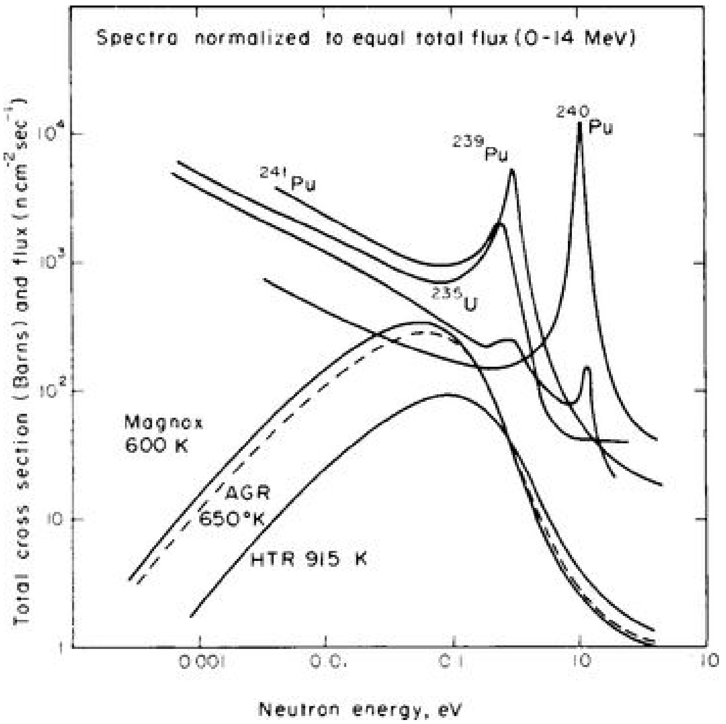

Figure 1-12 Typical Graphite Moderated High Temperature Gas Reactor Flux Spectra and Neutron Cross Sections [6]

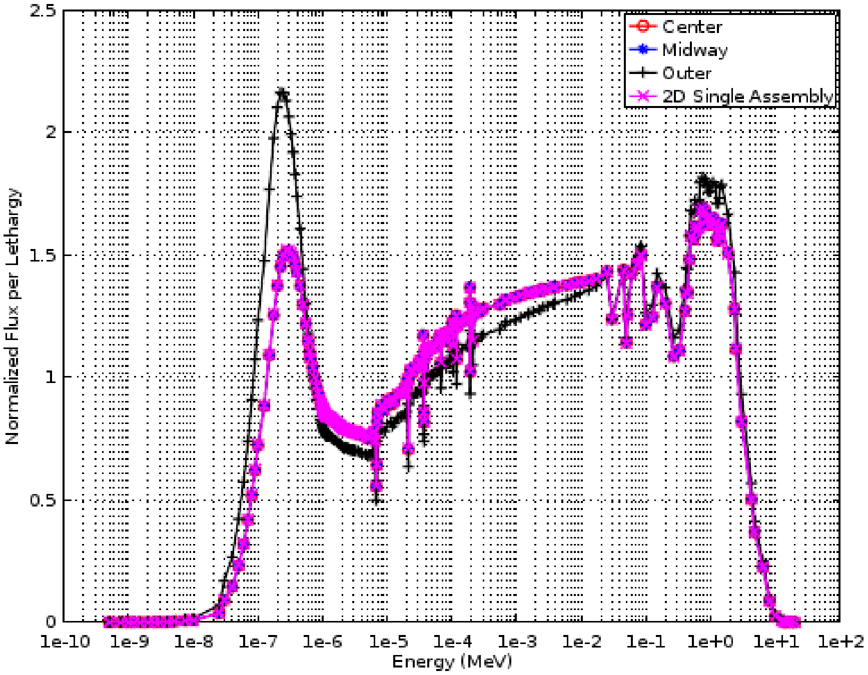

Figure 1-13 Fuel Region Flux Spectrum

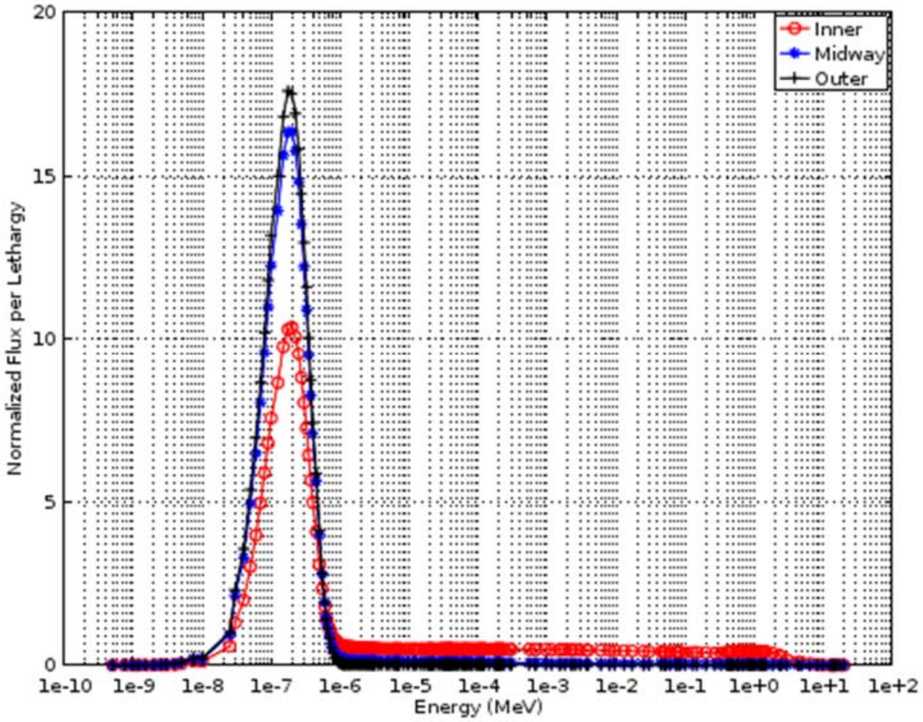

Figure 1-14 Reflector Region Flux Spectrum

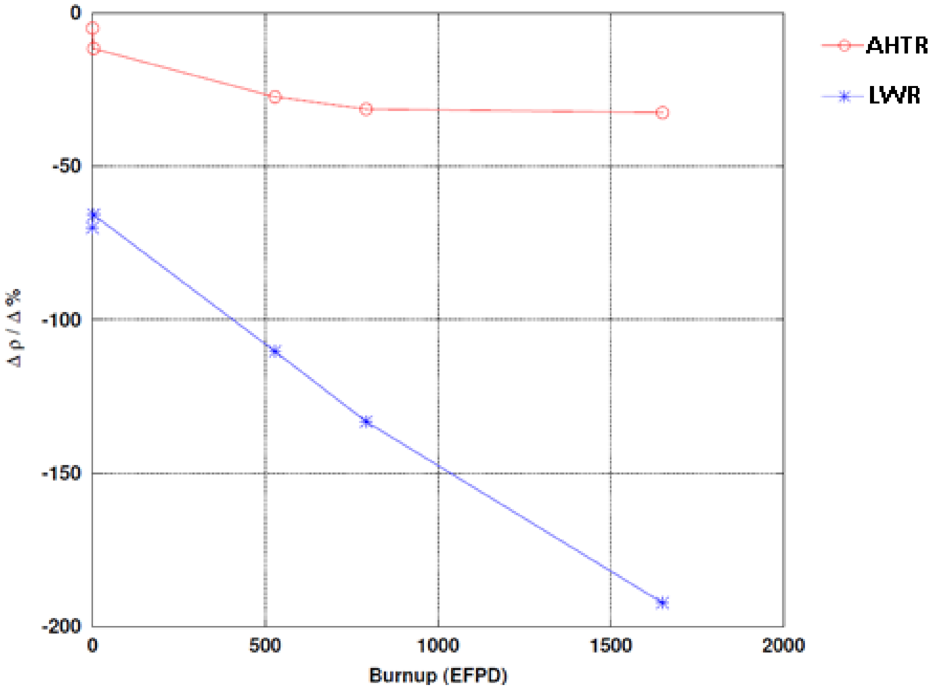

Figure 1-15 Comparison of AHTR and LWR Coolant Density Reduction Coefficient

1.6. Description of Neutronics Codes

Though there is a large number of commercially and freely available codes for lattice physics cross-section generation and full core nodal diffusion simulation, only a few exist that are well suited for developing and executing the AHTR two-step procedure. This section will briefly discuss the challenges facing such codes, the codes that were ultimately chosen, and why they were chosen.

1.6.1. Lattice Physics: SERPENT 2

Most production level lattice physics codes generally employ some deterministic means of solving the neutron transport problem such as Method of Characteristics (MOC) or Collision Probabilities (CP), which are generally very fast methods but, as mentioned previously, require some condensation of the high fidelity energy dependent cross-section data on account of memory constraints. This reduction from high energy fidelity to some coarser multi-group structure is typically achieved by assuming pin-cell regularity and solving an equivalent 1-D pin model, possibly with a 2-D coupling correction, to provide flux distributions for flux weighted averaging of the cross-section data.

However, as stated in the previous section, the longer neutron diffusion length combined with the rotational arrangement of fuel plates within the assemblies makes it difficult to derive an accurate plate-cell model from which to obtain a flux solution for flux weighted cross-section condensation. Two forms of reactivity equivalent adjustments, one involving a physical transformation and the other a Dancoff correction factor, were investigated and employed in the previous ORNL studies [1]. Both of these methods require a reference solution, generally furnished by high fidelity Monte Carlo models, from which to adjust parameters to obtain reactivity equivalency. Both these approaches, though feasible as means of employing the faster deterministic lattice physics methods, introduce some additional error in that they typically assume the reactivity equivalent parameter will hold for the entirety of the fuel depletion. Also, both methods are questionable with regards to power distribution accuracy given that they only ensure reactivity equivalence, and additionally are greatly challenged by models in which burnable poison material is present in the homogenization region.

Recent advances in Monte Carlo simulation techniques, problem parallelization, computer resource utilization strategies, and computer memory capacities have made the use of continuous energy Monte Carlo codes for lattice physics calculations and subsequent generation of homogenized cross-section and diffusion parameters an increasingly viable option. Use of continuous energy Monte Carlo models with sufficient neutron histories essentially eliminate errors associated with geometry and energy fidelity reductions rendering them more accurate relative to the reactivity equivalence approaches. One such candidate code which was specifically designed for lattice physics application is the Monte Carlo code SERPENT 2 [35].

SERPENT 2, and its predecessors SERPENT 1 and PSG, were originally designed with a slightly more narrow scope than typical Monte Carlo codes in that they focused less on shielding applications and more so on homogenization and other assembly-level reactor physics calculations, thus makeing it possible to optimize the calculation routines and obtain significant performance improvement as compared to general-purpose Monte Carlo codes [36]. SERPENT 2 exhibits a number of advantageous features that makes it well suited for this research as listed below:

1. Ability to generate few-group B1 critical spectrum corrected homogenized cross-sections and diffusion parameters including discontinuity factors for fuel and reflectors.
2. Option for explicit treatment of randomly dispersed fuel particles
3. Ability to model graphite as a bounded atom system using thermal scattering libraries
4. Flexible application of Cross-section Unionized Energy speed-up technique based on user memory demands and availability
5. Use of Woodcock delta-tracking for reduced computational overhead
6. Use of Chebyshev Rational Approximation Method (CRAM) for burnup depletion modeling
7. Equilibrium Xenon distribution feature to help with treatment of Monte Carlo Xenon Oscillation

Though SERPENT 2 is still a developmental code, it has shown substantial progress towards achieving its goal of performing accurate lattice physics calculations for 3-D core simulators and is believed to provide a sufficient means of producing few-group cross-section libraries [37-49]. Due to its high degree of accuracy, its favorable runtime, and level of development, SERPENT 2 was selected as the lattice physics code for cross-section generation.

1.6.2. Core Simulator: NESTLE

Though a number of nodal diffusion core simulators could have been used for this analysis, it was believed best for this case to use a code that was sufficiently accurate and capable of handling the geometric and material simulation needs of this research, but most importantly, also actively and locally maintained so as to ascertain support in the event that shortcomings or development needs were discovered. The most modern version of the NESTLE core simulator was found to satisfy the majority of the essential requirements of this research while also providing the benefit of being an in-house code at the University of Tennessee, Knoxville (UTK) which allowed for quick interaction with developers [50].

It should be noted that new features of the modern version of NESTLE maintained at UTK relative to its original release [50], include a full conversion to Fortran 90, simplified input format, two-phase flow thermal hydraulics modeling, advanced depletion and isotope tracking using ORIGEN, output files compatible with VISIT visualization software, and compatibility with SCALE, SERPENT, and CASMO lattice physics. In fact, the new features have expanded NESTLE's versatility from large pressurized water reactors to new core models including boiling water reactors, small modular reactors, and in large part due to this research project, to fluoride salt cooled high temperature reactors.

NESTLE is a NEM based diffusion simulator coupled with either the Homogenous Equilibrium Mixture (HEM) or Drift Flux (DF) thermal hydraulic model for coupled neutronics and thermal hydraulic calculations. NESTLE provides a flexible means of modeling coolant and fuel thermal hydraulic terms by employing user provided polynomials to describe coolant and fuel specific equations of state, making it possible to provide an accurate representation of the temperature dependent density of FLiBe and the heat transfer characteristics between the FLiBe coolant and fuel plates in NESTLE. It also provides the ability to model hexagonal assemblies and few-group parameter functionalization with respect to changes in local node conditions. For these reasons, the NESTLE code was selected as the core simulator for this research.

1.7. Research Goals

The ultimate aim of this research was to develop and demonstrate the feasibility of an AHTR adapted two-step procedure. The proposed procedure is illustrated in Figure 1-16 with SERPENT 2 serving as the lattice physics code and NESTLE as the primary core simulator. Because these two codes have not been used in conjunction prior to this research, linkage codes were developed to parse the results from SERPENT 2 and place them in a format usable by NESTLE. Cross-section and leakage correction generation models were developed for both the reflector and control blade treatment, and few-group energy group structure optimized to ensure accurate simulation in the core simulator. Ultimately, the final results were also benchmarked to ensure accuracy by means of comparison to high fidelity SERPENT 2 full core models.

Successful development of the two-step procedure for AHTRs principally allows for much faster detailed fuel assembly and full core design approaches than what is currently available for AHTRs [51]. This translates into a more expedient design optimization iteration process due to the acceleration of the full core simulations, and allows for better convergence onto optimal fuel and core designs. Additionally, the linkage to a 3-D core diffusion simulator affords the possibility of a strong coupling of neutronics and thermal hydraulics currently absent in AHTR simulations. Such a direct coupling provides a more accurate means of assessing safety related parameters both for at power steady state operation and slow transient scenarios.

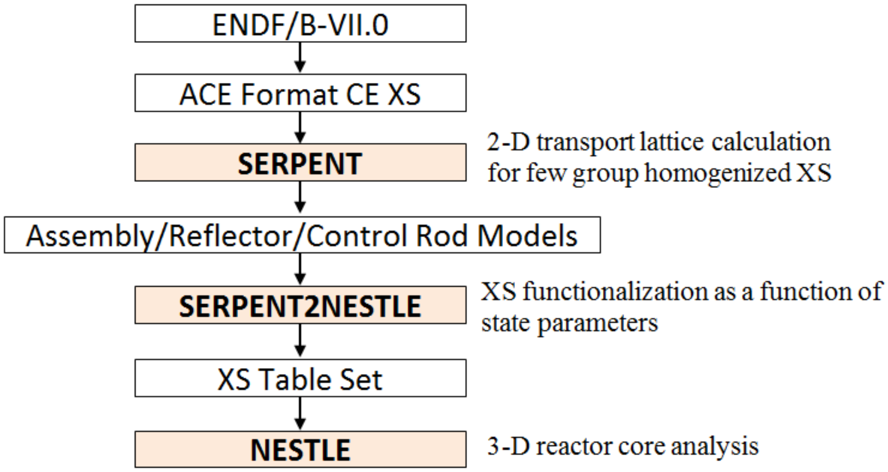

2-D transport lattice calculation for few group homogenized XS

XS functionalization as a function of state parameters

3-D reactor core analysis

Figure 1-16 Illustration of Proposed AHTR two-step Procedure

2. Development of AHTR two-step Procedure

Summarized in this chapter is a discussion of the considerations and steps taken for adapting the two-step approach to the AHTR core design. The chapter covers each of the major points of enquiry applicable to the two-step adaptation for both 2-D lattice physics and 3-D core diffusion simulation.

2.1. Design Specification of AHTR Core

The AHTR core design has yet to be finalized and will likely undergo multiple iterations before a final concept is settled upon. To develop at least some base conception of this procedure one design must be selected, and in this case the design used in the afore mentioned ORNL studies served this purpose.

Though an overall description of the core and fuel concept have been provided previously, a more detailed description of the AHTR design specifications on which this research was conducted is presented in Table 2-1, Table 2-2, Table 2-3. These specifications are based off the design information from the afore mentioned ORNL documents ORNL/TM-2011/365 and ORNL/TM-2012/320 [1,2].

Table 2-1 TRISO Particle Description

Region	Parameter	Parameter Value (μm)	Material	Density (g/cm^3)
Kernel	diameter	427	Uranium Oxycarbide	10.90
Buffer	thickness	100	Porous Graphite	1.00
IPyC	thickness	35	Pyrolitic Graphite	1.90
SiC	thickness	35	Silicon Carbide	3.20
OPyC	thickness	40	Pyrolitic Graphite	1.87
Fuel Particle	diameter	847	-	-
Matrix	pitch	927	Carbon Material	1.75

Table 2-2 Material Characteristics of Fuel Assembly

Part	**Material**	$\rho(g/cm^3)$
Channel Box	C-C	1.95
Y-shape	C-C	1.95
Coolant	FLiBe	1.95@700°C
Control Blade	Mo(98.7%) Hf(1.2%) C(0.1%)	10.28

Table 2-3 Main Core Characteristics of the AHTR Reference Model

Characteristic	**Value**	**Units**
Core Thermal Power	3,400	MW
Number of Fuel Assemblies	253	-
Fuel Plates per Assembly	18	-
Fuel Enrichment	19.75	wt%
Fuel TRISO Packing Fraction	40	%
Moderator / Reflector	Graphite	-
Coolant	FLiBe (2LiF-BeF$_2$)	
Li7 enrichment	99.995	wt%
Coolant Pressure	1	atm
Inlet Coolant Temperature	650	°C
Outlet Coolant Temperature	700	°C
Coolant Volumetric Flow Rate	14.56	m^3/s
Coolant Mass Flow Rate	28,500	kg/s
Core Height	600	cm
Fueled region height	550	cm
Equivalent Core Diameter (Fueled Region)	7.81	m
Core Diameter (Including Radial Reflector)	9.56	m
Fuel assembly pitch	46.75	cm
Outer apothem	22.5	cm
Channel box wall thickness	1	cm
Y-shape thickness	4	cm
Coolant thickness between pates	0.7	cm
Coolant thickness between plate and wall	0.35	cm
Fuel plate thickness	2.55	cm
Fuel plate length	22.52	cm
Fuel Plate Sleeve Thickness	0.06	cm
Fuel Plate Fuel Stripe Thickness	0.62	cm
Fuel Plate Carbon Meat Thickness	1.20	cm
Control Blade Slot Thickness	1	cm
Control Blade Slot Wing Length	10	cm

2.2. Lattice Model

The first step in the development of the AHTR two-step procedure was the defining of a lattice physics model from which to generate homogenized cross-sections. Though SERPENT 2's continuous energy treatment of cross-section data helps reduce uncertainties and alleviate errors associated with developing a plate-cell model for the multi-group reduction, there still remains other items in model creation that must be considered and addressed. This section, albeit not exhaustive in the identification and assessment of all lattice physics modeling concerns, attempts to consider the more significant points of model accuracy and how they were addressed in this research.

2.2.1. TRISO Particle Treatment

First, and somewhat most apparent of the modeling challenges, is the accurate and expedient treatment of the TRISO particles within the fuel stripes. Due to the novelty of the AHTR fuel design, a specific fuel fabrication process has yet to be developed. Multiple methods for fabricating graphite TRISO particle compacts for cylinders and spheres have been considered including powder and particle mixture pressing, particle overcoat pressing, and molten matrix injection into random closed packed particles, each having their own strengths and challenges [52]. It was assumed for this research that the most likely manufacturing process would be the graphite over coated particle pressing technique due to its recent use in manufacturing irradiation specimens for Advanced Gas-cooled Reactors (AGRs) [53]. What is important in this assumption is that the resulting compact should be a nearly random particle dispersion with some non-random packing clustering near the dye wall as shown in Figure 2-1. In theory it may be possible to pre-structure the particles into a hexagonal closed-pack prior to compression which would help to achieve packing fractions near 50% post compression, but it is likely that the uniform arrangement will not be perfectly maintained during compression, and so the random dispersion assumption still likely accurate [54].

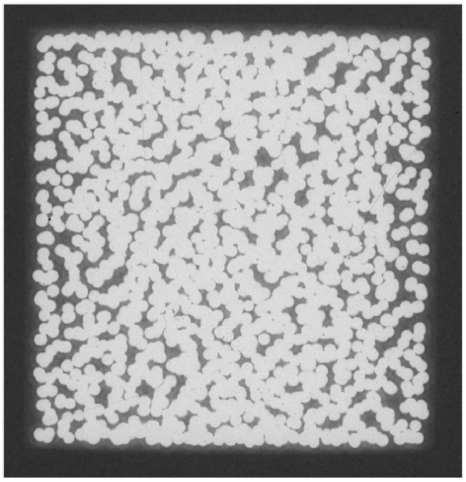

Figure 2-1 X-ray radiograph of an AGR-3/4 compact [53]

Given that the actual dispersion will be mosty random, it was then believed that the most accurate approach for modeling the particles would be by explicitly treating each particle individually in a random dispersion. SERPENT 2 provides a random dispersion module for the generation of random dispersion realizations, and has sufficient geometry definitions to meet the needs of this research as shown in Figure 2-2. Though this method was believed to be the most faithful to what would be the actual fuel geometry it suffered from longer runtimes due to the detailed tracking of individual particle locations and the requirement of several realizations to obtain a representative average [55].

Because of the demands on runtime accompanying the multiple realizations of a random dispersion treatment, an alternative regular lattice particle arrangement was considered as shown in Figure 2-3. It should be noted that this lattice treatment allowed clipping of particles at the stripe edges for the sake of model simplicity, and that subsequently the particle lattice pitch was adjusted to ensure the correct fuel volume representation. Such a treatment removes the statistical aspect of the random dispersion realization and alleviates the need for multiple realization for an average representation, but also introduced possible sources of error from alteration of the local fuel-to-moderator ratio, provision of streaming paths along the lattice planes, and of course the unphysical clipping of particles [56].

To assess the significance of this error, five random dispersion realizations were simulated and compared against the regular lattice particle arrangement. As can be seen in Figure 2-4 the difference in reactivity between random dispersion and regular lattice treatments are not insignificant, in some cases exceeding 300±43 pcm, but are not so large as to invalidate the regular lattice treatment. More importantly though is the comparison of the assembly averaged flux spectrum presented in Figure 2-5 wherein the spectra appear to be nearly identical between the random dispersion realizations and the regular lattice arrangement at beginning of cycle (BOC) conditions. This is believed to be indicative that few group homogenized cross-sections generated using a regular lattice particle arrangement will be very similar to cross-sections generated from a random dispersion treatment, and so justifies the use of a regular particle arrangement. It should be noted for completeness that the one-standard deviation Monte Carlo statistical uncertainties for the flux spectrum were predominantly <0.1% Relative Standard Error (RSE) with the exception of the very low flux regions where uncertainties were as high as 11% RSE.

With these results it was decided that an explicit treatment of individual TRISO particles could most expediently and accurately be simulated using a regular lattice arrangement. In addition to this treatment, a common runtime reduction technique of partial homogenization of particle coatings (i.e. homogenizing buffer / IPyC layers together and OPyC / matrix together), was utilized to reduce transport runtimes while maintaining reactivity and flux characteristics effectively unaltered [57]. Figure 2-6 shows that the error introduced by partial coating homogenization, and in fact also full coating homogenization, is essentially negligible (Note: error uncertainties for both cases were less than 43 pcm). Partial homogenization was chosen rather than full homogenization to maintain some level of consistency with the ORNL study which employed only partial homogenization when considering explicit TRISO particle treatment.

Other techniques that were reviewed in this research for the treatment of TRISO particles included the Chord Length Sampling technique, a Collision Probability treatment, the SCALE-NEWT Double Het treatment, and the SERPENT 2 implicit TRISO model treatment [34, 57, 58]. However, each of these were ultimately rejected on the grounds of either insufficient theoretical or implementational maturity.

Additionally, the RPT method described in Section 1.3 was considered as a possible runtime reduction technique and was partially utilized in the energy group optimization portion of this research as will be discussed later, but was ultimately decided against in the cross-section generation model on account of its lack of physicality and added necessity of equivalency parameter search.

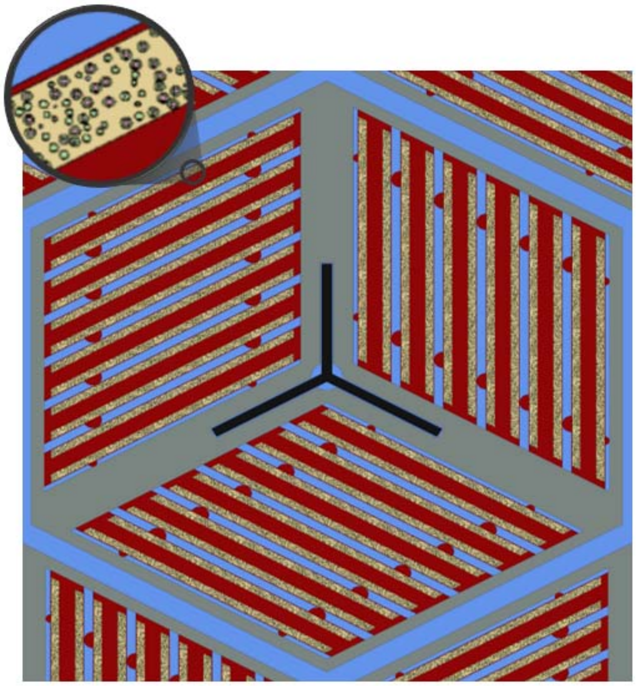

Figure 2-2 SERPENT 2 Model of AHTR Fuel Assembly with randomly dispersed TRISOs

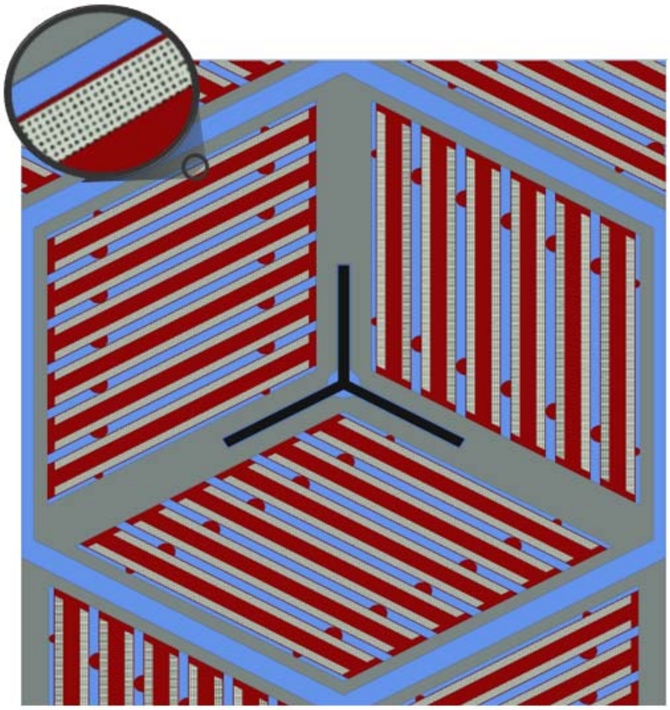

Figure 2-3 SERPENT 2 Model of AHTR Fuel Assembly with regular lattice TRISOs

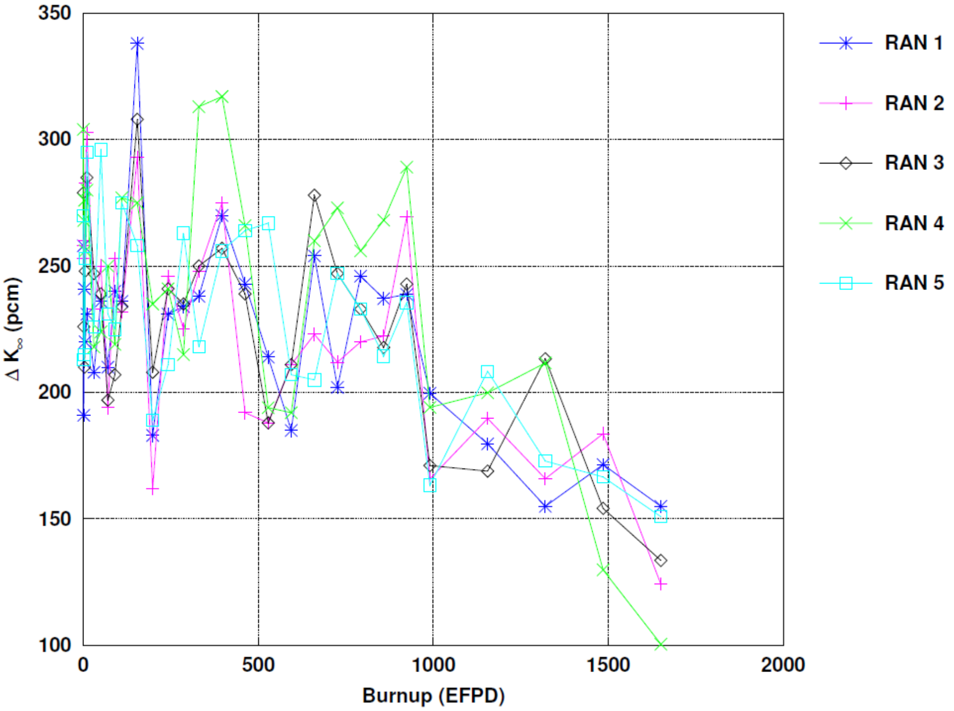

Figure 2-4 K-infinite Difference between Regular Lattice and Random Dispersion

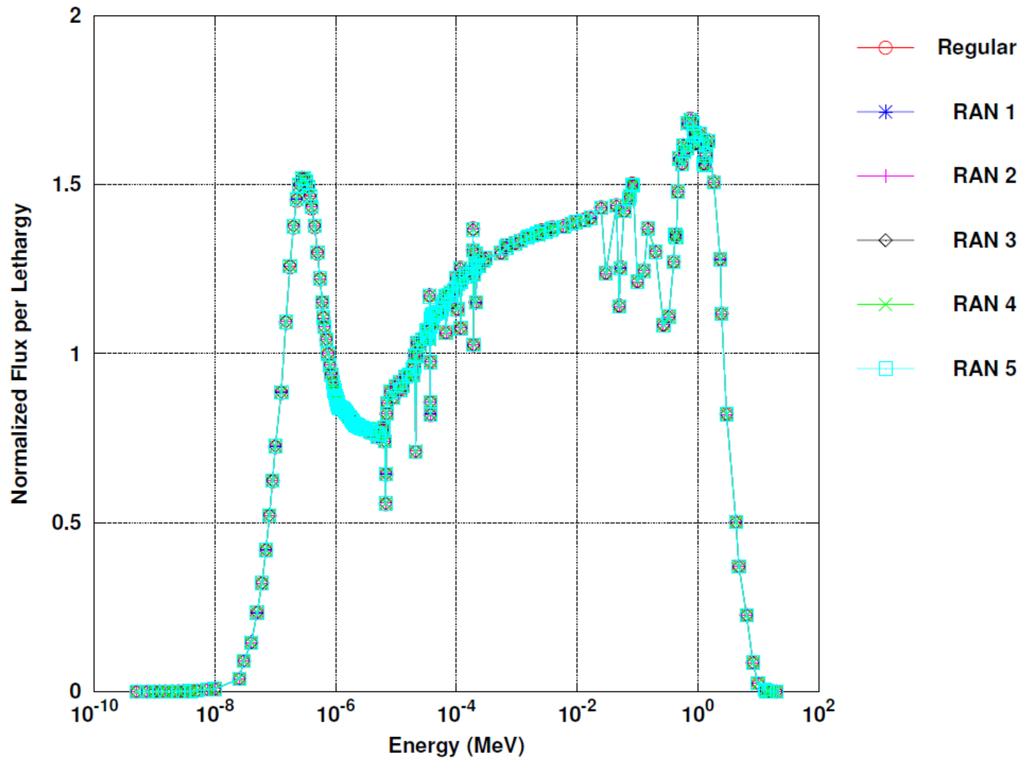

Figure 2-5 BOL Flux Spectrum of Regular Lattice and Random Dispersion

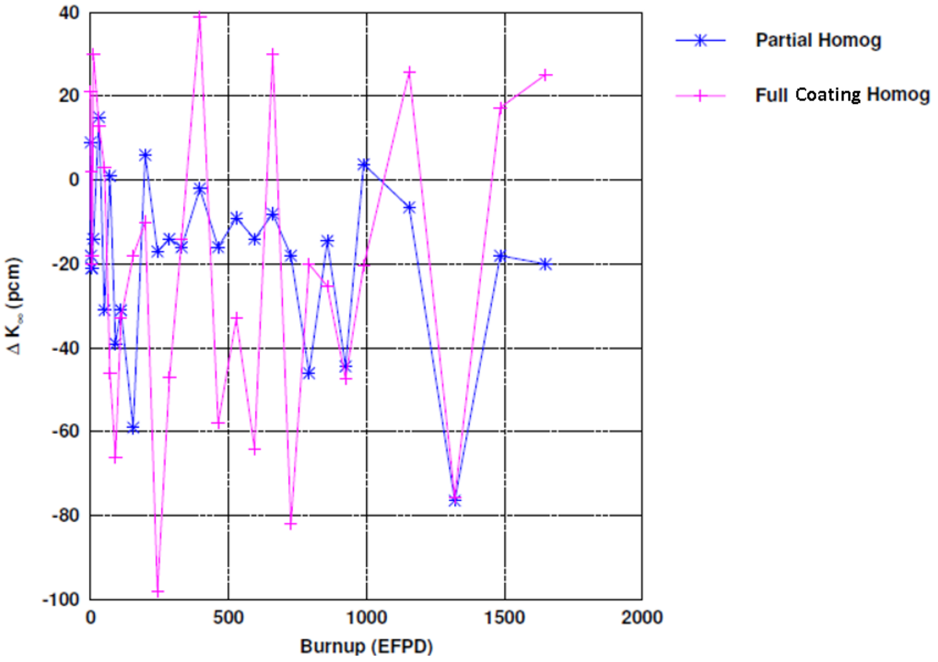

Figure 2-6 Error of Partial and Full Coating Homogenization Compared to Full Coating Treatment

2.2.2. Depletion Region Subdivision Mesh Refinement

Much as in the case of LWRs, one must consider the level of subdivision of depletion regions necessary in order to ensure accuracy. Individual depletion of every fuel TRISO particle is not only an impractical endeavor but rather an impossible one due to the memory restrictions of current computers. As such, some degree a fuel depletion lumping will be necessary to make the simulation problem tenable. Practicality dictates that not only should fuel lumping be employed to make the simulation obtainable, but also expedient where at all possible, meaning increasing the degree of lumping to optimize runtime and memory usage with respect to model accuracy. As such, this important concern for developing an accurate two-step procedure was considered in this research.

To assess the impact of fuel depletion, lumping models were created with varying degrees of lumping ranging from 2 depletion zones for a given assembly, one representing plate top stripes and the other plate bottom stripes, all the way to 329 depletion zones with 9 depletion zones for each stripe. Depletion zone subdividing was generally performed only along the length of stripes rather than the thickness of stripes given that the stripes width is relatively thin compared to the stripe length. An illustration of the stripe depletion subdivision is presented in Figure 2-7.

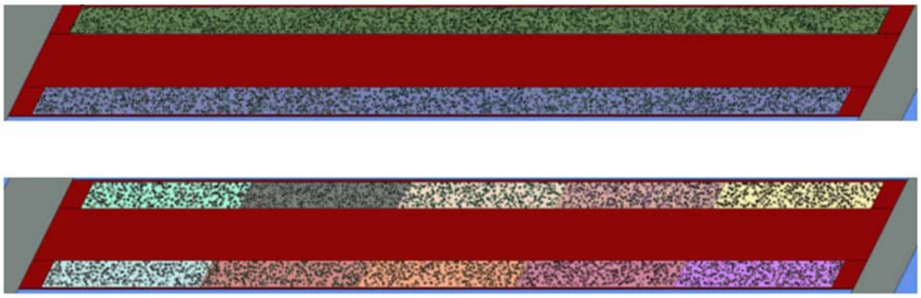

Figure 2-7 Illustration of Lumped Depletion(top) vs. Stripe Subdivided Depletion (bottom)

A comparison of model reactivity was made using the different levels of depletion subdivision, the results of which can be observed in Figure 2-8. To clarify the labeling of the results, “Lumped” refers to two depletion regions for the entire model, one for all instances of the “upper” fuel stripe within all plate and one for all instances of the “lower” fuel stripe within all plates. Furthermore, cases labeled as “Subd” denote the number of subdivisions applied along the length of every stripe, implying that all stripe instances are depleted independently and are then further subdivided. Since each of 3 tri-sections in an assembly has 6 plates with 2 stripes each, this corresponds to 3x6x2=36 stripes per fuel assembly. So, for “Subd 1” 36 depletion regions were simulated, one for each stripe, whereas for “Subd 9” 329 depletion regions were simulated, 9 for each stripe.

It can be observed in the results that model differences with respect to the Subd 9 model generally increased with accumulating burnup and are largest for cases with the fewest lumped depletion zones. However, the error even for two depletion zone model was not extraordinarily large and this quickly decreased in magnitude as the number of depletion zones was increased (Note: again error uncertainties were less than 43 pcm). Ultimately, five subdivisions per stripes, totaling 180 total depletion zones, was deemed to be sufficiently accurate for lattice physics simulations without demanding an overwhelming amount of computer memory and runtime. It should be noted that another parameter of interest that should be considered in future studies of depletion region refinement is the stripe-wise power distribution, which was not investigated in this study.

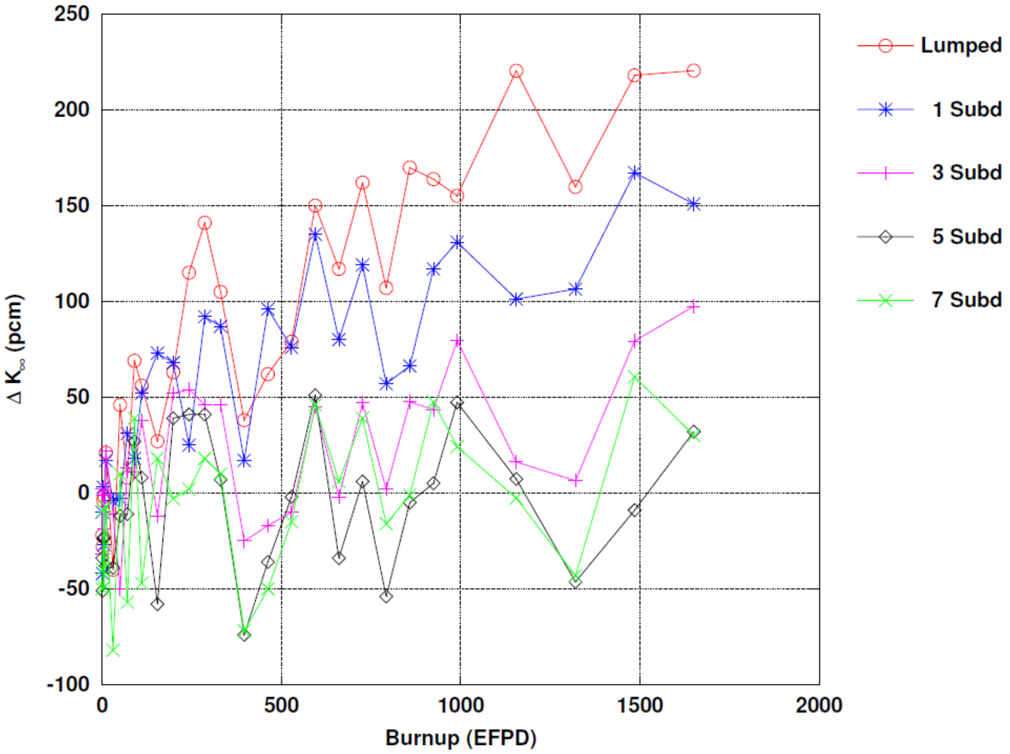

Figure 2-8 K-infinity Difference versus 9 Depletion Sub-divisions per Fuel Stripe

2.2.3. Assessment of Photo-nuclear Effects

One important current shortcoming of the SERPENT 2 code that warranted investigation is the lack of capability for simulating coupled photo-nuclear reactions. The ^{9}Be isotope which is a constituent of the FLiBe coolant exhibits a few notable photo-neutron reactions, as illustrated by the cross-section profiles in Figure 2-9, that the SERPENT 2 code currently does not treat. Therefore, a 2-D single assembly model was created and simulated using the Monte Carlo code MCNP6 to assess the potential photo-nuclear effects [59].

As can be seen in Table 2-4, the MCNP6 simulation with photo-nuclear physics tracking NP mode has an essentially identical reactivity as the N mode simulation with tracking of only neutron interactions. Thus, indicating that the photo-neutron reactions of ^{9}Be are not large enough to call into question the accuracy of the SERPENT 2 model with regards to the absence of photo-nuclear effects. It should be noted that the SERPENT 2 difference with MCNP6 is slightly higher than expected, but still believed sufficiently small such that it might be attributed to minor differences in model setup and not a need for concern. Possible explanations for this difference could either be small inconsistencies in cross-section treatment or a small shifting of the regular lattice TRISO grid in the MCNP6 model such that the particle clipping and subsequently fuel volume was altered. Again, the error was thought to be sufficiently small such that the exact cause for the difference was not pursued.

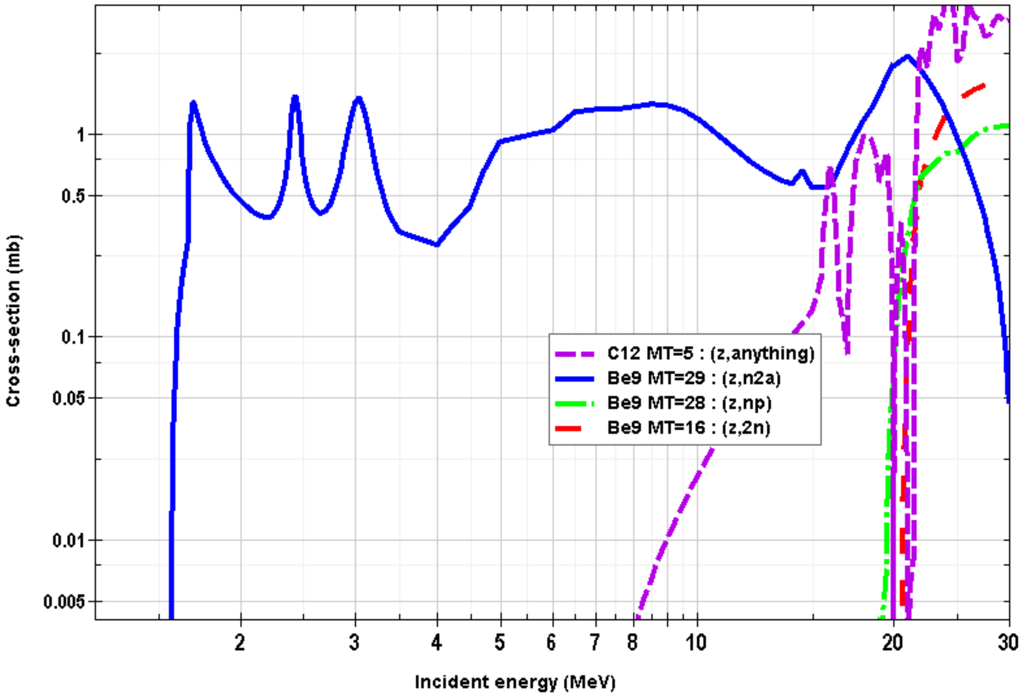

Figure 2-9 Gamma Cross Sections of Interest for AHTR [31]

Table 2-4 Assessment Photo-Nuclear Effects

MCNP 6.1 NP mode k-inf	MCNP 6.1 N mode diff (pcm)	SERPENT 2 diff (pcm)
1.35587 +/- 10	16 +/- 14	232 +/- 20

2.3. Energy Group Optimization

In this section the manner in which the few-group energy group structure is both constructed and optimized is discussed. The optimization was performed under the premise of ensuring the accuracy of the infinite assembly approximation for a variety of core conditions. It should be noted that the MOC deterministic code KARMA along with the aforementioned RPT technique were used for this optimization due to the large number of core models considered and the expediency with which they must be accomplished. KARMA and RPT were used for the few-group optimization only and were not used in any other portions of this research.

As discussed previously, longer diffusion lengths, altered flux spectrum, and the presence of strong flux discontinuities near the reflector all challenge the original few-group energy group structure used in traditional LWR two-step procedures. One solutions for this would be to consider larger assembly super cells rather than single assemblies to properly account for the neighbor effects and discontinuities. However, this would entail generating cross-sections libraries for all the foreseeable combinations of assemblies and reflector blocks which is both cumbersome and time consuming.

One of the more practical alternatives to larger lattice physics cells is to simply allow additional energy groups in the few group structure. The addition of supplementary energy groups to the few group structure reduces the error of the infinite single assembly condensation by allowing the resolution of cross-sections energy dependencies that are important to spectrum effects associated with assembly neighborhood heterogeneity. An algorithm for determining coarse energy group structure for homogenized cross-sections was proposed by Kim et. al. for the VHTR, which was subsequently presumed applicable to AHTR and employed in this research [60].

In this algorithm, core models are simulated for a variety of expected representative operating conditions, such as various fuel burnup profiles, operating temperatures, control blade insertion patterns, and a multitude of other possible core configurations. Similarly, single infinite assembly models are also simulated to span the possible assembly configurations, considering assembly burnup, operating temperature, control rod position, etc.

In all full core and single assembly simulations, multi-group collapsed values (typically 100+ energy groups but for this research 190 energy groups) for assembly zone wise fluxes, absorption cross-section, and $\nu \cdot \Sigma_{fiss}$ cross sections are edited for use in optimization. Such a fine group structure should result in a near equivalency between the cross-sections created from the infinite single assembly cases as compared to assemblies of the same design and operating conditions from the full core model. Essentially, one should be able to replace the homogenized cross-sections of the full core assembly with that of the equivalent infinite single assembly and obtain nearly identical results in a diffusion simulation.

But 190 groups is still too fine to use in production level diffusion based full core analysis and so this must be further condensed, while still preserving accuracy. This is accomplished in the algorithm as follows:

1. Starting with the highest energy group, attempt to condense this energy group with the next lowest energy group as follows in all models:

$$\phi_{G_k,i} = \sum_{g=g_{k1}}^{g_{k2}} \phi_{g,i}$$

$$\Sigma_{a,G_k,i} = \frac{\sum_{g=g_{k1}}^{g_{k2}} \Sigma_{a,g,i}\phi_{g,i}}{\phi_{G_k,i}} \qquad \nu\Sigma_{f,G_k,i} = \frac{\sum_{g=g_{k1}}^{g_{k2}} \nu\Sigma_{f,g,i}\phi_{g,i}}{\phi_{G_k,i}} \tag{2-1}$$

   where,

   $\phi_{g,i}$ = scalar flux of group g in assembly zone i,

   $\phi_{G_k,i}$ = collapsed flux of combined group G_k in assembly zone i,

   $\nu\Sigma_{f,g,i}$ = macroscopic nu-fission cross-section of group g in assembly zone i,

   $\nu\Sigma_{f,G_k,i}$ = collapsed macroscopic nu-fission cross-section of group G_k in assembly zone i,

   $\Sigma_{a,g,i}$ = macroscopic absorption cross-section of group g in assembly zone i,

   $\Sigma_{a,G_k,i}$ = collapsed macroscopic absorption cross-section of group G_k in assembly zone i.

2. In the core models, calculate energy group and assembly zone wise reaction rates for both absorption and nu-fission (i.e. neutron generation) reactions:

$$\mathrm{R}_{a,G_k,i} = \Sigma_{a,G_k,i}\phi_{G_k,i} \qquad \mathrm{R}_{f,G_k,i} = \nu\Sigma_{f,G_k,i}\phi_{G_k,i} \tag{2-2}$$

3. Calculate reaction rates again in the core model but this time substitute the macroscopic cross-sections for the assembly zones with the infinite assembly model macroscopic cross-sections corresponding to the matching core conditions (i.e. burnup, control blade insertion, etc.)

$$\mathrm{R'}_{a,G_k,i} = \Sigma'_{a,G_k}\phi_{G_k,i} \qquad \mathrm{R'}_{f,G_k,i} = \nu\Sigma'_{f,G_k}\phi_{G_k,i} \tag{2-3}$$

where,

$\Sigma'_{a,G_k} =$ Infinite Assembly macroscopic absorption cross-section of group G_k,

$\nu\Sigma'_{f,G_k} =$ Infinite Assembly macroscopic absorption cross-section of group G_k,

$\phi_{G_k,i} =$ collapsed flux of combined group G_k from full core model assembly zone i.

4. Assess the difference between the core model reaction rates and the infinite assembly substituted reaction rates for all assembly zones i and energy groups g where total number of zones is I and energy groups G, and determine the significance of the differences with regards to the core model global reactivity

$$\Delta\mathrm{R}_{a,G_k,i} = \mathrm{R}_{a,G_k,i} - \mathrm{R'}_{a,G_k,i} \qquad \Delta\mathrm{R}_{f,G_k,i} = \mathrm{R}_{f,G_k,i} - \mathrm{R'}_{f,G_k,i}$$

$$\mathrm{E}_{a,G_k,i} = \frac{\sum_{g=1}^{G}\sum_{i=1}^{I}\Sigma_{a,g,i}\phi_{g,i}}{\sum_{g=1}^{G}\sum_{i=1}^{I}\nu\Sigma_{f,g,i}\phi_{g,i}} - \frac{\left(\sum_{g=1}^{G}\sum_{i=1}^{I}\Sigma_{a,g,i}\phi_{g,i}\right) - \Delta\mathrm{R}_{a,G_k,i}}{\sum_{g=1}^{G}\sum_{i=1}^{I}\nu\Sigma_{f,g,i}\phi_{g,i}} \tag{2-4}$$

$$\mathrm{E}_{f,G_k,i} = \frac{\sum_{g=1}^{G}\sum_{i=1}^{I}\Sigma_{a,g,i}\phi_{g,i}}{\sum_{g=1}^{G}\sum_{i=1}^{I}\nu\Sigma_{f,g,i}\phi_{g,i}} - \frac{\sum_{g=1}^{G}\sum_{i=1}^{I}\Sigma_{a,g,i}\phi_{g,i}}{\left(\sum_{g=1}^{G}\sum_{i=1}^{I}\nu\Sigma_{f,g,i}\phi_{g,i}\right) - \Delta\mathrm{R}_{f,G_k,i}}$$

5. If the differences for all full core models and their associated assembly zones is below some designated acceptance criteria (i.e. 150 pcm), then let the combined energy group remain and return to step 1 with the new combined energy group as the new “high” group.

   Otherwise, do not combine the groups and return to step 1 with the next lowest energy group now representing the new “high” group

6. Repeat steps 1 through 5 until all energy groups have been considered for condensation

In this manner one can systematically determine a condensed energy group structure that will ensure a certain level of accuracy via preservation of reaction rates when using an infinite assembly based cross-section set in a diffusion full core simulation.

Though this algorithm is fairly simple in conception, accurate and expedient implementation can prove difficult. To obtain a truly optimized energy group structure with absolute confidence that it will apply to all operating conditions, one would need to apply the algorithm to full 3-D core models spanning all possible operating conditions . This of course would be a practical impossibility and ultimately defeat the purpose of the two-step procedure which is to avoid multiple detailed transport full core simulation. Therefore it is best to focus on only select state conditions which generally approximate and / or bound most expected operating conditions.

Figure 2-10 through Figure 2-14 show the impact of various operating conditions on the flux spectrum of a single infinite assembly model. It can be observed that changes in plate temperature (i.e. both fuel and non-fuel plate material), insertion of a control blade, and burnup of fuel all have a significant influence on the flux spectrum and so warrant consideration in energy group optimization. Coolant temperature and density changes on the other hand appear to have a negligible effect on flux spectrum and so can be ignored.

Limiting the analysis to only those physical parameters of significant influence helps to reduce the scope of conditions that must be considered, however this alone is still insufficient in making the energy group optimization problem tenable. Considering even in a 2-D model there are 253 assembly locations in the core, each that could possibly have different operating states, it can still be seen that an extraordinary number of simulations could be devised to cover all possible operating states. To help lessen this complexity even further, the 2-D full core model can be reduced to a representative semi1-D full core model such as illustrated in Figure 2-15. This is considered as semi 1-D model because the TRISO particles are modeled in SERPENT 2 as true spheres with full 3-D representation, but with the enclosing macro-geometry having reflective boundary conditions in all directions except the radial direction.

Looking at Figure 2-16 it can be seen that the flux spectrum of the central fuel assembly in the 1-D model matches fairly well the flux spectrum of the central fuel assembly in the 2-D model, which is important because most assemblies in a uniform reactor experience nearly the same flux spectrum as the central assembly as show in Figure 2-17. Figure 2-18 though shows some difference between the peripheral assembly flux spectrum of the 1-D and 2-D full core models, and though the difference is notable it is not believed to be so large as to invalidate the use of the 1-D model as a means of performing energy group optimization analysis.

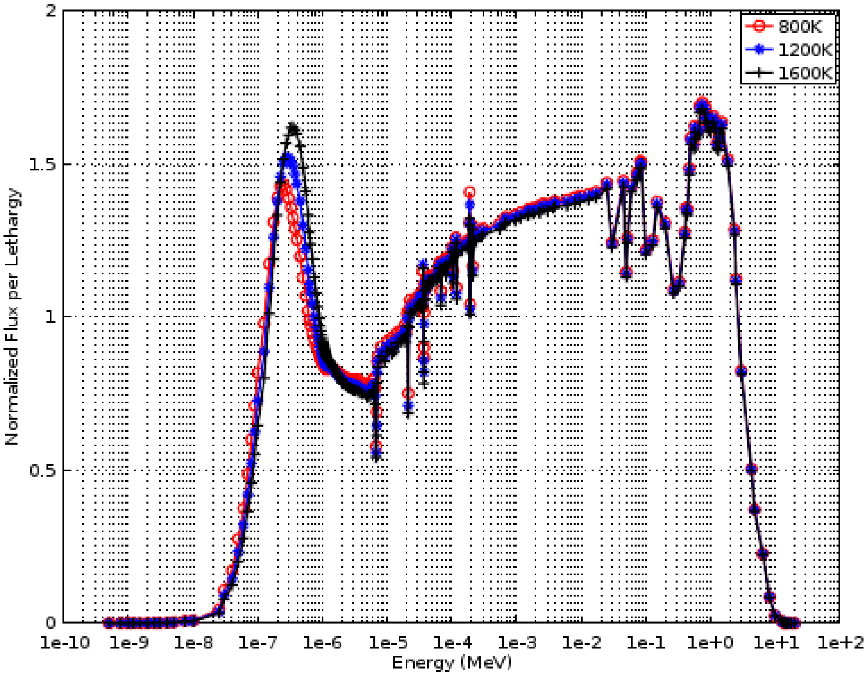

Figure 2-10 Spectrum Effects of Changing Plate Temperature in SERPENT 2 2-D Single Assembly Models

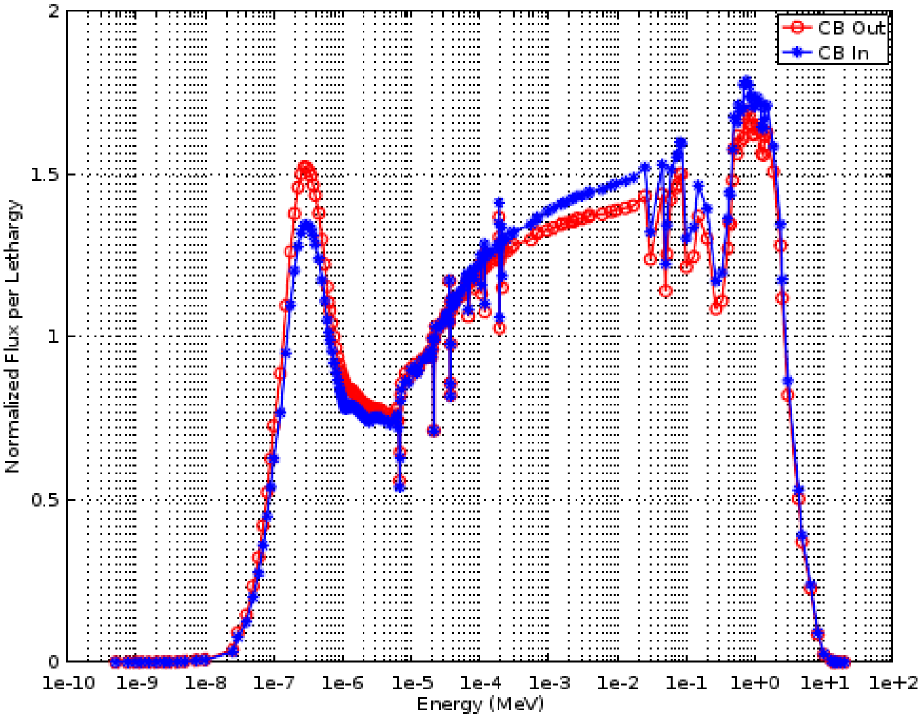

Figure 2-11 Spectrum Effects of Control Blade Insertion in SERPENT 2 2-D Single Assembly Models

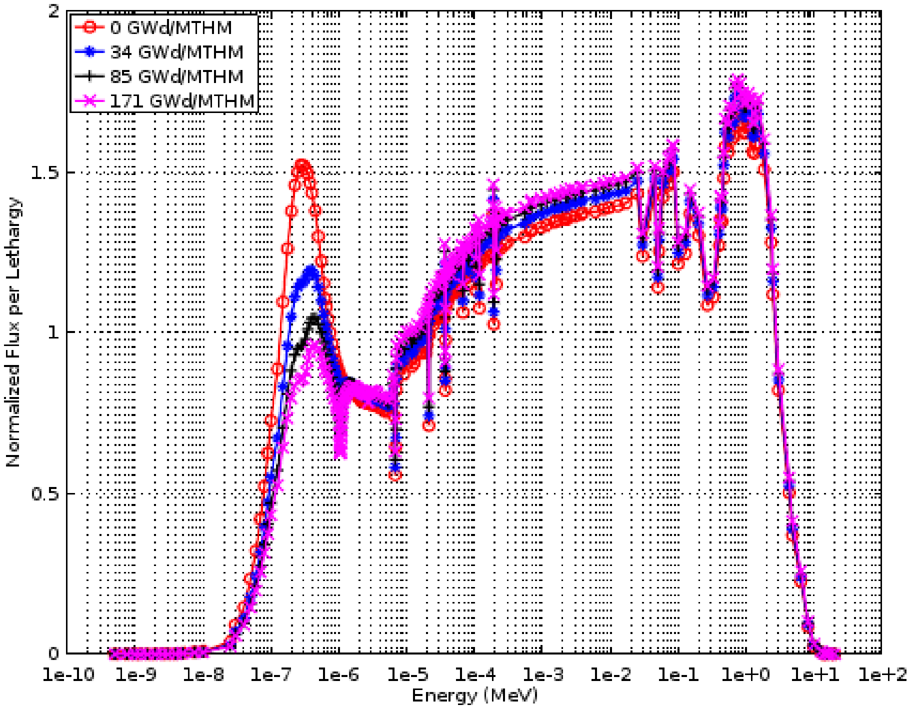

Figure 2-12 Spectrum Effects of Fuel Burnup in SERPENT 2 2-D Single Assembly Models

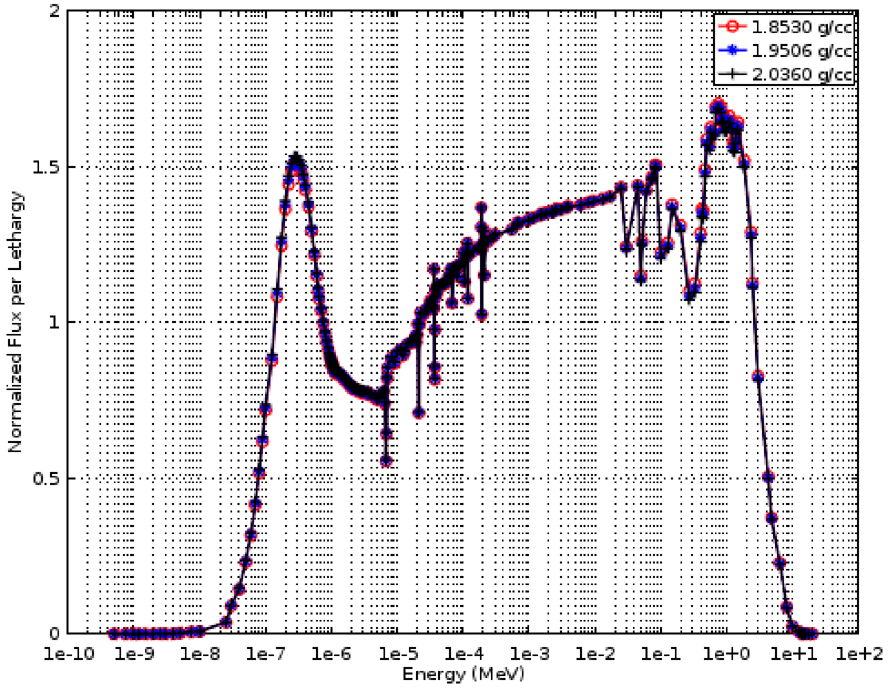

Figure 2-13 Spectrum Effects of Changing Coolant Density in SERPENT 2 2-D Single Assembly Models

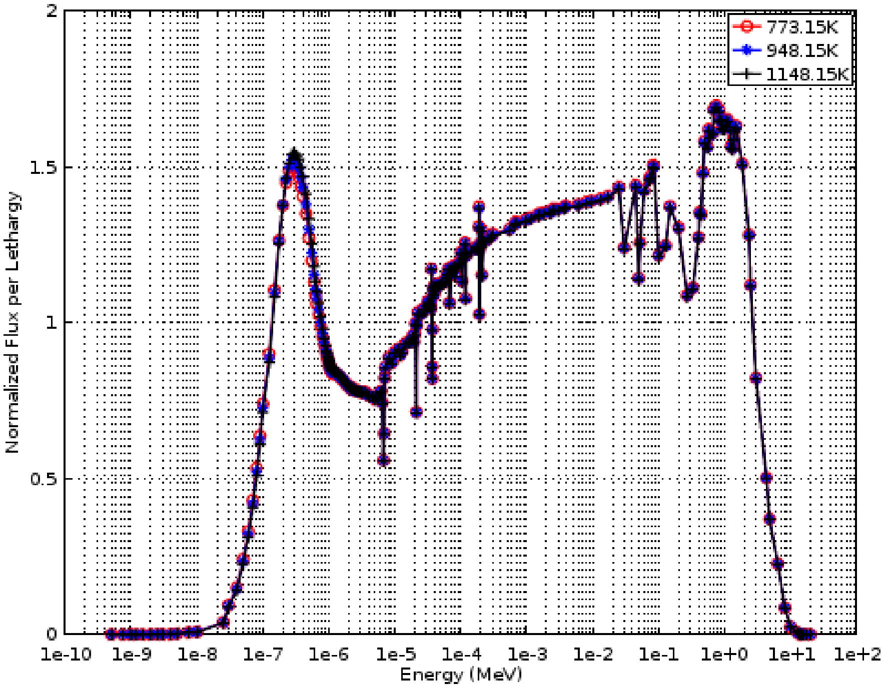

Figure 2-14 Spectrum Effects of Changing Coolant Temperature in SERPENT 2 2-D Single Assembly Models

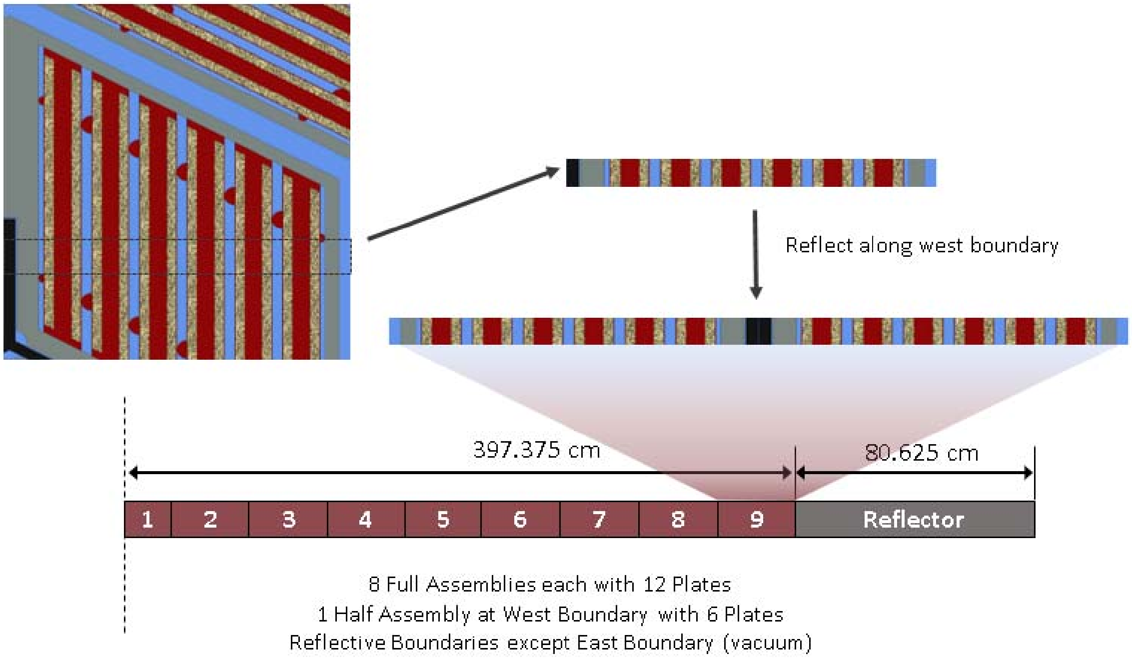

Figure 2-15 Depiction of Semi 1-D Model

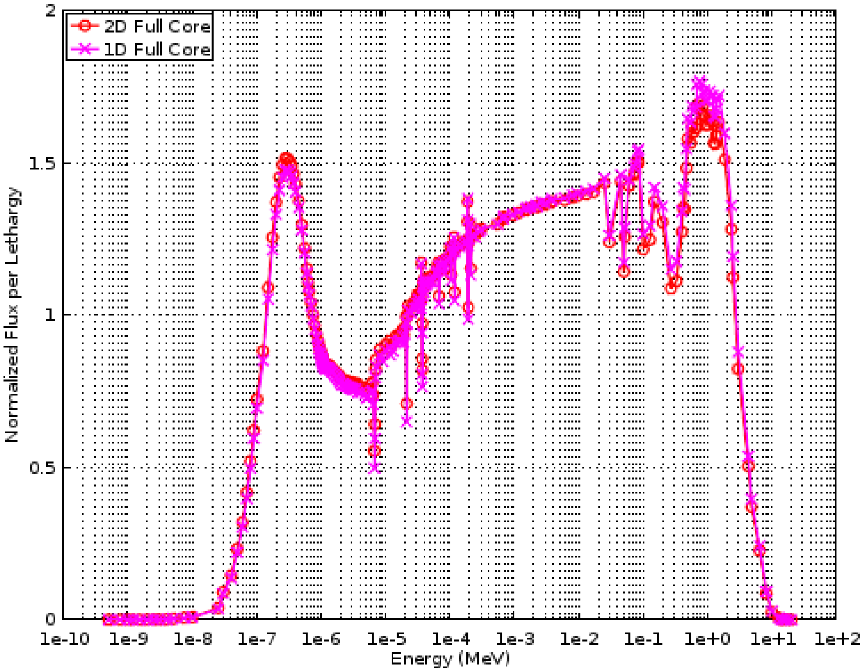

Figure 2-16 Central Assembly Flux Spectrum Comparison Between SERPENT 2 2-D and 1-D models

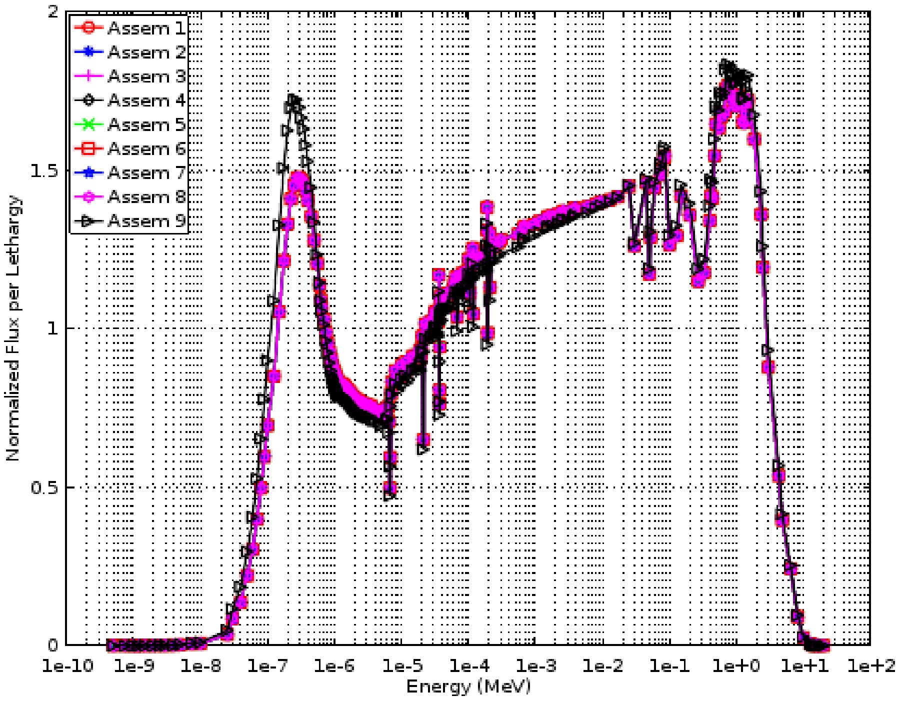

Figure 2-17 Flux Spectrum of Individual Assemblies in SERPENT 2 1-D Full Core Model

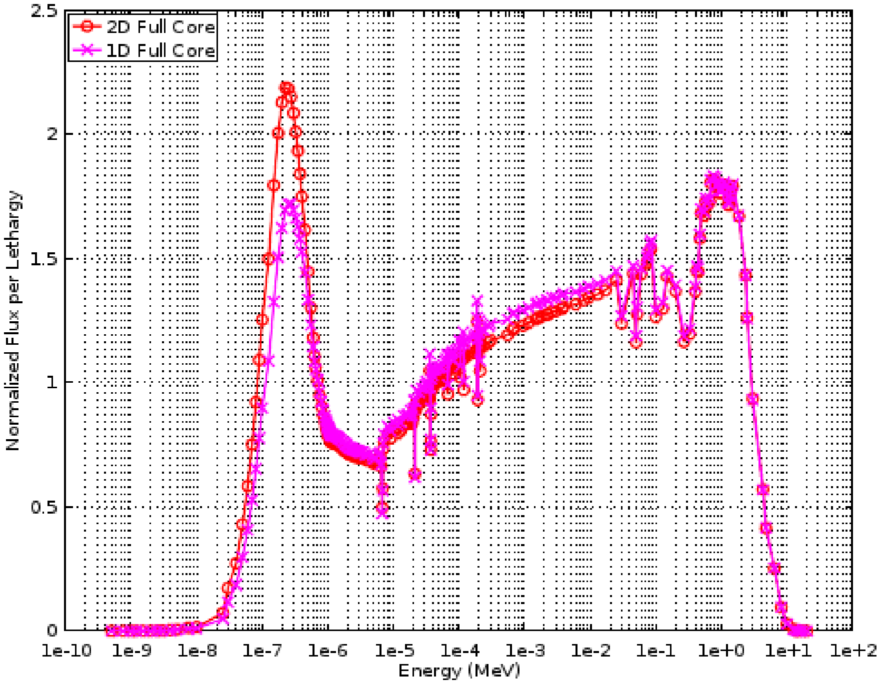

Figure 2-18 Peripheral Assembly Flux Spectrum Comparison Between SERPENT 2 2-D and 1-D models

Following the notion that most assemblies in a uniform core experience a similar flux spectrum as the central assembly, it may then be possible to further reduce the 1-D model from a true full core model to a smaller mini-core model as shown in Figure 2-19. It can be seen in Figure 2-20 that this assumption does indeed hold very well with good spectrum agreement between the interior fuel assemblies and periphery fuel assemblies of the two 1-D models

For the energy group optimization analysis of this research, all these approximations were applied so as to reduce the number of necessary models to capture the effects of various operating conditions to within some tenable amount. Select simplified mini-core operating conditions were simulated with consideration to assembly burnup, fuel temperature, and control blade insertion so as to attempt to reasonably span a representative set of potential core configurations. This is partially represented in Figure 2-21 where in the different configurations illustrated were tested at multiple temperature conditions ranging from 300 K to 1500 K and burnup conditions. Again, it is not possible to cover all possible operating conditions and so some limited subset of the likely conditions must suffice.

Due to the large number of cases under consideration along with the somewhat relatively longer runtimes of SERPENT 2, an alternative transport code was sought to help hasten the simulation time. The Method of Characteristics code KARMA was employed for this purpose and was able to quickly perform the simulations for these various cases in only a few hours [61]. In order to utilize KARMA, an RPT equivalent model was created which agreed with the reference SERPENT 2 1-D zero burnup model within 250 pcm and with essentially an identical flux spectrum behavior. Although RPT, as previously mentioned, does incur some error, it is believed that this error will likely have little effect on the group structure optimization. Essentially, the RPT error should not greatly influence the flux spectrum to the point where significant changes in group boundaries will result. Again, the use of KARMA and RPT were applied only to the energy group optimization, and only out of absolute necessity for simulation expediency. After generating 190 group collapsed flux and cross-section results for the various models the aforementioned energy group optimization algorithm was used to determine an optimal few-group energy group structure. It should be noted that though control blade inserted mini-core models were considered, only the non-controlled assemblies within these models were used in the optimization. The reason for this is that the proper treatment of non-controlled neighbors on controlled assemblies was captured using an alternative method as described in Section 2.5.

Using the aforementioned optimization algorithm along with the various Mini-Core models a 13 group structure, shown in Table 2-5, was obtained with group wise reaction rate errors below 170 pcm. This error actually represents the lowest reaction rate error achievable by the algorithm with these AHTR models due to select cases of the infinite assembly approximation exhibiting errors of 170 pcm for a single energy group in the fine energy group structure. Essentially, if no energy group condensation were performed, the maximum error of the infinite assembly approximation would be 170 pcm, which the algorithm cannot improve on. Though this structure obtains a reasonably acceptable reaction rate error, it was believed to be comprised of an excessive number of energy groups being that for VHTR, a reactor with a considerably longer diffusion length, optimized group structures consist of only 10 energy groups and VHTR [60]. Additionally, the NESTLE core simulator is limited to a maximum allowable energy group structure size of 4 energy groups, which necessitates further condensation of the energy group structure. Therefore, manual manipulation of group boundaries was performed and produced a 4-group structure listed as “Option 1” in Table 2-6.

It can be seen by looking at Figure 2-22, Figure 2-23, and Figure 2-24 (model number index listed in Table 2-7) that this manual 4-group structure performed generally better than the 13 group structure in most models. Reaction rate errors were calculated on the basis of L2-norm differences. Also, it should be noted that model eigenvalues for were calculated using the summation of $\nu\Sigma_f$ reactions over the summation of Σ_a reactions of all fuel zones. The reason for this discrepancy between the optimization algorithm and manual manipulation is that the aforementioned algorithm fails to capture the idea of error cancellation wherein some reaction rate over approximation is cancelled by reaction rate under approximation. By taking this error cancelling notion into consideration, one can strategically select group boundaries, sometimes “sooner” than what the algorithm would have chosen, such that coarser group structures can be obtained. Even though one could likely obtain even better accuracy with additional energy groups and manual determination of group boundaries, the limitations of NESTLE prevented pursuing a finer group structure than 4 groups. It should be noted that an N-Group version of NESTLE is nearing completion at this time and should be employed in future studies to test a larger number of energy groups.

An additional 4-group structure, Option 2, is presented in Table 2-6 and its associated error. It can easily be seen that this group structure performs considerably worse than Option 1 and the 13 group structure and so would not be worth consideration. However, there is reason for it and the motivations for deriving it will be discussed on more detail in Section 2.4.

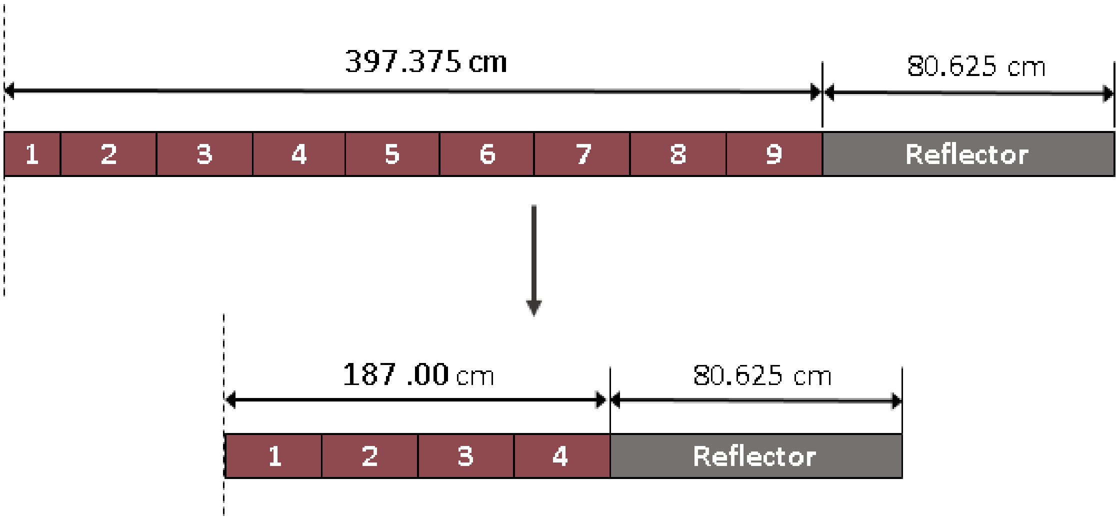

4 Full Assemblies each with 12 Plates
Reflective Boundaries except East Boundary (vacuum)

Figure 2-19 Illustration of 1-D Mini-Core Simplification

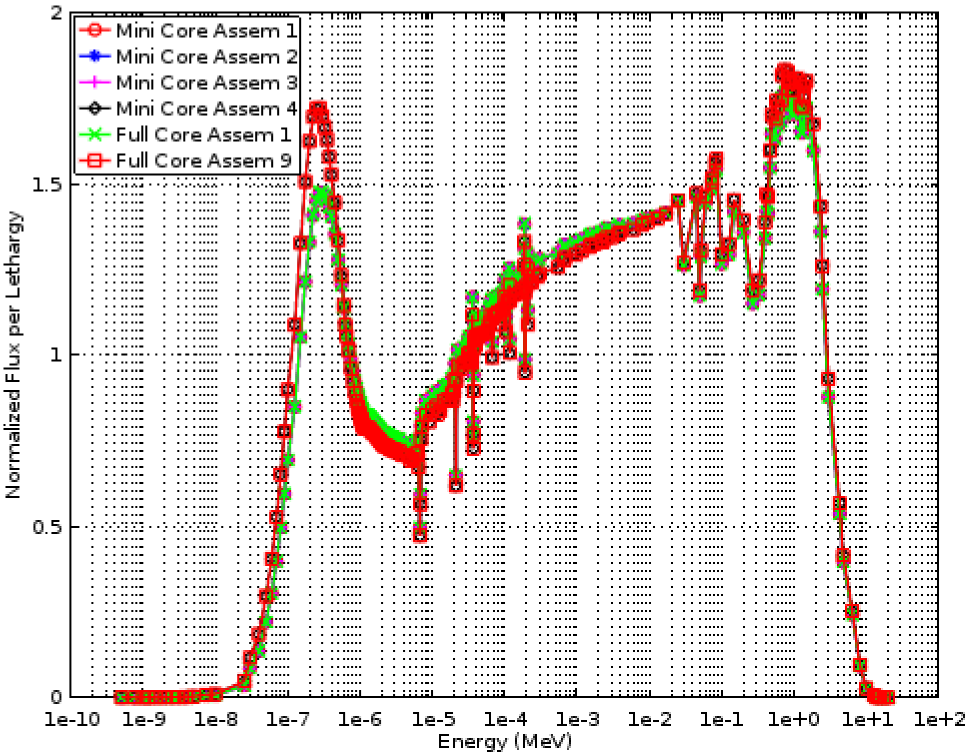

Figure 2-20 Comparison of SERPENT 2 1-D Full Core and 1-D Mini Core Flux Spectrum

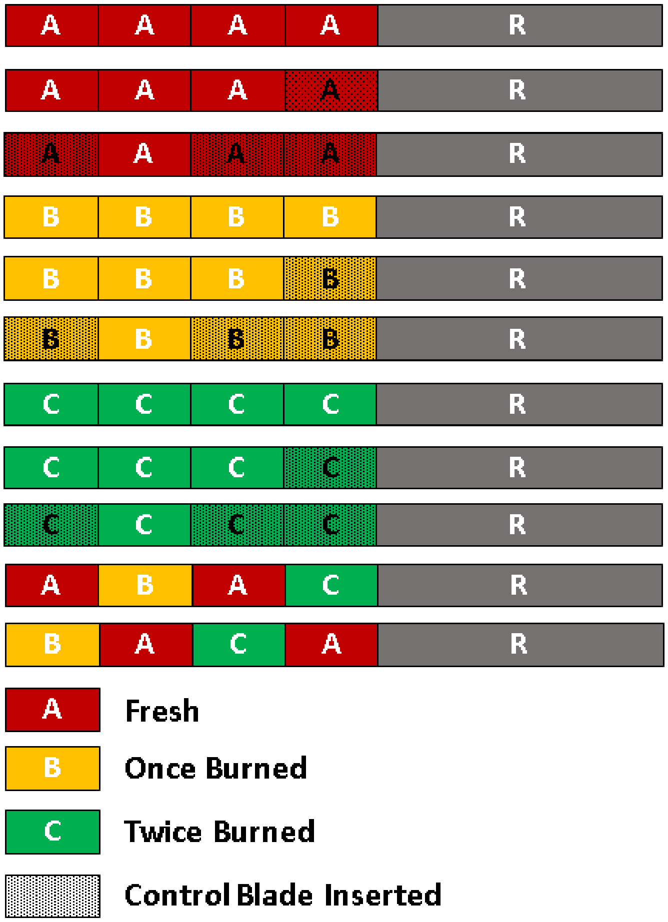

Figure 2-21 Mini-Core Model Arrangements

Table 2-5 13-Group Few Group Structure

	Group Boundaries (MeV)	
Group #	Upper Bound	Lower Bound
1	2.0000E+01	1.4739E-04
2	1.4739E-04	4.5000E-07
3	4.5000E-07	2.9074E-07
4	2.9074E-07	2.5103E-07
5	2.5103E-07	2.2769E-07
6	2.2769E-07	1.8443E-07
7	1.8443E-07	1.4572E-07
8	1.4572E-07	1.1157E-07
9	1.1157E-07	8.1968E-08
10	8.1968E-08	5.6922E-08
11	5.6922E-08	3.5500E-08
12	3.5500E-08	1.2396E-08
13	1.2396E-08	1.0000E-12

Table 2-6 4-Group Few Group Structures

	Group Boundaries (MeV)			
	Option 1		Option 2	
Group #	Upper Bound	Lower Bound	Upper Bound	Lower Bound
1	2.0000E+01	9.1188E-03	2.0000E+01	9.1188E-03
2	9.1188E-03	2.9023E-05	9.1188E-03	2.9023E-05
3	2.9023E-05	7.3000E-07	2.9023E-05	1.8554E-06
4	7.3000E-07	1.0000E-12	1.8554E-06	1.0000E-12

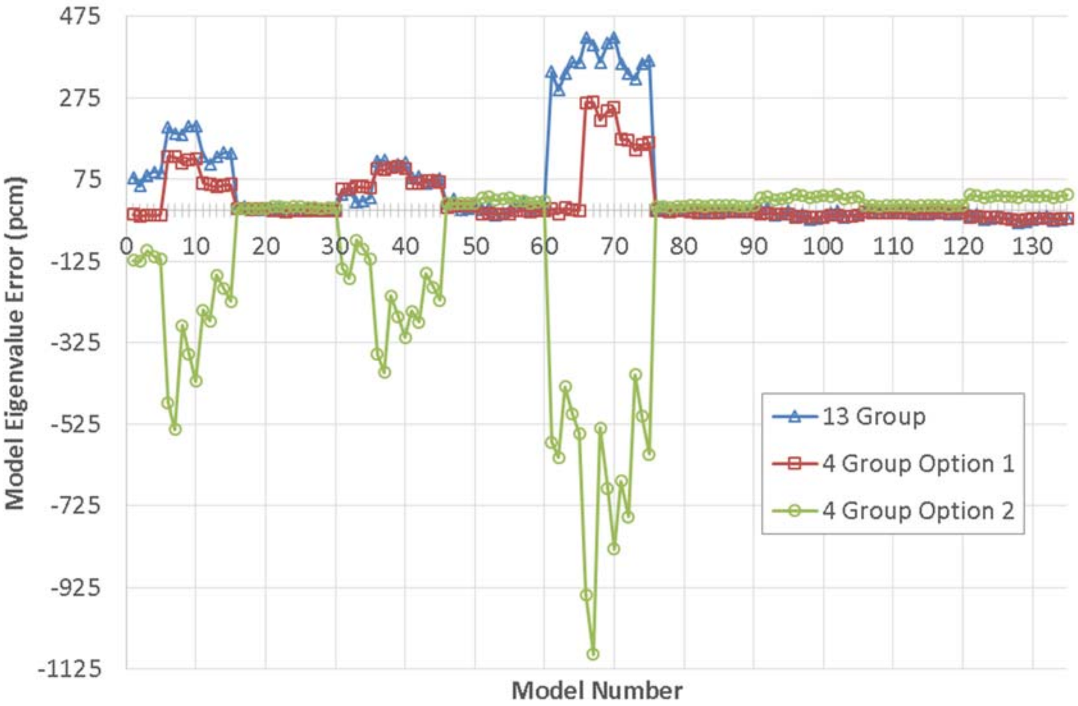

Figure 2-22 Eigenvalue Errors for Group Structures

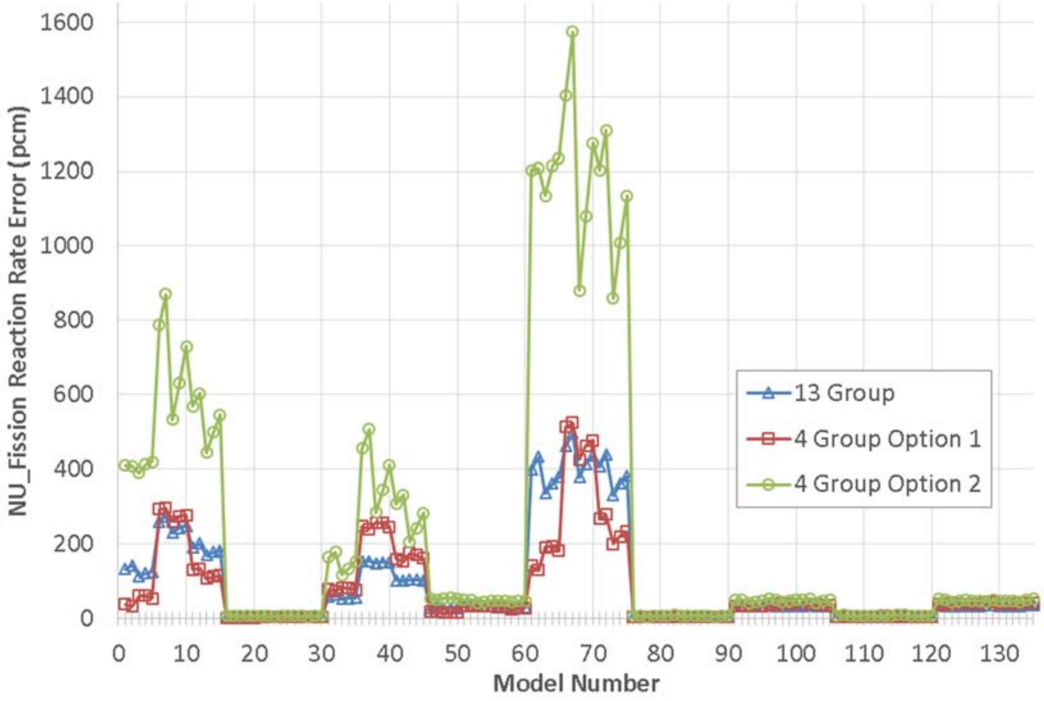

Figure 2-23 Maximum Zone $\nu \cdot \Sigma_{fiss}$ Reaction Rate Errors for Group Structures

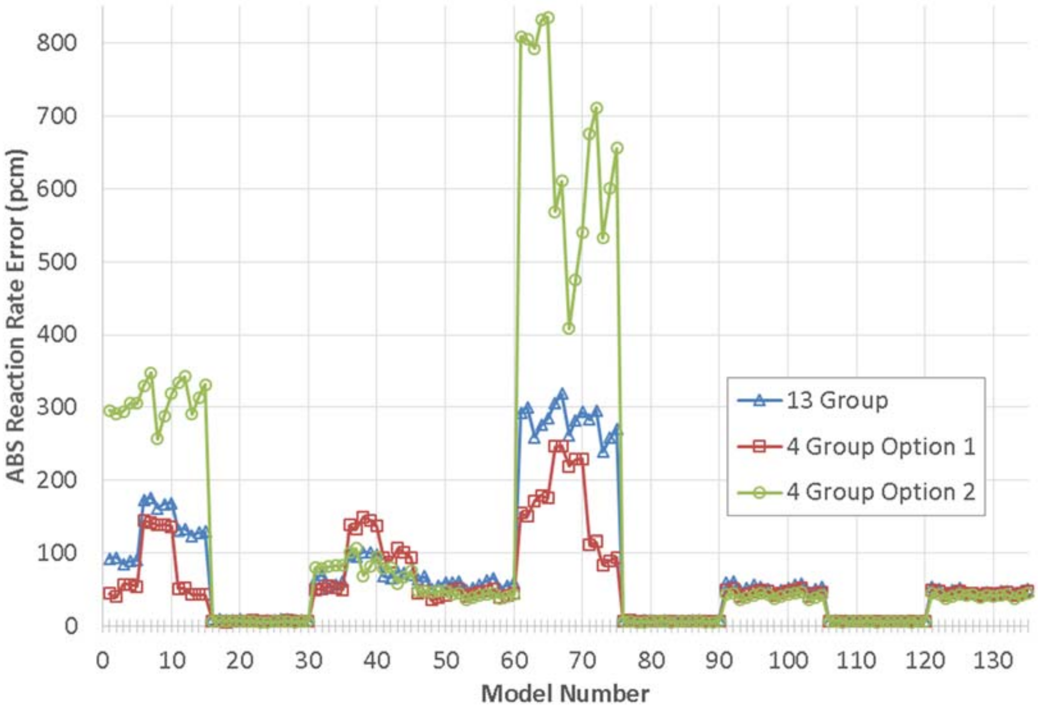

Figure 2-24 Maximum Zone Σ_{abs} Reaction Rate Errors for Group Structures

Table 2-7 Energy Group Error Plot Model Number List

Model	**Config***	**Burnup**	**Temp (K)**	**Model**	**Config***	**Burnup**	**Temp (K)**	**Model**	**Config***	**Burnup**	**Temp (K)**
1	AAAA	BOC	1200	46	**A**A**AA**	BOC	1200	91	**B**B**BB**	BOC	1200
2	AAAA	BOC	1500	47	**A**A**AA**	BOC	1500	92	**B**B**BB**	BOC	1500
3	AAAA	BOC	300	48	**A**A**AA**	BOC	300	93	**B**B**BB**	BOC	300
4	AAAA	BOC	600	49	**A**A**AA**	BOC	600	94	**B**B**BB**	BOC	600
5	AAAA	BOC	900	50	**A**A**AA**	BOC	900	95	**B**B**BB**	BOC	900
6	AAAA	EOC	1200	51	**A**A**AA**	EOC	1200	96	**B**B**BB**	EOC	1200
7	AAAA	EOC	1500	52	**A**A**AA**	EOC	1500	97	**B**B**BB**	EOC	1500
8	AAAA	EOC	300	53	**A**A**AA**	EOC	300	98	**B**B**BB**	EOC	300
9	AAAA	EOC	600	54	**A**A**AA**	EOC	600	99	**B**B**BB**	EOC	600
10	AAAA	EOC	900	55	**A**A**AA**	EOC	900	100	**B**B**BB**	EOC	900
11	AAAA	MOC	1200	56	**A**A**AA**	MOC	1200	101	**B**B**BB**	MOC	1200
12	AAAA	MOC	1500	57	**A**A**AA**	MOC	1500	102	**B**B**BB**	MOC	1500
13	AAAA	MOC	300	58	**A**A**AA**	MOC	300	103	**B**B**BB**	MOC	300
14	AAAA	MOC	600	59	**A**A**AA**	MOC	600	104	**B**B**BB**	MOC	600
15	AAAA	MOC	900	60	**A**A**AA**	MOC	900	105	**B**B**BB**	MOC	900
16	AAA**A**	BOC	1200	61	BACA	BOC	1200	106	CCC**C**	BOC	1200
17	AAA**A**	BOC	1500	62	BACA	BOC	1500	107	CCC**C**	BOC	1500
18	AAA**A**	BOC	300	63	BACA	BOC	300	108	CCC**C**	BOC	300
19	AAA**A**	BOC	600	64	BACA	BOC	600	109	CCC**C**	BOC	600
20	AAA**A**	BOC	900	65	BACA	BOC	900	110	CCC**C**	BOC	900
21	AAA**A**	EOC	1200	66	BACA	EOC	1200	111	CCC**C**	EOC	1200
22	AAA**A**	EOC	1500	67	BACA	EOC	1500	112	CCC**C**	EOC	1500
23	AAA**A**	EOC	300	68	BACA	EOC	300	113	CCC**C**	EOC	300
24	AAA**A**	EOC	600	69	BACA	EOC	600	114	CCC**C**	EOC	600
25	AAA**A**	EOC	900	70	BACA	EOC	900	115	CCC**C**	EOC	900
26	AAA**A**	MOC	1200	71	BACA	MOC	1200	116	CCC**C**	MOC	1200
27	AAA**A**	MOC	1500	72	BACA	MOC	1500	117	CCC**C**	MOC	1500
28	AAA**A**	MOC	300	73	BACA	MOC	300	118	CCC**C**	MOC	300
29	AAA**A**	MOC	600	74	BACA	MOC	600	119	CCC**C**	MOC	600
30	AAA**A**	MOC	900	75	BACA	MOC	900	120	CCC**C**	MOC	900
31	ABAC	BOC	1200	76	BBB**B**	BOC	1200	121	**CCCC**	BOC	1200
32	ABAC	BOC	1500	77	BBB**B**	BOC	1500	122	**CCCC**	BOC	1500
33	ABAC	BOC	300	78	BBB**B**	BOC	300	123	**CCCC**	BOC	300
34	ABAC	BOC	600	79	BBB**B**	BOC	600	124	**CCCC**	BOC	600
35	ABAC	BOC	900	80	BBB**B**	BOC	900	125	**CCCC**	BOC	900
36	ABAC	EOC	1200	81	BBB**B**	EOC	1200	126	**CCCC**	EOC	1200
37	ABAC	EOC	1500	82	BBB**B**	EOC	1500	127	**CCCC**	EOC	1500
38	ABAC	EOC	300	83	BBB**B**	EOC	300	128	**CCCC**	EOC	300
39	ABAC	EOC	600	84	BBB**B**	EOC	600	129	**CCCC**	EOC	600
40	ABAC	EOC	900	85	BBB**B**	EOC	900	130	**CCCC**	EOC	900
41	ABAC	MOC	1200	86	BBB**B**	MOC	1200	131	**CCCC**	MOC	1200
42	ABAC	MOC	1500	87	BBB**B**	MOC	1500	132	**CCCC**	MOC	1500
43	ABAC	MOC	300	88	BBB**B**	MOC	300	133	**CCCC**	MOC	300
44	ABAC	MOC	600	89	BBB**B**	MOC	600	134	**CCCC**	MOC	600
45	ABAC	MOC	900	90	BBB**B**	MOC	900	135	**CCCC**	MOC	900

* Red bolded letters denote zones with control blades inserted

2.4. Reflector Model

This section reviews the development of the radial and axial reflector models which were used to generate few group cross-section libraries for the core simulator. Included are discussions of the applied simplifications and 1-D benchmarking of the models both in terms of eigenvalue and power distribution.

Treatment of the reflector in a diffusion core simulator typically follows a similar manner as fuel assemblies, in that the reflector is represented with nodes with their own homogenized few-group cross-sections, diffusion parameters, and ADF values. These values must still be generated using a transport simulation, but unlike the fuel assemblies the reflector does not provide its own neutron source and so cannot be represented with a single reflector block with infinite boundary conditions. The typical approach to overcoming this hurdle is to implement a model in which the reflector is simulated along with fuel assemblies which provide the neutron source necessary to make the few-group homogenized values.

A full heterogeneous core simulation would be necessary to obtain an exact representation of the flux spectrum observed in the reflector in reality, but this would be far too computationally expensive and so some approximations must be made. One way to reduce this cost is to utilize a simplified core model that still provides a flux spectrum in the reflector region that is fairly consistent with that of the full core model. Various simplified models might be considered for this approximation, but for this study a semi 1-D full core model as illustrated in Figure 2-15 will be utilized. Examining at Figure 2-25, Figure 2-26, and Figure 2-27 reveal that nearer the fuel the 1-D reflector model does exhibit some difference in flux spectrum when compared to the 2-D model, however this difference diminishes as one moves deeper into the reflector. Though the difference is notable benchmarking will later show that it is not excessively impactful.

Though this simplified 1-D model can be used to generate homogenized cross-sections, diffusion parameters, and discontinuity factors in a manner consistent with the method described by K. Smith’s Generalized Equivalence Theory (GEM) (i.e. each surface having its own distinct discontinuity factor and node diffusion coefficients determined via flux weighted averaged transport cross-sections), the discontinuity factors and diffusion coefficients generated by this approach would not be sufficient in the diffusion 2-D and 3-D full core models. This is due to the fact that the full core diffusion model requires 6 discontinuity factors, one for each face of the hexagonal node. The semi 1-D model only generates 2 meaningful discontinuity factors; one for the single core facing surface and one for the exterior facing reflector surface.

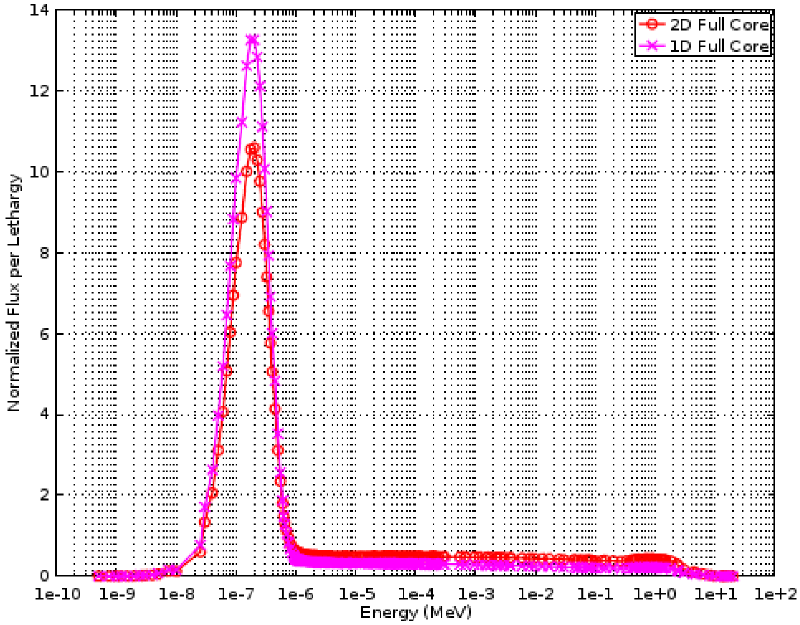

Figure 2-25 1-D and 2-D Full Core model Spectrum Differences in nearest-to-fuel 1/3 of Reflect

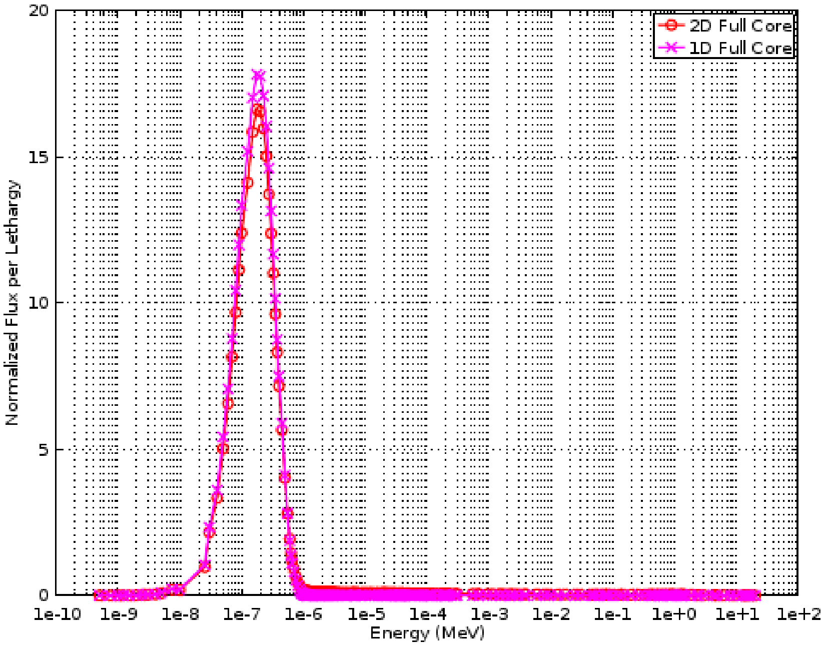

Figure 2-26 1-D and 2-D Full Core model Spectrum Differences in middle 1/3 of Reflect

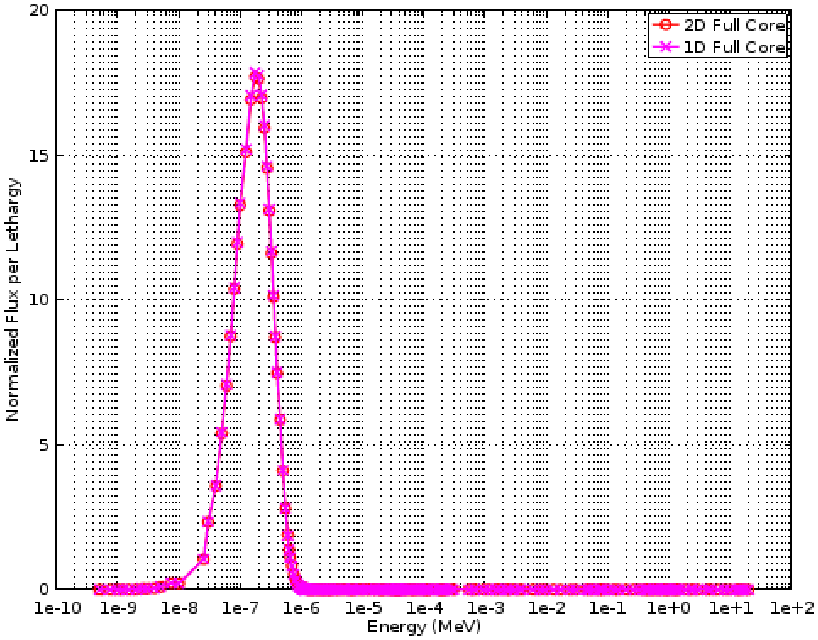

Figure 2-27 1-D and 2-D Full Core model Spectrum Differences in furthest-from-fuel 1/3 of Reflect

To surmount this challenge, a technique of cross-section adjustment to remove the need for explicit ADF treatment utilized in the modeling of VHTR was employed in this analysis [60]. In this approach, we assume that the individual fuel assemblies have nearly the same ADFs on surfaces in contact with other fuel assemblies and so the ADFs at the fuel and reflector interface can be assessed with a single effective fuel region and the reflector region as shown in Figure 2-28.

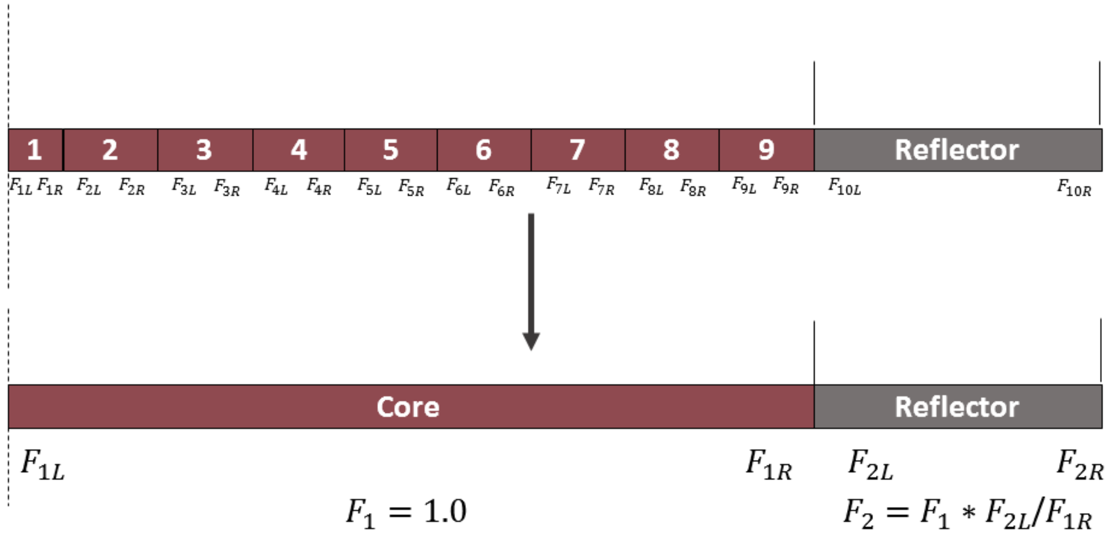

Figure 2-28 Illustration of Cross-section ADF Adjustment

After obtaining these ADFs, the goal then becomes adjusting the reflector cross-sections and diffusion coefficients such that all ADFs can be set to 1.0. We start by considering the homogeneous flux discontinuity relationship as shown in Equation (2-5) established by Equivalence Theory

$$F_{1R} \cdot \phi^f\left(x_{f+}\right) = F_{2L} \cdot \phi^r(x_{r-}) \tag{2-5}$$

If we assume the fuel ADF is 1.0, then we know via the above relationship that the reflector ADF must subsequently be altered to the ratio of the two ADFs

$$(1.0) \cdot \phi^f\left(x_{f+}\right) = \frac{F_{2L}}{F_{1R}} \cdot \phi^r(x_{r-}) \tag{2-6}$$

However, the goal is to ultimately have both fuel and reflector ADFs set to 1.0, and the can only be achieved if we scale our reflector flux by a factor of the ADF ratios.

$$(1.0) \cdot \phi^f\left(x_{f+}\right) = (1.0) \cdot \hat{\phi}^r(x_{r-}) \quad \text{where} \quad \hat{\phi}^r(x) = \frac{F_{2L}}{F_{1R}} \phi^r(x) \tag{2-7}$$

Now we should consider the 1-D nodal equation for the reflector provided below in Equation (2-8)

$$-\frac{d}{dx}D^r\frac{\partial}{\partial x}\phi^r(x)\bigg|_{x=x_{r+}}+\frac{d}{dx}D^r\frac{\partial}{\partial x}\phi^r(x)\bigg|_{x=x_{r-}}+A^r\bar{\phi}^r=Q^r\bar{\phi}^r \tag{2-8}$$

We can see that in order to obtain an equivalent relationship using the new “scaled” flux solution we must then multiply the diffusion coefficient and cross-sections by the inverse of the ADF ratio.

$$-\frac{d}{dx}\hat{D}^r\frac{\partial}{\partial x}\hat{\phi}^r(x)\bigg|_{x=x_{r+}}+\frac{d}{dx}\hat{D}^r\frac{\partial}{\partial x}\hat{\phi}^r(x)\bigg|_{x=x_{r-}}+\hat{A}^r\bar{\hat{\phi}}^r=\hat{Q}^r\bar{\hat{\phi}}^r \tag{2-9}$$

where,

$\hat{D}^r=\frac{F_{1R}}{F_{2L}}D^r$,

$\hat{A}^r=\frac{F_{1R}}{F_{2L}}A^r$, $\hat{\Sigma}_i^{\ r}=\frac{F_{1R}}{F_{2L}}\Sigma_i^{\ r}$,

$\hat{Q}^r=\frac{F_{1R}}{F_{2L}}Q^r$.

This can be carried even further if we were to assume a third region outside the reflector, such as a coolant region, were present that we would also like to represent with a 1.0 ADF.

$$F_{2R}\cdot\phi^r(x_{r+})=F_{3L}\cdot\phi^c(x_{c-}) \tag{2-10}$$

$$F_{2R}\cdot\hat{\phi}^r(x_{r+})=F_{3L}\cdot\frac{F_{2L}}{F_{1R}}\cdot\phi^c(x_{c-}) \tag{2-11}$$

$$(1.0)\cdot\phi^r(x_{r+})=(1.0)\cdot\hat{\phi}^c(x_{c-})\quad\text{where}\quad\hat{\phi}^c(x)=\frac{F_{3L}}{F_{2R}}\frac{F_{2L}}{F_{1R}}\phi^c(x) \tag{2-12}$$

$$-\frac{d}{dx}\hat{D}^c\frac{\partial}{\partial x}\hat{\phi}^c(x)\bigg|_{x=x_{c+}}+\frac{d}{dx}\hat{D}^c\frac{\partial}{\partial x}\hat{\phi}^c(x)\bigg|_{x=x_{c-}}+\hat{A}^c\bar{\hat{\phi}}^c=\hat{Q}^c\bar{\hat{\phi}}^c \tag{2-13}$$

where,

$\hat{D}^c=\frac{F_{2R}}{F_{3L}}\frac{F_{1R}}{F_{2L}}D^c$,

$\hat{A}^c=\frac{F_{2R}}{F_{3L}}\frac{F_{1R}}{F_{2L}}A^c$,

$\hat{Q}^c=\frac{F_{2R}}{F_{3L}}\frac{F_{1R}}{F_{2L}}Q^c$.

This process would continue for all subsequent regions until the boundary is reached where a final accumulated scaling factor can be applied to the outward facing discontinuity factor. However, in the event that the flux is very small at the boundary, then this final step may be ignored being that its contribution will be insignificant. Following this procedure, cross-sections and diffusion coefficients using a simple 1-D SERPENT 2 model can be adjusted such that the leakage behavior is maintained and ADFs can all be treated as 1.0 throughout the core. This procedure was applied not only for the radial reflector, but also for the axial reflector and coolant regions using a 3-D radially infinite assembly model with limited axial extents as illustrated in Figure 2-29.

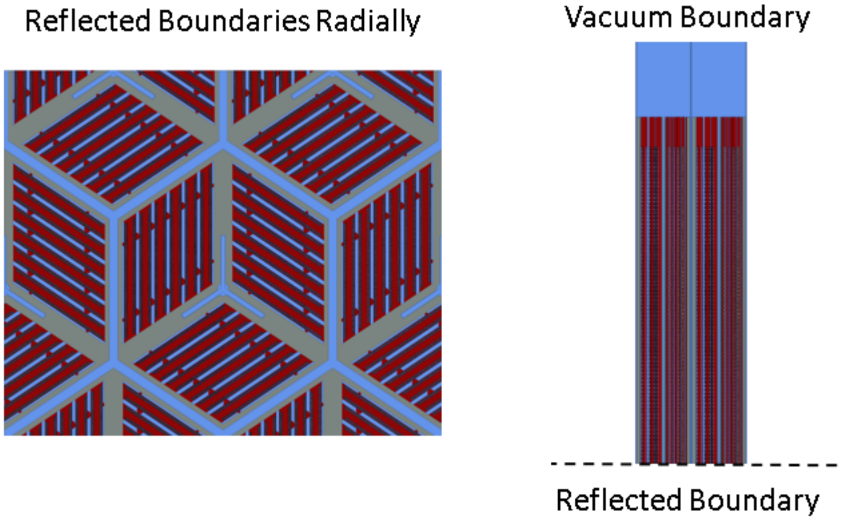

Figure 2-29 Axial Reflector Model Radial View (Left) and Axial View (Right)

Accuracy of this approach was assessed by using a 1-D finite difference code to replicate the SERPENT 2 models used for generating the reflector cross-sections. One item that was discovered early in this testing was that radially only the graphite portion of the "reflector" region need be model and that ignoring the vessel liner, inner wall, downcomer, and outer vessel provided identical neutronic behaviors. This can be observed in Figure 2-30 and was confirmed with a 2-D full core model. The likely explanations for this are the combination of large reflector size and the vessel liner being a boron shield. The nearly 2 assembly pitch thick reflector provides a considerable distance with which to reflect neutrons and those few that due reach the edge of the reflector are absorbed by the boron liner, effectively providing a vacuum boundary. This is important because it allows for further simplification of the problem geometry with essentially no impact on model accuracy.

The somewhat more significant observation made during these 1-D evaluations was that power distribution accuracy seemed significantly worse for Option 1 of the 4-group structures though the eigenvalue was nearly within the 2.8 pcm statistical uncertainty of the reference (Note: power distribution uncertainty was <0.00020). A likely explanation for this behavior is that the energy group optimization only considered the accuracy of using infinite single assembly models and not the accuracy of reflector energy group condensation. So whilst the 4-group Option 1 structure is fairly optimal for the infinite assembly approximation, it is not so for the reflector energy group condensation. This lead to the use of Option 2, detailed in Table 2-6, which was an older iteration on the infinite assembly energy group optimization that just so happened to be well optimized for the reflector, though it is generally of poorer accuracy for the infinite assembly approximation. It can be seen in Figure 2-30 that Option 2 performs considerably better than Option 1 with an eigenvalue agreement also within the statistical uncertainty.

For the axial reflector model it can be seen in Figure 2-31 that Option 2 again provided better power distribution agreement than Option 1, but not nearly to the same level of significance as was observed for the radial reflector (Note: power distribution uncertainty was <0.00039). . Eigenvalue agreements for both were again within the 2.8 pcm statistical uncertainty of the reference It is likely that the improved performance of Option 1 axially may be attributed to the fact that the axial reflector is not purely graphite, but actually a continuation of the fuel plates with only plate meat present. As such, there is channel coolant also present in the axial reflector region which produces a different flux spectrum than is observed in the radial reflector region. The important conclusion one can derive from these results though is that energy group optimization should consider reflector energy group condensation along with the accuracy of the infinite lattice approximation. Going forward, Option 2 was selected as the more desirable energy group structure for further analysis on the grounds of its better power distribution agreement. Alternative energy groups structures with greater energy resolution should be able to provide satisfactory reflector and assembly accuracy, but since NESTLE is currently limited to 4 groups, and so their pursuit was left for future work.

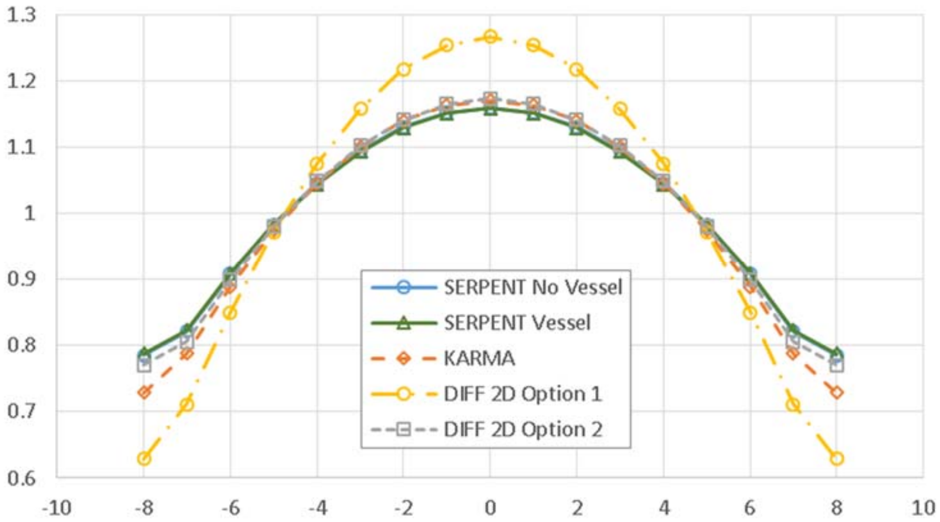

Figure 2-30 Radial 1-D model Power Distribution Comparisons

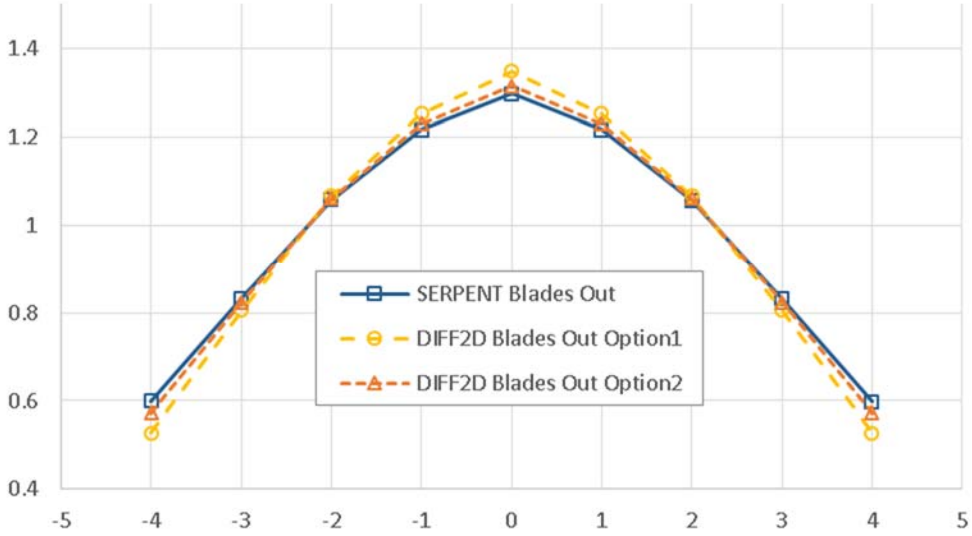

Figure 2-31 Axial 1-D Model Power Distribution Comparisons

A final item that was considered before moving forward with the AHTR two-step procedure development was the accuracy of the underlying fuel-to-fuel interface ADF equivalency assumption of this ADF adjustment technique. The validity of this assumption was assessed for the fuel interfaces of the 1-D KARMA model as well as against the various burnup and branch conditions of the 2-D single assembly model. A brief summary of the physical conditions of the branch cases can be found in Table 2-8. Examining Table 2-9 shows that the assumption largely holds for all assemblies with the possible exception of the outer most peripheral assembly which exhibited greater ADF values for groups 3 and 4. Although the outer most assembly ADFs were slightly elevated it was not believed that this was so large as to invalidate the above described ADF adjustment method.

In Table 2-10 one can observe that ADFs indeed change with respect to burnup in a somewhat significant manner. However, it should be noted that high burnup differences are necessary for the ADF discrepancy to become significant. Though cores are often loaded with assemblies of different burnup profiles depending on the applied batching strategy, it is believed to be unlikely that the burnup differences between the most fresh and most burned assemblies will be so large as to significantly challenge the ADF equivalence assumption of the ADF adjustment method. It also should at this point be observed that the 2-D assembly models exhibit two effective ADF values, each representing one of the plate facing arrangement of periodic rotational placement of plates. Though these values are fairly close, it is worth noting that the ADFs change depending on whether the plate flats or ends are facing the surface of the assembly.

Finally, Table 2-11 shows that assembly ADFs are largely unaffected by changes in coolant temperature / density and fuel temperature, but can be more significantly impacted by the insertion on a control blade. The difference in ADFs between controlled and uncontrolled assemblies is the largest that can be observed from the acquired results and therefore may require special consideration so to not invalidate the ADF equivalency assumption. This issue is specifically addressed in Section 2.5.

Table 2-8 Summary of Branch Conditions

	BASE	High Cool Temp	Low Cool Temp	High Cool Dens	Low Cool Dens	High Fuel Temp	Low Fuel Temp
Fuel Temp (K)	1700.33	1700.33	1700.33	1700.33	1700.33	2420.33	980.33
Cool Temp (K)	1247	1607	932	1247	1247	1247	1247
Cool Dens (g/cc)	1.9506	1.9506	1.9506	2.036	1.853	1.9506	1.9506

Table 2-9 ADFs of 1-D KARMA Model

	1	2		3		4		5		6		7		8		9		Refl
G	R	L	R	L	R	L	R	L	R	L	R	L	R	L	R	L	R	L
1	0.88	0.88	0.88	0.88	0.88	0.88	0.88	0.88	0.88	0.88	0.88	0.88	0.88	0.87	0.88	0.85	0.80	0.90
2	1.05	1.05	1.05	1.05	1.05	1.04	1.05	1.04	1.05	1.04	1.05	1.04	1.05	1.04	1.05	1.04	0.99	0.87
3	1.18	1.18	1.18	1.18	1.18	1.18	1.18	1.18	1.18	1.17	1.18	1.17	1.18	1.17	1.18	1.20	1.05	0.86
4	1.19	1.19	1.19	1.19	1.19	1.19	1.19	1.19	1.19	1.19	1.20	1.19	1.20	1.19	1.20	1.25	1.11	0.83

Table 2-10 Changes in ADFs of 2-D SERPENT 2 Model with Respect to Burnup

	0 GWd/MTHM		3.1 GWd/MTHM		85.3 GWd/MTHM		170.6 GWd/MTHM	
G	FACE 1	FACE 2	FACE 1	FACE 2	FACE 1	FACE 2	FACE 1	FACE 2
1	0.92	0.93	0.93	0.94	0.93	0.94	0.93	0.94
2	1.02	1.02	1.02	1.02	1.02	1.02	1.02	1.02
3	1.11	1.09	1.10	1.09	1.10	1.08	1.11	1.09
4	1.15	1.12	1.15	1.12	1.21	1.16	1.22	1.17

Table 2-11 Changes in ADFs of 2-D SERPENT 2 Model with Respect to Branches

	BASE		High Coolant Temp		Low Coolant Temp		High Coolant Dens		Low Coolant Dens		High Fuel Temp		Low Fuel Temp		Control Blade In	
G	FACE 1	FACE 2	FACE 1	FACE 2	FACE 1	FACE 2	FACE 1	FACE 2	FACE 1	FACE 2	FACE 1	FACE 2	FACE 1	FACE 2	FACE 1	FACE 2
1	0.92	0.93	0.92	0.94	0.93	0.94	0.92	0.93	0.93	0.93	0.93	0.94	0.92	0.94	0.94	0.95
2	1.02	1.02	1.02	1.02	1.03	1.02	1.02	1.02	1.02	1.02	1.02	1.02	1.02	1.02	1.05	1.05
3	1.11	1.09	1.10	1.09	1.10	1.08	1.10	1.08	1.10	1.08	1.11	1.09	1.10	1.08	1.16	1.15
4	1.15	1.12	1.14	1.12	1.15	1.12	1.15	1.12	1.14	1.11	1.15	1.12	1.15	1.12	1.24	1.21

2.5. Control Blade Correction

This section covers the development of a correction method for the infinite assembly assumption for a model with a control blade inserted. Discussed is a brief derivation of the correction method and how it is applied for AHTR.

As mentioned previously, the single infinite assembly model is not a correct treatment for cases in which the control blades are inserted. To recap, this is due to the fact that the control blades will be serving as primary reactivity control, implying that controlled assemblies will likely be surrounded uncontrolled assemblies which directly counters the infinite assembly assumption of the single cell model. As such, the infinite assembly approximation alone will not accurately represent the flux conditions experienced by a controlled assembly, and so some correction must be applied.

To perform this correction we can follow in a similar notion as was discussed for the reflector in Section 2.4. First, we must consider what might be assumed a more “realistic” representation of a control blade insertion model. For at power control, it is most likely that some checker-boarded insertion scheme will be employed to avoid excessive power peaking. Therefore, we can construct a representative super-cell both for assemblies with control blades inserted Figure 2-32 and for the neighboring uncontrolled assemblies Figure 2-33. Simulations are conducted for both cases being that the discontinuity factor ratio used for the cross section correction will depend on the ADFs of both the controlled and neighboring uncontrolled assemblies. From these models we can calculate ADFs on all 6 faces of the controlled and uncontrolled assembly.

It should be noted that these ADFs will not be equal due to rotational arrangement of the plates, however we are only concerned with the node’s net leakage behavior. Therefore, we can average the surface ADFs of each set, effectively assuming all surfaces experience the same average current and fluxes. Using the previously mentioned approach for the reflector, we can similarly obtain the following:

$$F_O \cdot \phi^O(x_{O+}) = F_I \cdot \phi^I(x_{I-}) \tag{2-14}$$

$$(1.0) \cdot \phi^O(x_{O+}) = \frac{F_I}{F_O} \cdot \phi^I(x_{I-}) \tag{2-15}$$

$$(1.0) \cdot \phi^O(x_{O+}) = (1.0) \cdot \hat{\phi}^I(x_{I-}) \quad \text{where} \quad \hat{\phi}^I(x) = \frac{F_I}{F_O} \phi^I(x) \tag{2-16}$$

$$-\frac{d}{dx}\widehat{D}^I\frac{\partial}{\partial x}\hat{\phi}^I(x)\bigg|_{x=x_{I+}}+\frac{d}{dx}\widehat{D}^I\frac{\partial}{\partial x}\hat{\phi}^I(x)\bigg|_{x=x_{I-}}+\hat{A}^I\bar{\bar{\phi}}^I=\hat{Q}^I\bar{\bar{\phi}}^I \tag{2-17}$$

where,

$\widehat{D}^I=\frac{F_O}{F_I}D^I$,

$\hat{A}^I=\frac{F_O}{F_I}A^I$,

$\hat{Q}^I=\frac{F_O}{F_I}Q^I$.

Using this approach we can then generate leakage adjustments to the infinite assembly control blade cross-sections to account for the control blade heterogeneity of true operation.

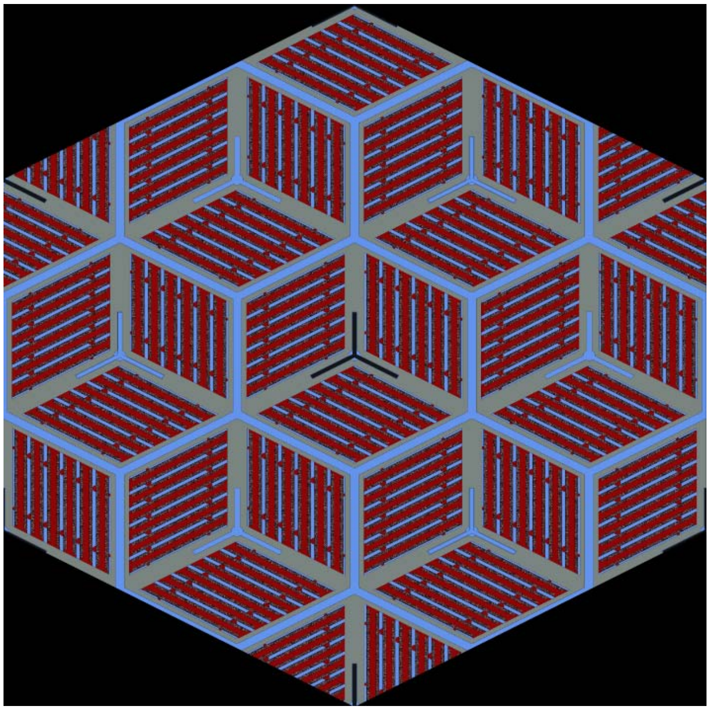

Figure 2-32 Super Cell Model for Control Blade Inserted in Primary Assembly

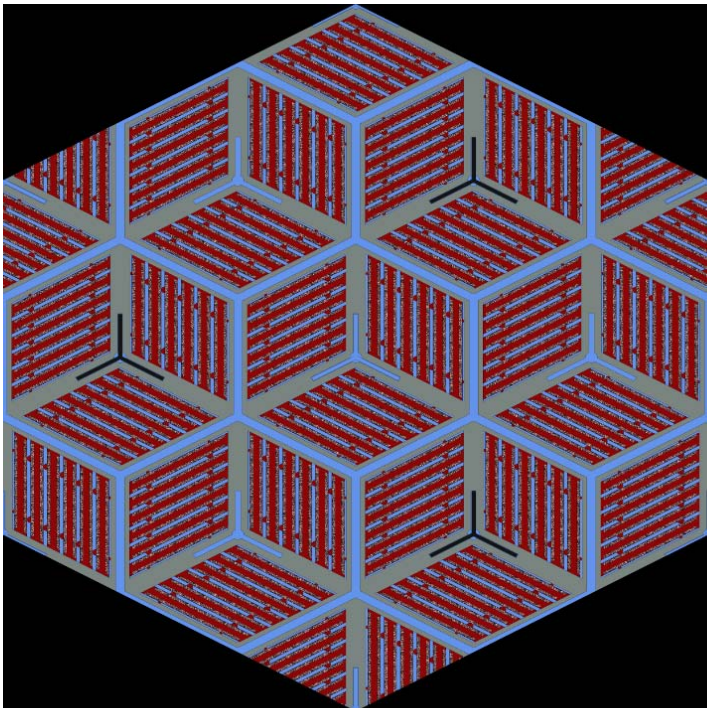

Figure 2-33 Super Cell Model for Control Blade Inserted in Neighboring Assemblies

2.6. Cross-section Functionalization

The previous sections of this chapter have thus far discussed the adaptation of the lattice physics simulations so as to produce useable cross section data for a core simulator. Though this cross section data should be generic and usable by any core simulator able to support the AHTR's particular geometry and coolant, formatting of the cross-section libraries will almost certainly be needed to put the data into a form usable by the selected core simulator.

Such is the case with NESTLE, wherein cross-section libraries are not simply read and interpolated from tabular data, but rather by polynomial functionalization as shown in Equation (2-18). This polynomial represents a Taylor expansion of the effective node cross-section with expansion coefficients that can be determined via polynomial fitting of the base and branch case data. For NESTLE, these fits must be performed for each set of perturbations (i.e. changes in fuel temp, coolant density, coolant temp, etc.) and burnup conditions independently of one another with no consideration of cross-terms nor history effects. Though this can ultimately lead to some accumulation of errors in the core simulator results when performing cycle analysis, we must remember that the goal of this research is simply to demonstrate the viability and means of performing a two-step procedure for the AHTR. Further application of this approach for cycle analysis may necessitate the use of an alternative core simulator if higher degrees of accuracy are desired.

$$\begin{aligned}\Sigma_{xg} = a_{1_{xg}} + \sum_{n=1}^{2} a_{(n+1)_{xg}} (\Delta\rho_c)^n + a_{4_{xg}} \Delta T_c + a_{5_{xg}} \Delta\sqrt{T_{F_{eff}}} \\ + \sum_{n=1}^{3} a_{(n+5)_{xg}} \left(\Delta N_{sp}\right)^n\end{aligned} \tag{2-18}$$

where,

$a_{j_{xg}}$ = expansion coefficient,

ΔT_c = change in coolant temperature,

$\Delta\sqrt{T_{F_{eff}}}$ = change in square root of effective fuel temperature,

$\Delta\rho_c$ = change in coolant density,

ΔN_{sp} = change in soluble poison concentration.

Coupling programs and scripts were written to extract all relevant data from the SERPENT 2 outputs, including outputs from infinite assembly models, control blade leakage correction models, and reflector models. These programs then calculated and applied any leakage correction factors where appropriate to the cross-sections, performed the polynomial fittings to determine expansion coefficients, and wrote the final data sets into a NESTLE readable format. An illustration of the code flow diagrams are provided in Figure 2-34 and Figure 2-35.

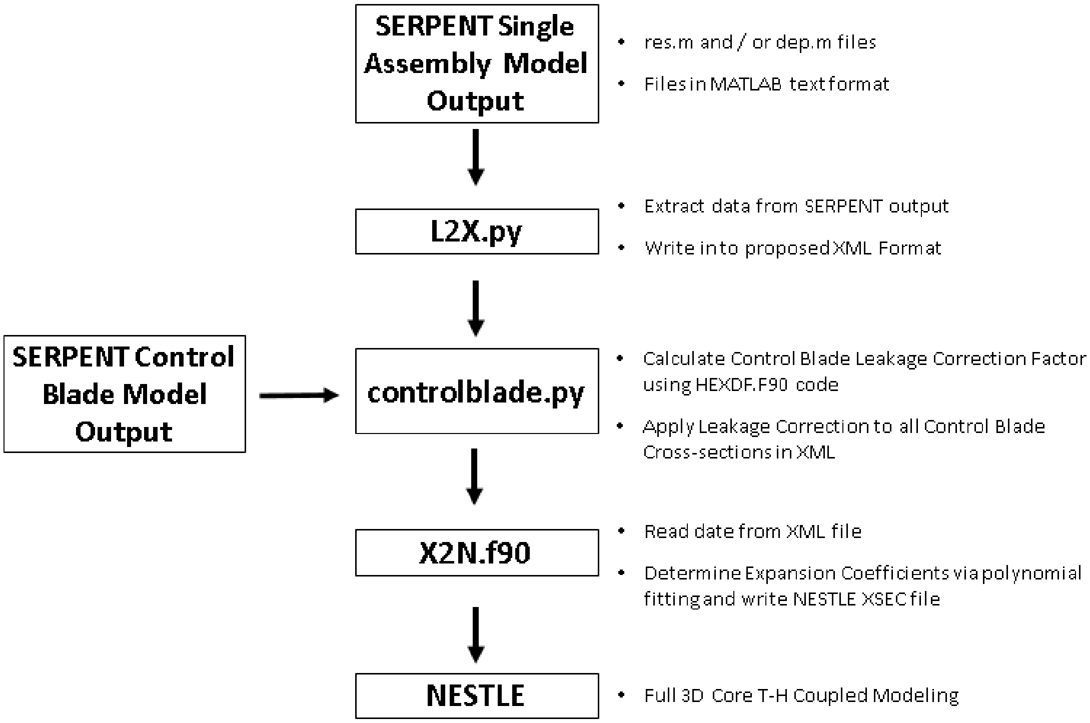

Figure 2-34 Diagram of Single Assembly Cross-section Functionalization Programs

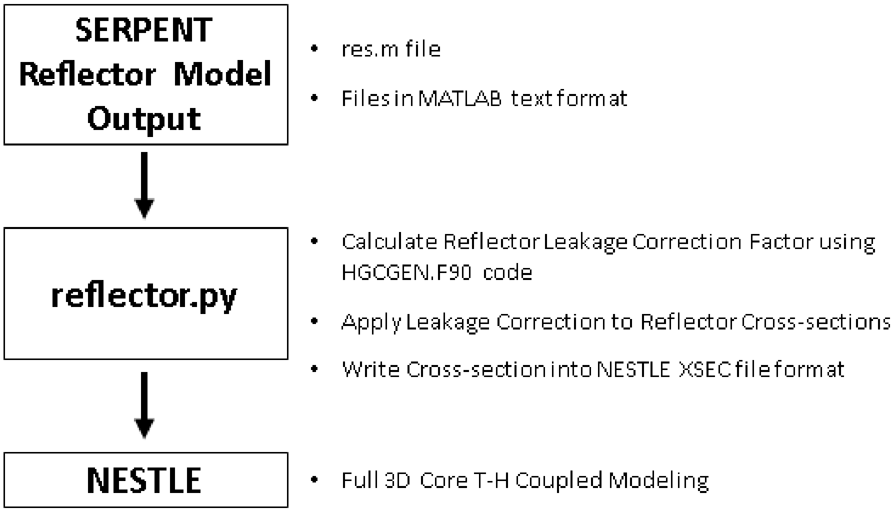

Figure 2-35 Diagram of Reflector Cross-section Functionalization Programs

It should be noted that some bugs were encountered when using the SERPENT 2 calculated values for Xe, I, Pm, and Sm microscopic cross-sections and yields. It was found that these values were not consistent with other SERPENT 2 results and so they were determined by alternative means. The microscopic cross-sections were determined by dividing the macroscopic cross-sections by the isotopic number densities provided either by the "res.m" output file for models run using the SERPENT 2 equilibrium settings for Xe and Sm or the "dep.m" when not using the equilibrium feature. The yields were determined via back calculation from the equilibrium Bateman equations, which at least provided a first order approximation.

The fitting routines, used strictly for the infinite assembly cross-sections, were tested via comparison to the SERPENT 2 single assembly results for the base case and all branching cases. It can be observed in Figure 2-36 and Figure 2-37 that the fitting routines appear to match the SERPENT 2 results well within the 83 pcm solution statistical uncertainty.

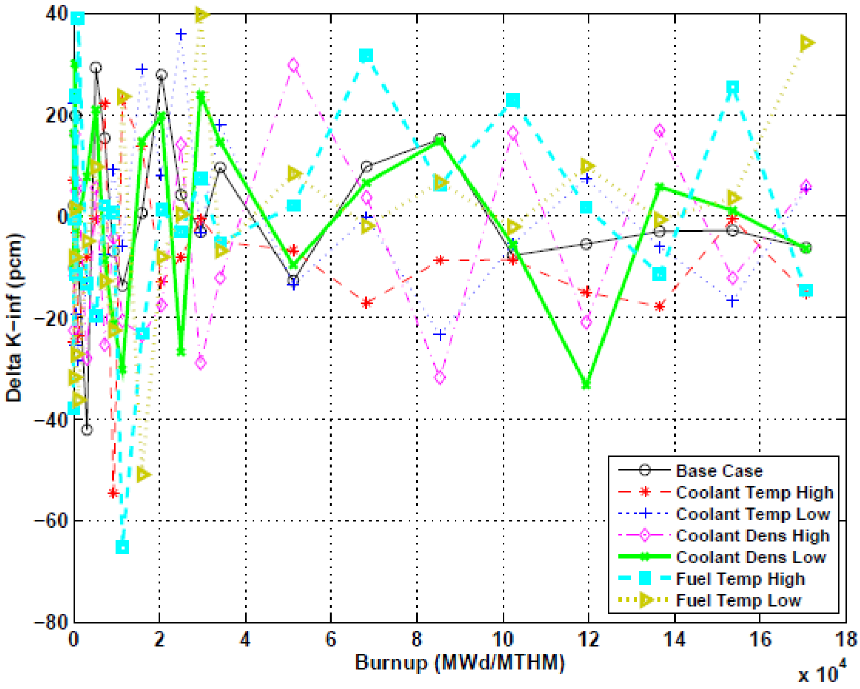

Figure 2-36 Error of NESTLE Single Assembly Model with Control Blades Out Compared to SERPENT 2

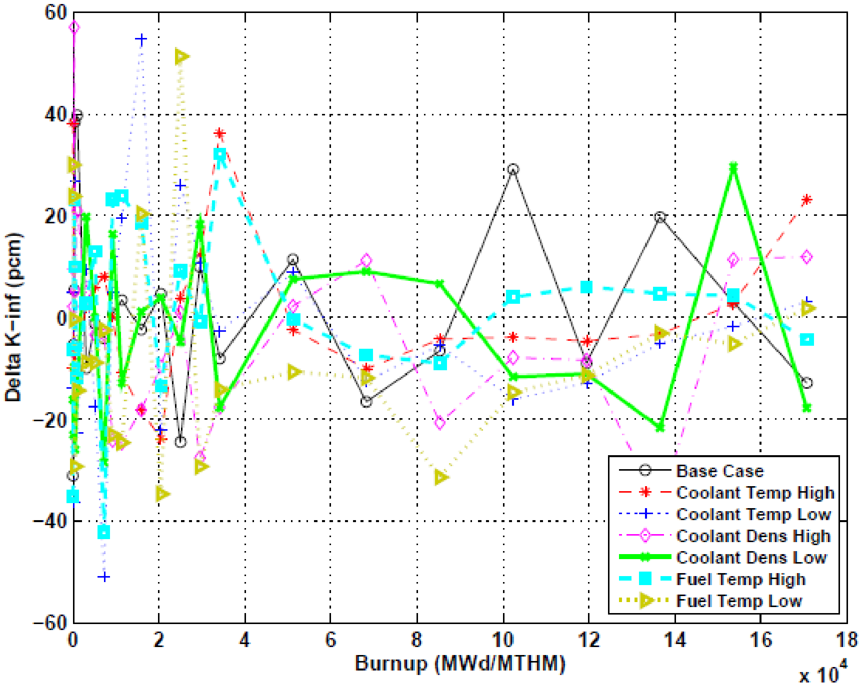

Figure 2-37 Error of NESTLE Single Assembly Model with Control Blades IN Compared to SERPENT 2

2.7. Thermal Hydraulic and Fuel Temperature Polynomials

This section briefly discusses the defining of closure polynomials for the thermal hydraulic and fuel temperature polynomials needed within NESTLE. As mentioned previously in Section 1.6.2, NESTLE utilizes polynomials with user provided coefficients to act as closure relationships for NESTLE's internal thermal hydraulic and fuel temperature models. These polynomial coefficients must be determined by some external means, whether by modeling or experimentation, and for this research they were determined by referring to previous research studies on FLiBe properties and fuel plate temperature simulations.

For the coolant related polynomials, a combination of the studies on the implementation for FLiBe modeling in RELAP and the INL database on liquid salt properties were utilized to determine the coefficients [62, 63]. Equation (2-19) and Equation (2-20) show the determined closure relationships pertaining to the coolant that were utilized in NESTLE.

$$\rho = 142.8588 - 0.029181U \tag{2-19}$$

where,

$\rho =$ Density (lbm/ft^3),

$U =$ Internal Energy (BTU/lbm).

$$T = 885.44 + 1.73U \tag{2-20}$$

where,

$T =$ Temperature (°F),

$U =$ Internal Energy (BTU/lbm).

For the fuel temperature related polynomials, the studies by P. Avigni on thermal hydraulic modeling of AHTR were utilized [64]. Equation (2-21), Equation (2-22), Equation (2-23), and Equation (2-24) show the determined closure relationships pertaining to the fuel that were utilized in NESTLE.

$$T = 1251.4 - 0.0012L + 9 \times 10^{-9}L^2 \tag{2-21}$$

where,

$T =$ Average Fuel Temperature (°F),

$L =$ Linear Power Density (kW/ft).

$$h = 3.3604 - 0.0034T + 1 \times 10^{-6}T^2 \tag{2-22}$$

where,

$h =$ Effective Heat Transfer Coefficient (kw/ft^2-°F),

$T =$ Average Fuel Temperature (°F).

$$T = 1283.5 - 0.0014L + 7 \times 10^{-9}L^2 \qquad (2\text{-}23)$$

where,

T = Fuel Surface Temperature (°F),

L = Linear Power Density (kW/ft).

$$C_p = 0.073 + 0.0003T - 7 \times 10^{-8}T^2 \qquad (2\text{-}24)$$

where,

C_p = Fuel Specific Heat,

T = Average Fuel Temperature (°F).

2.8. Discussion of Plate Power Reconstruction and Thermal Limits

This section discusses the issue of plate power reconstruction. Although the means for defining and calculating it are present in SERPENT 2 and NESTLE, this step was not pursued on account of time limitations and of having a lower priority and importance in contrast to other aspects of this work.

As mentioned previously, pin power reconstruction is an often utilized technique in LWR analysis to assess performance margins concerning coolant limits such as departure from nucleate boiling and rod dry-out, as well as fuel performance limits such as centerline fuel melt for individual rods and axial locations. Because of its common use in the traditional LWR two-step procedure, it was also considered for the AHTR modeling herein pursued and referred to as plate power reconstruction.

The equivalent operating limits of importance for AHTR are the boiling temperature of the coolant at 1400°C and TRISO particle failure temperature at 1600°C, though administrative limits appear to be typically set around 1000°C and 1250°C for coolant and fuel respectively [2]. Review of the literature, namely the thermal hydraulic study by P. Avigni [64] and initial ORNL study [1,2], revealed that even over a wide variety of design variations, consideration of irradiation induced degradation of conductivity, and Loss of Forced Cooling the administrative limits are in most cases not exceeded and the ultimate limits never surpassed.

According to the aforementioned sources, typical operating conditions for the base design place the outlet coolant temperatures around 700°C with a maximum fuel temperature approximation between 951°C and 1,004°C. Variations in plate design including adjustment of packing fraction, coolant gap thickness, stripe region thickness, and sleeve thickness can each lead to an increase in temperature ranging from 50°C up to 150°C depending on the type of alteration and to what degree. Degradation of graphite conductivity is estimated to produce an increase in maximum fuel temperature by about 80°C, though it should be noted irradiation is also correlated with fuel burnup (i.e. lower fuel power and ultimately lower temperature). Considering the worst case design alterations combined with the irradiation induced degradation of conductivity, we can crudely estimate a conservative introduction of 370°C due to irradiation and poor fuel design. It should be noted that this is highly conservative in that the stripe thickness and coolant gap thickness both account part of the increased fuel temperature due to reduction in meat size, which means if both are applied we need only take credit for the meat displacement effect of one, whereas the 370°C approximation allows for contributions from both. Also, design alterations that result in increased fuel temperature do not necessarily represent design alterations that would be desirable with regards to fuel efficiency. Even so, this conservative approximation only places the maximum fuel temperature at around 1370°C, which does exceed the administrative goal but is still well below the ultimate failure temperature. With regards to coolant temperature, even a substantial increase in fuel stripe thickness and reduction in coolant gap thickness only raises at power coolant temperature to 820°C [1,64].

Furthermore, current design reactivity coefficients exhibit a possibly small positive coolant void coefficient that is largely dwarfed by the large negative fuel and graphite temperature coefficient. Meaning, a large majority of feasible accident scenarios will lead to decreasing fuel and coolant temperatures, even in the event of Loss of Forced Cooling due to the proposed passive safety systems. Also, large assembly power peaking and transversal plate power peaking appears to contribute less than 1°C per 1% power tilt (Note: longitudinal plate power peaking effects were not assessed by these studies) [1,64].

All of this has been stated in order to illustrate that in all except possibly the most extreme of poor fuel and core design scenarios plate power reconstruction is not crucially essential for safety performance assessment. This can be done in practice, where tallies are used in SERPENT 2 to assess form factors with any level of spatial fidelity at the various burnups and operating perturbations as illustrated in Figure 2-38 and Figure 2-39. However, the large safety margins will likely alleviate the need for plate power reconstruction, and due to the combination of this fact and the limited time constraints of this project, full implementation of plate power reconstruction was not pursued and left for future work.

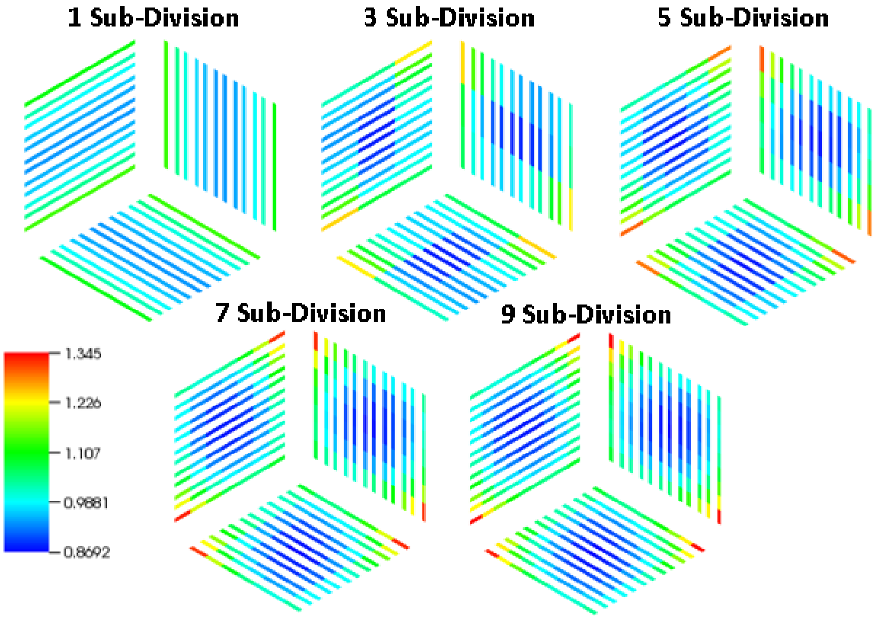

Figure 2-38 Power Densities at 0 GWd/MTHM of each Sub-Division Model Normalized to Assembly Average

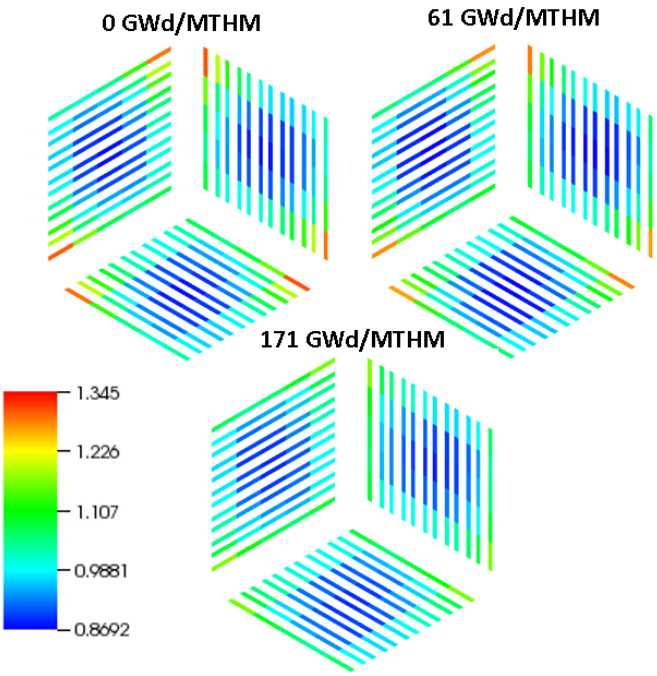

Figure 2-39 Power Densities at Various Burnups Normalized to 0 GWd/MTHM Average

3. Benchmarking of AHTR two-step Procedure

This section discusses the benchmarking of the AHTR two-step procedure using the NESTLE core simulator and comparing to reference SERPENT 2 high fidelity Monte Carlo models. Additionally the final T-H coupled core simulation is demonstrated so as to provide a proof of principle and to accentuate the speed and utility of the two-step procedure.

3.1. 2-D Benchmarking of two-step Procedure

Benchmarking of the two-step procedure began with testing of 2-D full core models. One of the first and somewhat obvious issues to address is the fact that the true core model will have a rounded reflector whereas the NESTLE model will consist of hexagonal reflector nodes producing a somewhat jagged reflector as shown in Figure 3-1. Though this two-step procedure will not address the modeling inaccuracy it is still worth assessing significance of it. Looking at Figure 3-2 it can be seen that an approximately 2% power tilt is induced along the “flats” of the core periphery, specifically where the reflector is thickest, at 12:00, 1:30, 4:30, 6:00, 7:30, and 10:30, in analogy to a clock. This is easily explained by looking again at Figure 3-1 and noticing that the rounded reflector thickness along the flats is thicker than two assembly pitches which is modeled by the jagged representation, thus producing greater reflection and ultimately higher power. Again, this source of error was not addressed in this two-step procedure, and only acknowledged for the sake of completeness. But it should be noted that it could likely be addressed by either tuning the core simulator boundary conditions or artificially adding extra reflector nodes to the points most effected by the error. All comparisons between NESTLE and SERPENT 2 were made using the jagged representation so that the two-step procedure can be assessed in the absence of this known modeling error.

An initial comparison between SERPENT 2 and NESTLE models with all control blades out was made using the 4-group Option 1 energy group structure. Looking at Figure 3-3 it can be seen that like the previous radial 1-D model, the Option 1 NESTLE model shows very high central peaking with a 20% power tilt, an 11% RMS error, and an eigenvalue agreement of about 200 ± 1.4 pcm. However, a substantial improvement was observed again when use the Option 2 energy group structure with the tilt reducing to within 6% with an RMS error less than 3.1% and the eigenvalue agreement to within 115 ± 1.4 pcm. Nevertheless, this tilt still appears fairly large and so the model was verified against an alternative core simulator, PARCS, to provide independent verification [65]. It can be seen in Figure 3-2 that the tilt is even further reduced to within 4% and RMS error less than 2% which is fairly close to what might be expected from using only 4 energy groups. PARCS eigenvalue agreement is with 141 ± 1.4 pcm, which though slightly worse than NESTLE might be attributed to the infinite assembly error from using the Option 2 4 group structure. The differences between the NESTLE and PARCs results are likely explained by their differences in modeling hexagonal nodes. In NESTLE, conformal mapping is used to transform the hexagonal node into a rectangular node, whose flux shape is then determined using the quartic NEM method used in NESTLE for Cartesian geometries. However in PARCS, hexagonal nodes are treated with the hexagonal nodal method known as Triangle-based Polynomial Expansion Nodal (TPEN) method wherein the radial flux shape is determined by splitting the hexagon into six triangles and employing a 3rd order polynomial expansion within each triangle, and the axial flux shape is determined using the quartic NEM method. Although the results of both approaches should be comparable being as both are proven methods, it is not unreasonable to expect some differences between the two, and this can be observed in all NESTLE / PARCS results.

Despite the reasonably good agreement between NESTLE / PARCS and SERPENT 2 for a four-group structure, the power tilt was investigated further due to its seemingly 1/3 azimuthal periodicity. Upon closer examination of the SERPENT 2 assembly wise power distributions, it was discovered that the SERPENT 2 edge assembly power results in fact exhibited an inherent 1/3 azimuthally periodic asymmetry between the north west, north east, and south (NW/NE/S) faces of the core relative to their southeast, southwest, and north counterparts (SE/SW/N), as shown in Figure 3-4, where the color scale has been adjusted to visibly highlight color differences in the low power peripheral regions. In other words, the high-fidelity stochastic transport results were not 1/6 symmetric as the NESTLE and PARCS results, showing a 2% to 4% higher power in the NW/NE/S edges of the core relative to the SE/SW/N faces.

Examination of the stripe subdivision power distributions, shown Figure 3-5, helped to identify the cause of these non-uniform peripheral power peaks. It can be seen that for those assemblies on the north edge of the core that two tri-sections separated by a perpendicularly oriented intra-tri-section moderator gap face the reflector, whereas on the north west peripheral assemblies only a sinlge tri-section faces the reflector with no intra-tri-section moderator gap facing that direction. The single tri-section, corresponding to the NW/NE/S edges, whether by improved resonance escape probability, superior moderation, and/or by having a larger fraction of fuel directly facing the moderator (no intra-tri-section gaps perpendicularly facing the reflector), is therefore more reactive than its SW/SW/N equivalents, and thus yields higher assembly power in those regions in a 1/3 periodic manner.

Consequently, the discrepancies encountered between NESTLE (or PARCS) and SERPENT 2 are not solely indicative of poor energy group structuring, but also include an underlying directional dependency that the current Two-Step procedure was unable to replicate, because the 1-D reflector model used to perform the ADF leakage correction of the reflector cross-sections essentially assumed full radial symmetry. However, as evidenced in the 2-D SERPENT 2 model, such is not a good assumption for all the radial faces of the core because the AHTR fuel assemblies can have two different orientations out on the edge of the core. Thus, this simply illustrates an inaccuracy introduced by the current approach to establish reflector cross sections, which introduces a notable power tilt but it is not excessively large so as to invalidate the Two-Step approach as an analysis tool. In fact, to fix this problem, one might develop two sets of orientation-dependent radial edge cross sections by using 1-D or 2-D transport models to properly characterize the reflector and fuel interface within the two distinct assembly orientations, and by explicitly treating the corresponding fuel/reflector ADFs within the core simulator rather than by including them into the cross-sections as a correction factor.

After performing the assessment with all control blades out, the case with control blades inserted was then investigated. For this model control blades were fully inserted in a checkerboard configuration to more closely represent a controlled core configuration at power, rather than an all blades in model which would represent a shutdown configuration. The initial NESTLE model utilized the ADF corrected control blade cross-sections along with the radial reflector cross-sections corresponding to the all blades out configuration. However, the use of control blade withdrawn radial reflector lead to a significant 10% radial power tilt in NESTLE with an RMS error within 5.4% as shown in Figure 3-6. This though was addressed by developing an alternative 1-D reflector model for control blade inserted cases wherein rods are inserted in an alternating manner as illustrated by Figure 3-7, where the inserted control blades are noted by the black stripes and those without blades are blue. Additionally, a control blade inserted case was simulated for the axial reflector, however it should be noted that unlike the fuel control blade inserted model, no radial ADF adjustment was made. This is because a means to accurately calculate these radial ADFs for the axial reflector and coolant regions was unavailable, and so applying the fuel region ADF adjustment may not have been entirely accurate. Therefore, a radial ADF adjustment was not applied to the axial reflector and coolant regionsand results assessed by comparison to a 3-D benchmark. Upon applying this new control blade case reflector cross-section, the NESTLE power errors were reduced to within 6% with an RMS error within 2.4% and k-effective agreement versus SERPENT 2 was within 130 ± 1.5 pcm. Likewise, the power and k-effective results for PARCS were calculated to within 5.3% maximum error, RMS error within 2.8%, and 140 ± 1.5 as seen in Figure 3-6. The power peaks that still persist are believed to be a result of the inaccurate symmetric reflector assumption. The presence of control blades as well as the blade-modified reflector model have shifted the power errors away from the previous troubled assemblies to new assemblies, but the underlying cause is still believed to be the same.

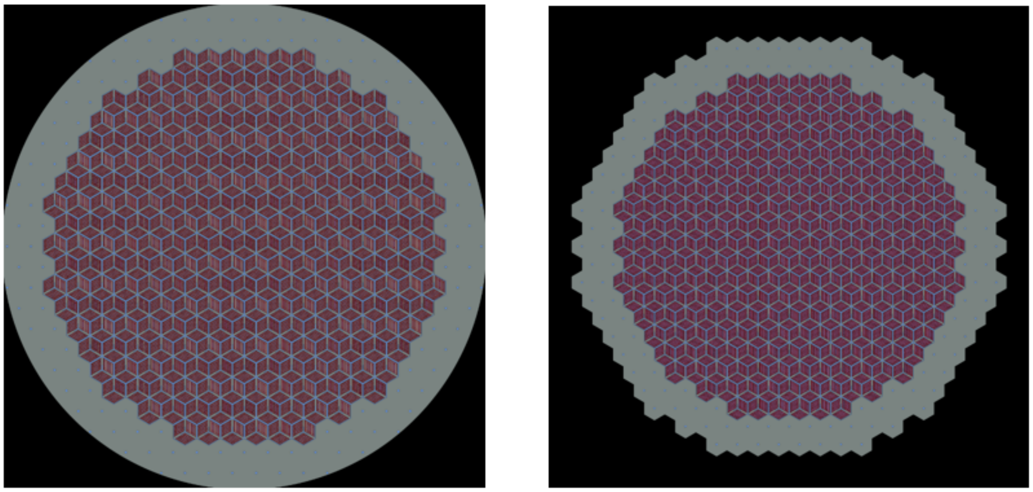

Figure 3-1 Illustration of Rounded Reflector (Left) and Jagged Reflector (Right)

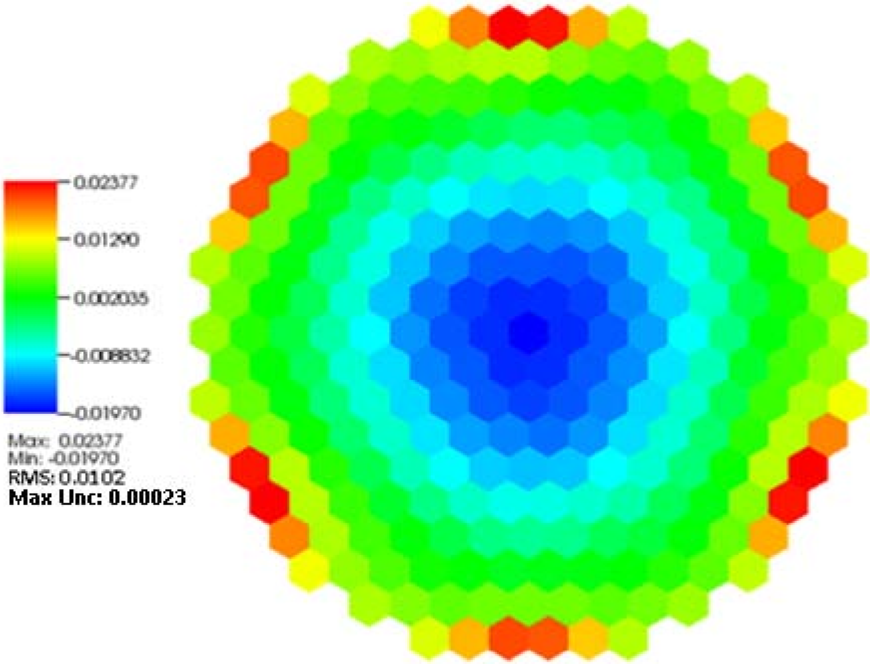

Figure 3-2 Relative Power Differences Rounded Reflector minus Jagged Reflector

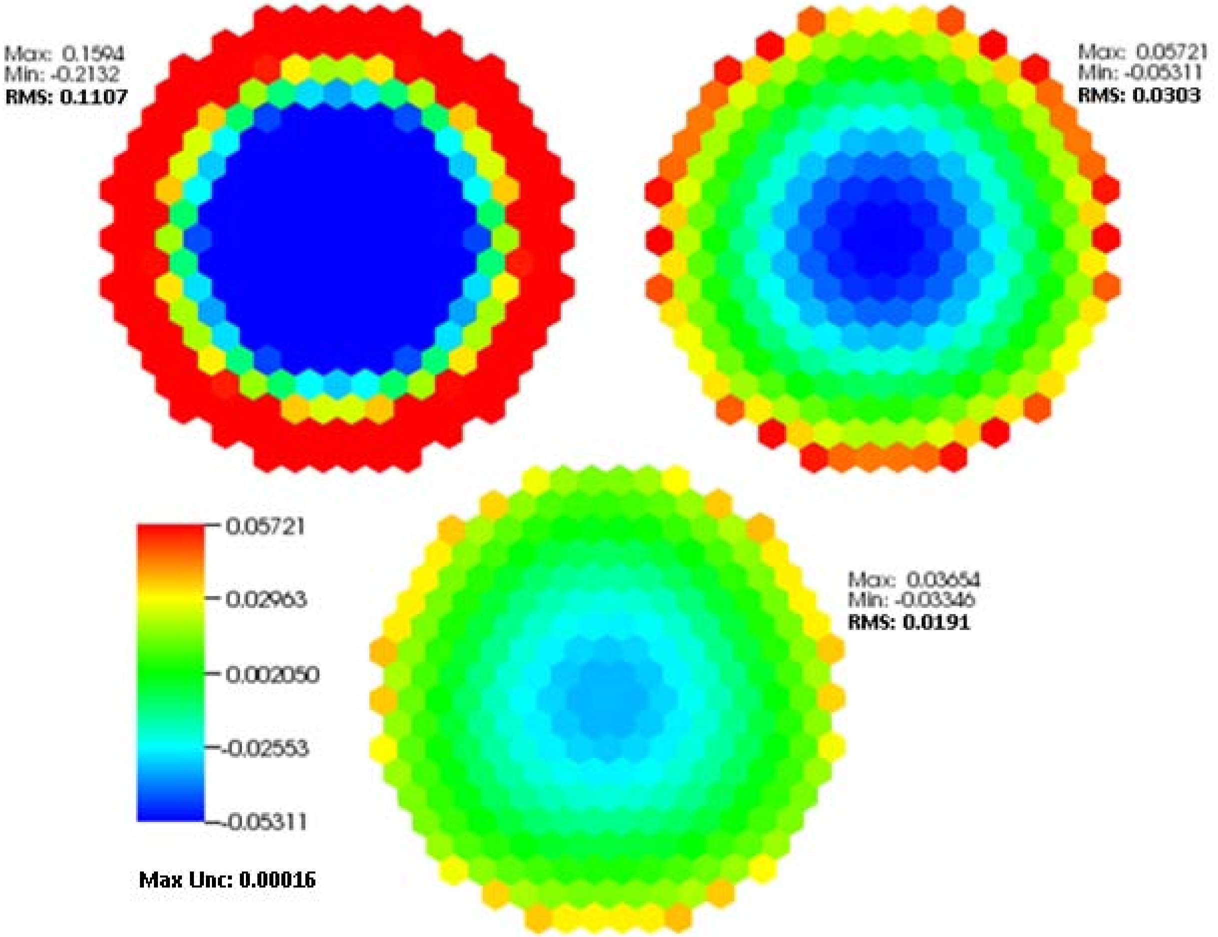

Figure 3-3 All Blades Out SERPENT 2 minus NESTLE 4-Group Option 1 (Top Left), NESTLE 4-Group Option 2 (Top Right), PARCS (Bottom) Relative Assembly Averaged Power Differences

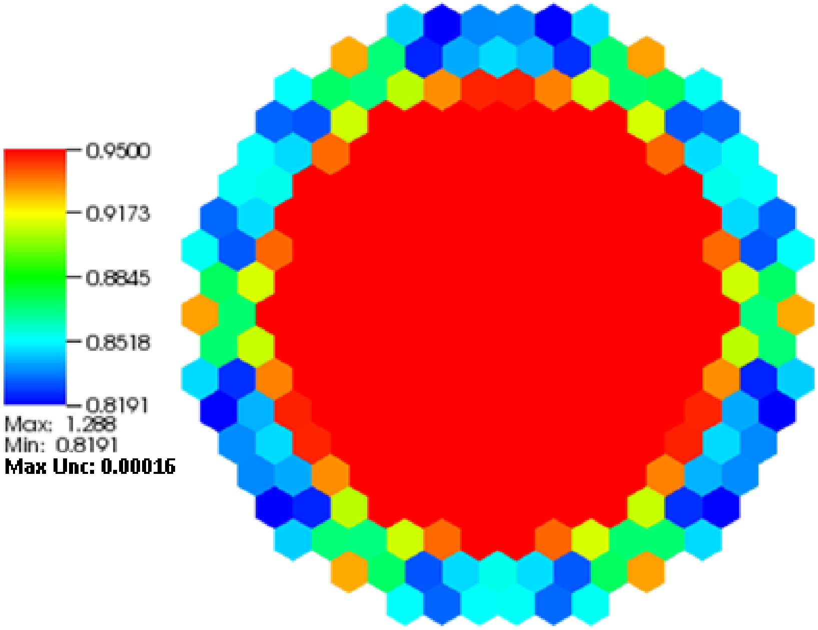

Figure 3-4 Illustration of SERPENT 2 Peripheral Power Peaking

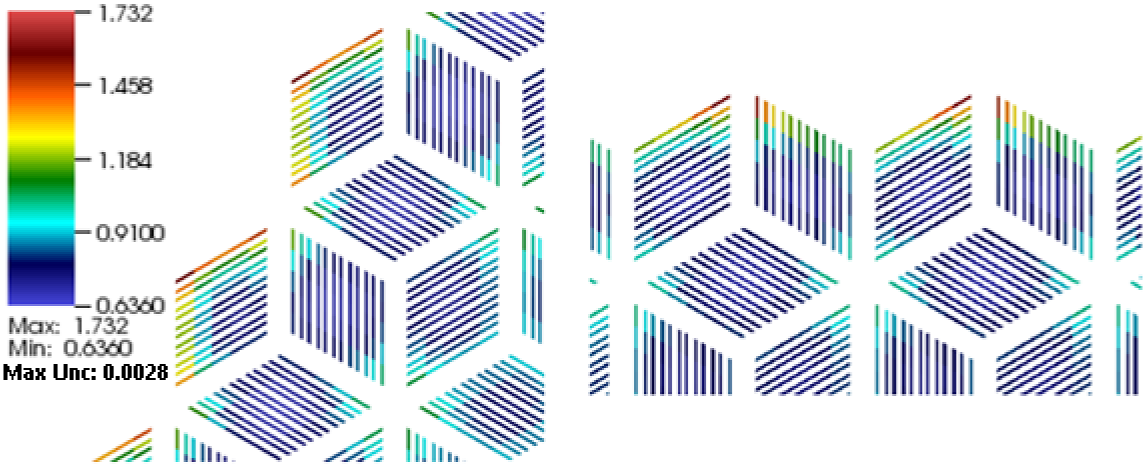

Figure 3-5 Plate Subdivision Power Peaking of Single Tri-Section Facing Reflector (Left) and Two Tri-Sections Facing Reflector (Right)

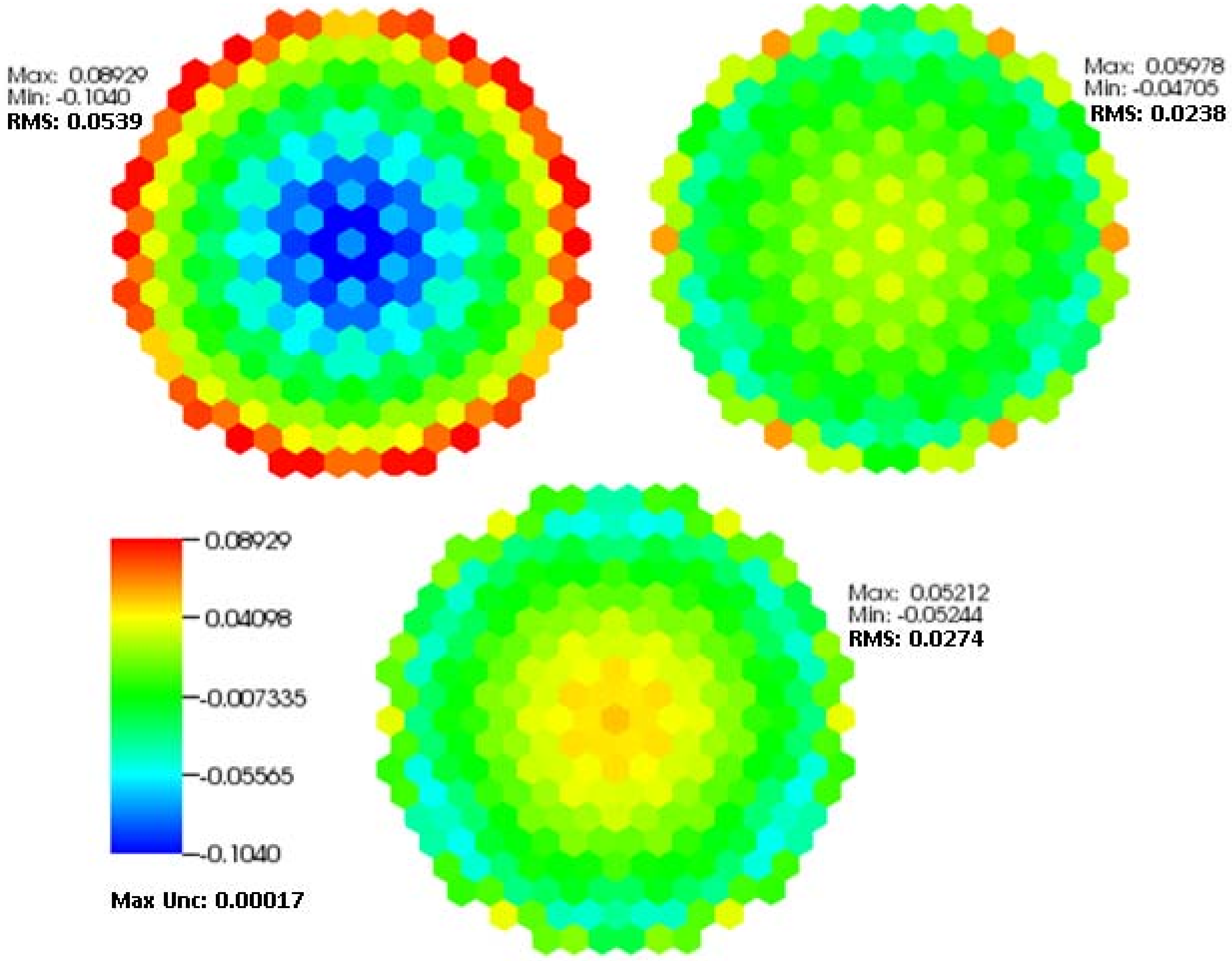

Figure 3-6 Assembly Averaged Relative Power Differences for Blades In Case. SERPENT minus NESTLE without Control Blade Reflector Adjustment (Top Left), NESTLE with Control Blade Reflector Adjustment (Top Right), and PARCs with Control Blade Reflector Adjustment (Bottom)

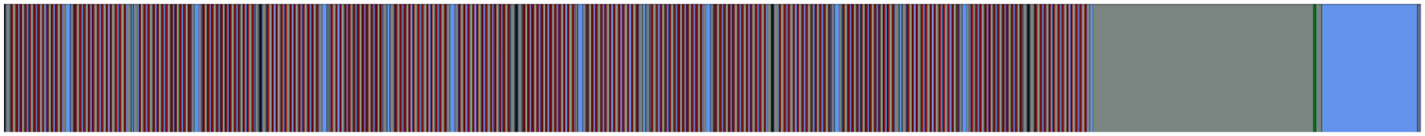

Figure 3-7 Illustration of Control Blade Semi 1-D Reflector Model

3.2. 3-D Benchmarking of two-step Procedure

After completing the 2-D full core assessmenst, the performance of the developed two-step procedure was evaluated for the modeling of 3-D full core models. Consistent with the 2-D evaluations, the 3-D cases were simulated for all blades out condition as well as the checker boarded fully inserted control blade conditions, both. For the control blades withdrawn case, NESTLE and PARCs demonstrated very good eigenvalue agreement with the reference SERPENT 2 model to within 102 ± 0.4 pcm and 127 ± 0.4 pcm, respectively. As can be seen in Figure 3-8 and Figure 3-9, power distribution agreement is also reasonable with maximum nodal differences of less than 10% and RMS error less than 3.5% for NESTLE and maximum nodal differences less than 7% and RMS error less than 2.6% for PARCS. It should be noted that axial averaged power distribution agreements appear excellent for both NESTLE and PARCS, and that the nodal power differences look to be dominated by tilts induced by the previously observed radial inaccuracies.

For the checker boarded fully inserted control blade model, only a NESTLE simulation was conducted due to difficulties encountered in obtaining a converged result with PARCS. Looking at Figure 3-10 and Figure 3-11 it can be seen that a better power distribution agreement was obtained between NESTLE and SERPENT 2 for the bladed caes, with maximum nodal differences less than 7%, RMS error less 2.7%, and axially averaged power distributions in near perfect agreement. Eigenvalue agreement of this model was within 127 ± 0.4 pcm.

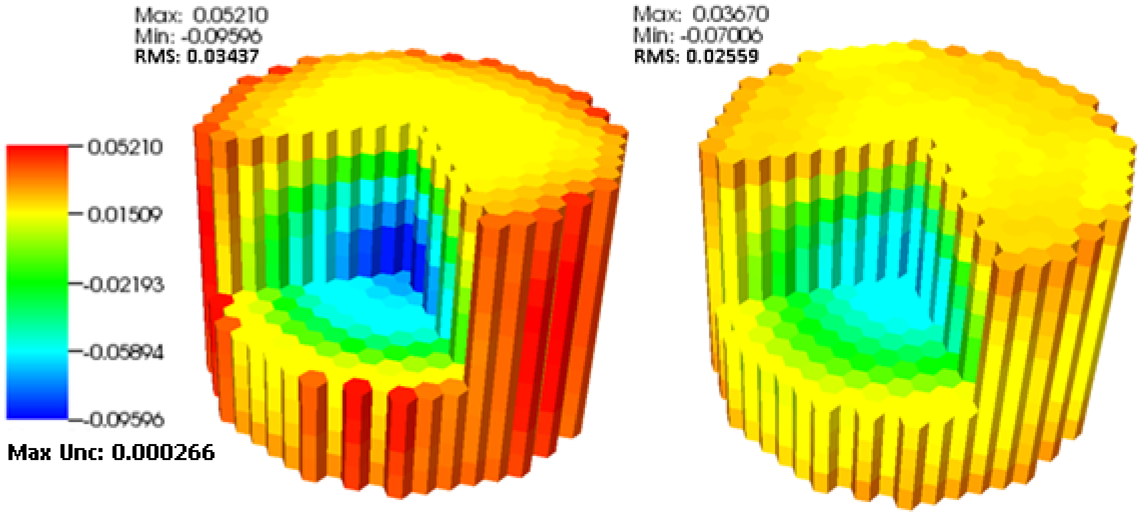

Figure 3-8 SERPENT 2 minus Core Simulator Relative Node Averaged Power Distribution Differences for 3-D Full Core with Control Blades Withdrawn for NESTLE (Left) and PARCs (Right)

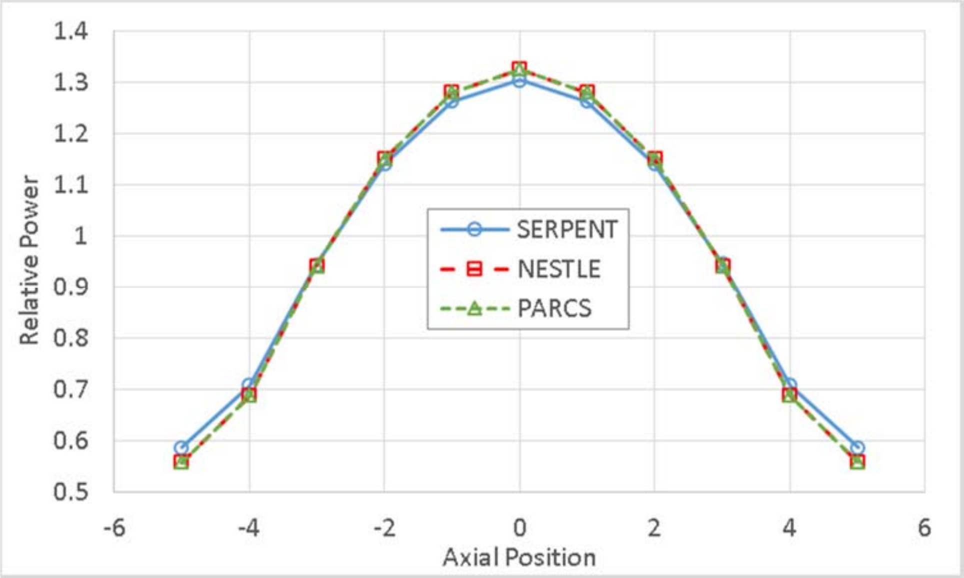

Figure 3-9 Radially Averaged Axial Power Distribution for 3-D Full Core with Control Blades Withdrawn

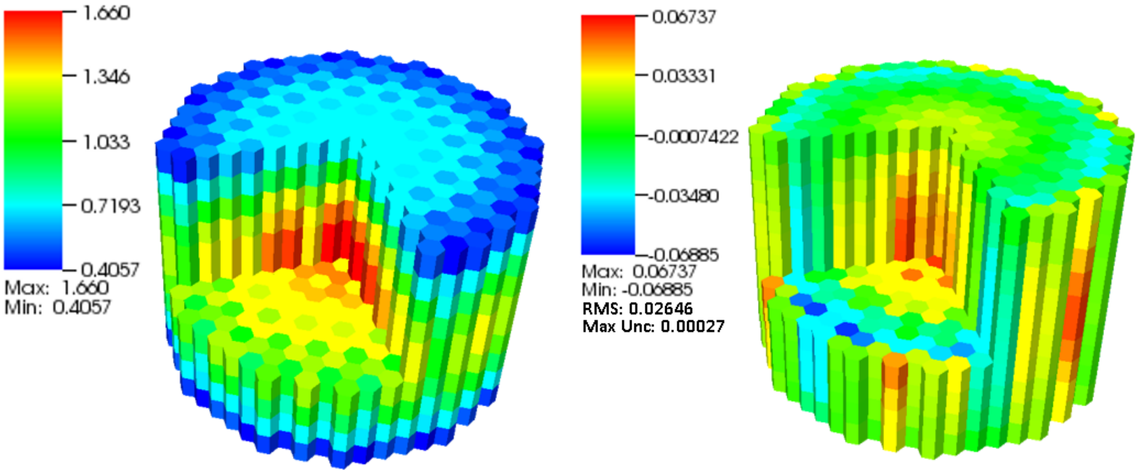

Figure 3-10 3-D Full Core with Control Blades Inserted NESTLE Relative Power Distributions (Left), SERPENT 2 minus NESTLE Node Averaged Power Distribution Differences (Right)

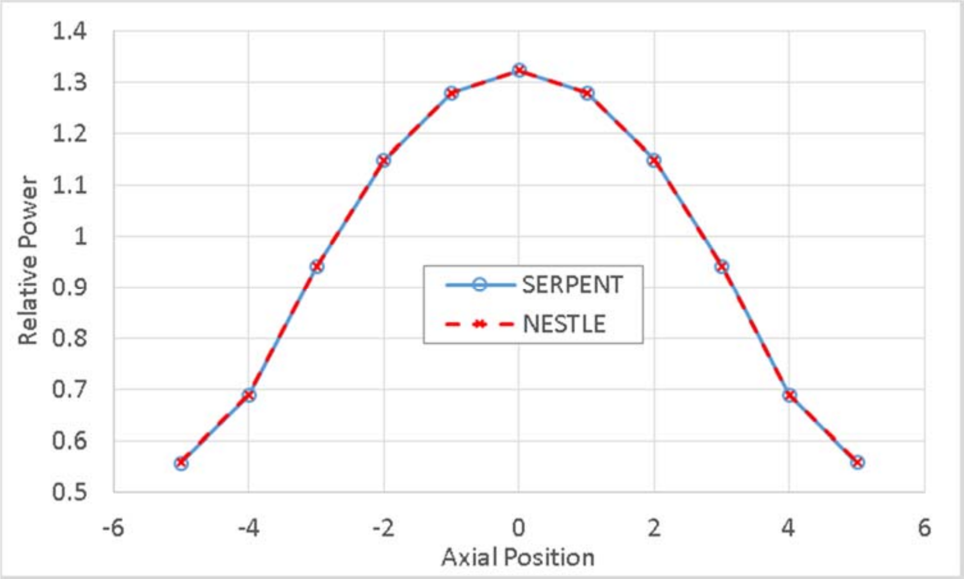

Figure 3-11 Radially Averaged Axial Power Distribution of 3-D Full Core with Control Blades Inserted

3.3. 3-D Coupled Neutronic and Thermal Hydraulic Depletion Demonstration

All previous calculations performed with NESTLE within the previous benchmarking sections were forced to run without thermal hydraulic feedbacks so to be able to compare to the SERPENT models. Though no formal benchmarking of the neutronics and thermal-hydraulic coupled model could be conducted --because there is simply nothing to compare to-- an illustrative NESTLE simulation is herein presented for demonstration purposes of the final product generated by this research project.

A reactivity curve can be observed in Figure 3-12 along with other metrics of interest shown in Figure 3-13 and Figure 3-14. Looking at Figure 3-13 it can be seen that all metrics tend to follow expected behaviors for the uniform core loading model that was used. Power and fuel temperature begin centrally peaked at beginning of cycle but gradually flatten as the fuel is burned out. Coolant density decreases as it flows from the bottom of the core to the top and fuel burnup proceeds from the inside out. As mentioned before, no formal testing of the coupled model was conducted due to time constraints and the lack of a practical means of provide a reference solution, but this demonstration does help to illustration the strength of the two-step method and provides a proof of principle and stepping stone for future research

The 3-D coupled calculation herein illustrated employed 24 depletion state points to model the AHTR fuel cycle. These results were generated on a single Intel Core i7 4770 Haswell processor in 21 minutes of wall-time (e.g. less than a minute per state point). In contrast, a single state point neutronic simulation of an equivalent model using SERPENT 2 and without thermal hydraulic feedbacks required 1.24 hours of wall clock time when using 1200 nodes with 16 core AMD Opteron processors each, or 19,200 processors of the ORNL TITAN supercomputer. Considering that multiple T/H iterations will be required to converge on a coupled solution for each state point, it can be said that obtaining a similar solution would take days or even weeks on a state-of-the-art high performance platform. Therefore, implementation within a typical modern cluster with a few hundred processors can be readily deemed as intractable.

In short, this easily demonstrates the utility of the two-step procedure in that it provides a coupled solution with substantially less runtime and resource requirements. It should be noted that when considering the cost savings of the two-step procedure, one should also consider the upfront computational costs of generating the lattice physics cross-section libraries. For this particular demonstration, models were simulated for the 7 branch conditions listed in Table 2-8 with both control blades inserted and withdrawn over 24 burnup points, totaling 336 state-point calculations. These simulations were conducted over 15 nodes comprised of Intel Core i7 4770 Haswell processors, using all 4 cores on each processor, and were completed in 7.8 hours of wall clock time. It should be noted that these run times will increase as larger numbers of neutron histories and improved accuracies are pursued. Though the cross-section library generation computational cost is significant, it is dramatically dwarfed by the computational costs associated with obtaining a coupled solution with the aforementioned SERPENT 2 based approach. Additionally, this cross-section library can be utilized for simulating more than just the uniform fresh core depletion calculation provided in this demonstration, such as multi-batch heterogeneous burnup distribution simulations. It can easily be seen then that with a few somewhat computationally expensive cross-section library generating simulations, one can perform a plethora of 3-D full core simulations at various conditions and core loadings at essentially negligible computational costs.

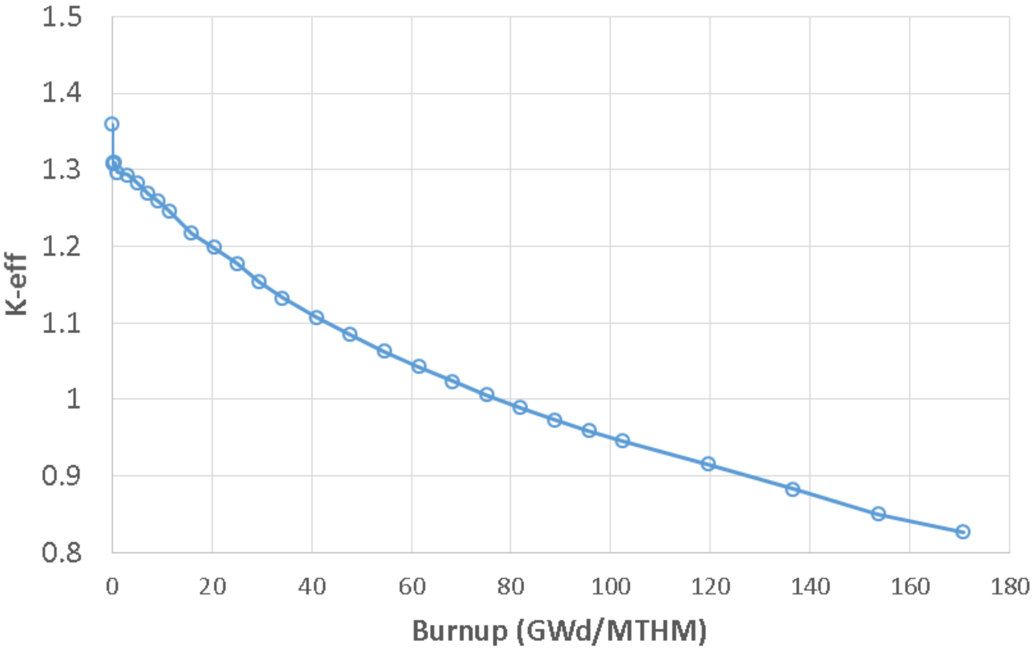

Figure 3-12 K- effective Profile for Illustrative Coupled Neutronic and Thermal Hydraulics AHTR Depletion Calculation in 3-D with NESTLE

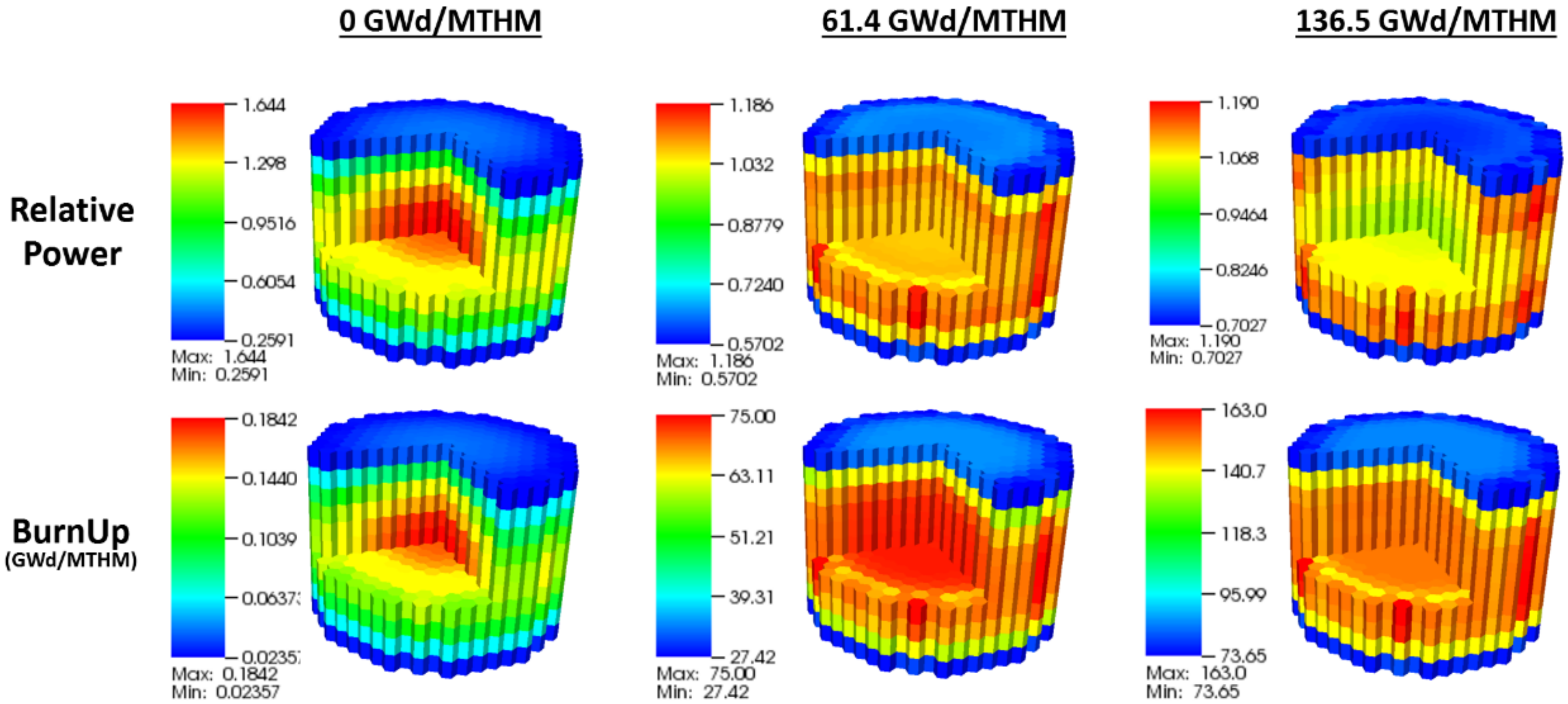

Figure 3-13 3-D Relative Power and Burnup Distributions for Coupled Neutronics and Thermal Hydraulic AHTR Deplection Calculations with the Two-Step Procedure

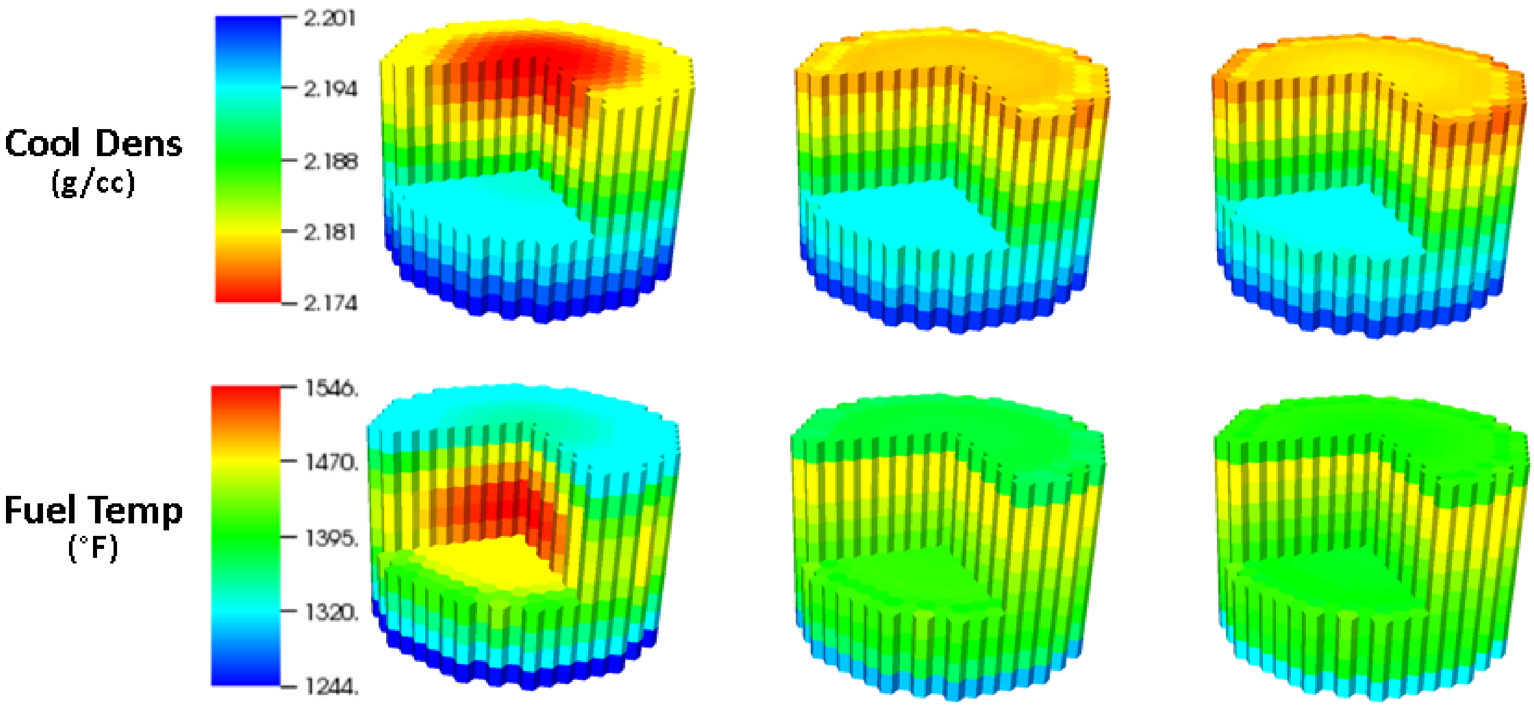

Figure 3-14 3-D Coolant Density and Fuel Temperature Distributions for Coupled Neutronics and Thermal Hydraulic AHTR Deplection Calculations with the Two-Step Procedure

4. Conclusions and Future Work

In this work a Two-Step procedure was developed for the AHTR so as to afford a means for strongly coupled neutronics and thermal hydraulic simulations currently absent in the reactor physics area. This leads the way to performing fuel cycle, core/assembly design, and safety margin assessments for steady state and slow transient conditions. Additionally, this procedure greatly reduces the computational expense of performing such simulations so as to allow for a means of expedient design optimization.

As part of this development, a means of performing accurate lattice physics for few group constants generation was established by using the SERPENT 2 continuous energy Monte Carlo code. It was found that TRISO particles could be treated explicitly as either random dispersion or regular lattice arrangements as well as with partial and entirely homogenized coating layers with comparable levels of accuracy. Five depletion regions per fuel stripe was shown to provide sufficient depletion resolution so as to be equivalent to finer stripe subdivision. Neutron transport simulations were shown to be sufficiently accurate such that photo-nuclear coupling could be deemed unnecessary. Upon establishing the lattice physics model, codes were then developed to extract the relevant output from SERPENT 2 and functionalize it into the polynomial form used by the NESTLE 3-D nodal simulator.

The Two-Step few group structure was analyzed using a select number of representative 1-D mini-core cases and optimized to ensure the accuracy of the infinite single assembly approximation. This was accomplished by both means of a deterministic algorithm, which provided a 13-group structure, and manual manipulation which resulted in a 4-group structure with similar reaction rate accuracy. A 1-D full core model and 3-D infinite single assembly model were used to generate radial reflector and axial reflector / coolant few-group constants which were subsequently adjusted by the interface ADFs to remove the need for tracking ADFs in the final full core models. The applicability of the ADF adjustment approach was also assessed and found to be sufficiently valid for the expected operating conditions with the exception of the control blade inserted case. This case was specially addressed with an additional radial ADF correction between controlled and uncontrolled assemblies organized in a checkerboard arrangement.

The finalized AHTR Two-Step procedure was then benchmarked using comparisons between core simulator and reference high fidelity Monte Carlo models of 2-D and 3-D uniform fresh cores with control blades fully withdrawn and fully inserted in a checkerboard arrangement. In these benchmarks, good agreement was obtained with regards to model eigenvalue and assembly power distribution. For the NESTLE core simulator 2-D and 3-D full core models, eigenvalue agreement was within 130 pcm and power distribution errors within 3.5% RMS error. However an underlying weakness was discovered in the validity of the radial uniformity assumption of the 1-D ADF adjustment of the radial reflector cross-sections which should be addressed in future development of this Two-Step procedure. Finally, a neutronic and thermal hydraulic coupled 3-D full core depletion model was simulated using the completed Two-Step procedure which demonstrated the functionality of the current procedure and its overall utility in reducing resource requirements.

With regards to expanding on the work herein presented, the following items are suggested as the focus of future work:

1. Further optimization of the few-group energy group structure

   Due to the limitations of NESTLE, the few-group energy group structure was limited to only 4 energy groups. Though the energy group structure presented herein is believed to be fairly well optimized for 4 energy groups, it is believed that much improved accuracy could be obtained with additional energy groups in the few group structure as well as further manual manipulation of the group boundaries with consideration for both the infinite assembly approximation accuracy and homogenized reflector accuracy. Ongoing development of an N-Group version of NESTLE will ultimately facilitate exploring the utility of using a greater number of energy groups.

2. Improvement of the reflector model so as to capture the underlying 1/3 azimuthal periodic power shift

   The reflector model considered in this study, though fairly computationally inexpensive due to its simplified core representation, is unable to precisely represent core azimuthal asymmetries, such as the underlying 1/3 azimuthal periodic power shift, due to its azimuthal uniformity assumption. This may be addressed in future works by considering 2-D whole core models for reflector cross-section generation. In these 2-D models, one could edit multiple azimuthal reflector regions for cross-sections and in this way capture the non-uniform azimuthal effects. Additionally, since a 2-D representation can provide a means for editing ADFs for all 6 faces of a hexagonal reflector node, one could treat the ADFs explicitly in the core simulator rather than by means of a cross-section adjustment. This explicit treatment of the ADFs may also help in accurately representing any non-uniformities that may be present in the full core model.

3. Implementation of plate power reconstruction

   Though plate power reconstruction is not thought to be essential for limiting safety performance evaluations, it would still prove useful in performing more accurate assessments of fuel utilization, isotopic tracking, and design optimization. SERPENT 2 provides the means of defining tallies with which to calculate form factors, but these tallies must be converted into a format usable by the core simulator which has yet to be done. Additionally, depletion region subdivision resolution may need to be further investigated to determine what level of subdividing may be needed to ensure stripe-wise power distribution convergence.

4. Establishment and Optimization of realistic batch-based AHTR fuel cycles

   The final item suggested for future development is the establishment and optimization of batch-based multicycles for realistic AHTR operation. Defining the specific fuel, core, and control blade management characteristics that would provide a path to licensing and operational management of a future AHTR. For this purpose, adaptation of multicycle optimization tools such as BWROpt [66] will prove to be extremely helpful to accomplish this task.

References

1. D.E. Holcomb, D. Ilas, V.K. Varma, A.T. Cisneros, R.P. Kelly, J.C. Gehin, “Core and Refueling Design Studies for the Advanced High Temperature Reactor”, Oak Ridge National Laboratory, ORNL/TM-2011/365, September 2011

2. V.K. Varma, D.E. Holcomb, F.J. Peretz, E.C. Bradley, D. Illas, A.L. Qualls, N.M. Zaharia, “AHTR Mechanical, Structural, and Neutronic Preconceptual Design”, Oak Ridge National Laboratory, ORNL/TM-2012/320, September 2012

3. H. Finnemann, F. Bennewitz, M.R. Wagner, “Interface Current Techniques for Multidimensional Reactor Calculations”, Atomkernenergie, **30**¸ pg. 123-128, 1977

4. K. Koebke, “A New Approach to Homogenization and Group Condensation”, IAEA Technical Committee Meeting on Homogenization Methods in Reactor Physics, Lugano, Switzerland, November 1978.

5. K.S. Smith, “Spatial Homogenization Methods For Light Water Reactor Analysis”, Doctoral Dissertation, Massachusetts Institute of Technology, June 1980

6. L. Massimo, “Physics of High Temperature Reactors”, Pergamon Press Ltd., Oxford, 1975

7. S.M. Goldberg, R. Rosner, “Nuclear Reactors: Generation to Generation”, *American Academy of Arts and Sciences*, 2011.

8. “Technology Roadmap Update for Generation IV Nuclear Energy Systems”, OECD Nuclear Energy Agency, January 2014.

9. “A Technology Roadmap for Generation IV Nuclear Energy Systems”, U.S. DOE Nuclear Energy Research Advisory Committee, GIF-002-00, Dec. 2002

10. W.B. Cottrell, H.E. Hungerford, J.K. Leslie, J.L. Meem, “Operation of the Aircraft Reactor Experiment”, Oak Ridge National Laboratory, ORNL-1845, September 1955

11. M.W. Rosenthal, P.R. Kasten, R.B. Briggs, “Molten-Salt Reactors – History Status and Potential”, *Nuclear Applications & Technology*, **8**, pg 107-117, 1970

12. P.N. Haubenreich, J.R. Engel, “Experience with the Molten-Salt Reactor Experiment”, *Nuclear Applications & Technology*, **8**, pg 118-136, 1970

13. H.G. MacPherson, “The Molten Salt Reactor Adventure”, *Nuclear Science and Engineering*, **90**, pg 374-380, 1985

14. “1000 MW(e) Molten Salt Breeder Reactor Conceptual Design Study”, U.S. Atomic Energy Commission, Contract NO. W-7405-eng-26, 1972

15. J.R. Engel, H.F. Bauman, J.F. Dearing, W.R. Grimes, E.H. McCoy, W.A. Rhoades, “Conceptual Design Characteristics of a Denatured Molten-Salt Reactor with Once-Through Fueling”, Oak Ridge National Laboratory, ORNL/TM-7207, July 1980

16. G. Zhangpeng, J. Zhou, D. Zhang, K.S. Chaudri, W. Tian, G. Su, S. Qiu, “Coupled Neutronics / Thermal-Hydraulics for Analysis of Molten Salt Reactor”, Nuclear Engineering and Design, **258**, pg. 144-156, 2013

17. C.W. Forsberg, P.F. Peterson, P.S. Pickard, “Molten-Salt-Cooled Advanced High-Temperature Reactor for Production of Hydrogen and Electricity”, *Nuclear Technology*¸ **144**, pg 289-302, 2003

18. D.E. Holcomb, F.J. Peretz, A.L. Qualls, “Advanced High Temperature Reactor Systems and Economics Analysis”, Oak Ridge National Laboratory, ORNL/TM-2011/364, September 2011

19. D.T. Ingersoll, C.W. Forsberg, P.E. MacDonald, K.T. Clarno, C.W. Forsberg, J.C. Gehin, C.O. Slater, J.J. Carbajo, D.F. Williams, T.A. Taiwo, J.E. Cahalan, T.K. Kim, J. Sienicki, F. Szakaly, A. Moisseytsev, M. Farmer, F. Dunn, P.F. Peterson, E. Greenspan, H. Zhao, J. Ambrosek, “Trade Studies for the Liquid-Salt-Cooled Very High-Temperature Reactor: Fiscal Year 2006 Progress Report”, Oak Ridge National Laboratory, ORNL/TM-2006/140, February 2007

20. D.F. Williams, L.M. Toth, K.T. Clarno, “Assessment of Candidate Molten Salt Coolants for the Advanced High-Temperature Reactor (AHTR)”, Oak Ridge National Laboratory, ORNL/TM-2006/12, March 2006

21. D.T. Ingersoll, L.J. Ott, J.P. Renier, S.J. Ball, W.R. Corwin, C.W. Forsberg, D.F. Williams, D.F. Wilson, L. Reid, G.D. Del Cul, P.F. Peterson, H. Zhao, P.S. Pickard, E.J. Parma, “Status of Preconceptual Design of the Advanced High-Temperature Reactor (AHTR)”, Oak Ridge National Laboratory, ORNL/TM-2004/104, May 2004

22. S.R. Greene, J.C. Gehin, D.E. Holcomb, J.J. Carbajo, D. Ilas, A.T. Cisneros, V.K. Varma, W.R. Corwin, D.F. Wilson, G.L. Yoder Jr., A.L. Qualls, F.J. Peretz, G.F. Flanagan, D.A. Clayton, E.C. Bradley, G.L. Bell, J.D. Hunn, P.J. Pappano, M.S. Cetiner, “Pre-Conceptual Design of a Fluoride-Salt-Cooled Small Modular Advanced High-Temperature Reactor (SmAHTR)” Oak Ridge National Laboratory, ORNL/TM-2010/199, December 2010

23. M. Fratoni, E. Greenspan, “Neutronic Feasibility Assessment of Liquid Salt-Cooled Pebble Bed Reactor”, *Nuclear Science and Engineering*, **168**, pg 1-22, May 2011

24. “Fluoride-Salt-Cooled High Temperature Reactor (FHR) Materials, Fuels, and Components White Paper”, Department of Nuclear Engineering and Engineering Physics University of Wisconsin Madison, UCBTH-12-003, July 2013

25. "Deep-Burn Modular Helium Reactor Fuel Development Plan", General Atomics and Oak Ridge National Laboratory, GA-244-0-TRT-000167, ORNL/TM-2002/135, September 2002

26. R.D. Hunt, J.L. Collins, "Uranium kernel formation via internal gelation", Radiochimica Acta, **92**, pg 909-915 2004

27. S. Bresnick, "MHTGR Fuel Process and Quality Control Description," DOE-HTGR-90257, Rev. 0, General Atomics, September 1991

28. Yonghee Kim and Min Baek, "Elimination of Double Heterogeneity through a Reactivity-Equivalent Physical Transformation", *Proceeding of GLOBAL 2005*, Paper No. 548, Tsukuba, Japan, Oct 9-13, 2005

29. S.M. Lewis, “Simplified Core Physics and Fuel Cycle Cost Model for Preliminary Evaluation of LSCR Fueling Options”, Georgia Institute of Technology, Master’s Thesis, May 2014

30. A.K. Prinja, E.W. Larsen, D.G. Cacuci (ed.), “General Principles of Neutron Transport”, *Handbook of Nuclear Engineering*, **1**, pg. 427-542, Springer Science+Business Media LLC, 2010

31. M.B. Chadwick, M. Herman, P. Obložinský, M.E. Dunn, Y. Danon, A.C. Kahler, D.L. Smith, B. Pritychenko, G. Arbanas, R. Arcilla, R. Brewer, D.A. Brown, R. Capote, A.D. Carlson, Y.S. Cho, H. Derrien, K. Guber, G.M. Hale, S. Hoblit, S. Holloway, T.D. Johnson, T. Kawano, B.C. Kiedrowski, H. Kim, S. Kunieda, N.M. Larson, L. Leal, J.P. Lestone, R.C. Little, E.A. McCutchan, R.E. MacFarlane, M. MacInnes, C.M. Mattoon, R.D. McKnight, S.F. Mughabghab, G.P.A. Nobre, G. Palmiotti, A. Palumbo, M.T. Pigni, V.G. Pronyaev, R.O. Sayer, A.A. Sonzogni, N.C. Summers, P. Talou, I.J. Thompson, A. Trkov, R.L. Vogt, S.C. van der Marck, A. Wallner, M.C. White, D. Wiarda, P.G. Young, "ENDF/B-VII.1: Nuclear Data for Science and Technology: Cross Sections, Covariances, Fission Product Yields and Decay Data", Nuclear Data Sheets, **112**, pg 2887-3152, 2011.

32. Y.A. Chao, N. Tsoulfanidis, “Conformal Mapping and Hexagonal Nodal Methods - I: Mathematical Foundation”, Nuclear Science and Engineering, **121**, pg. 202-209, 1995

33. A. Jonsson, S. Grill, J.R. Rec, “Nodal Imbedded Calculation for the Retrieval of Local Power Peaking From Reactor Analysis”, Joint ANS/ENS international topical meeting on advances in mathematical methods for the solution of nuclear engineering problems; Munich, Germany 1981.

34. *Scale: A Comprehensive Modeling and Simulation Suite for Nuclear Safety Analysis and Design,* ORNL/TM-2005/39, Version 6.1, June 2011. Available from Radiation Safety Information Computational Center at Oak Ridge National Laboratory as CCC-785

35. J. Leppänen. "Serpent– a Continuous-energy Monte Carlo Reactor Physics Burnup Calculation Code", VTT Technical Research Centre of Finland. August 16, 2012

36. J. Leppänen, M. Pusa, T. Viitanen, V. Valtavirta, T. Kaltiaisenaho, “The Serpent Monte Carlo Code: Status, Development, and Applications in 2013”, Annals of Nuclear Energy, IN PRESS, September 2014

37. E. Fridman, J. Leppänen, “On the Use of the Serpent Monte Carlo Code for Few-Group Cross Section Generation”, Annals of Nuclear Energy, **38**, pg. 1399-1405, 2011

38. J. Ortensi, J.J. Cogliati, M.A. Pope, J.D. Bess, R.M. Ferrer, A.A. Bingham, A.M. Ougouag, “Deterministic Modeling of the High Temperature Test Reactor”, Idaho National Laboratory, INL/EXT-10-18969, June 2010

39. E. Fridman, J. Leppänen, “Revised Methods for Few-Group Cross Sections Generation in the SERPENT Monte Carlo Code”, PHYSOR 2012

40. E. Fridman, E. Shwageraus, “Modeling of SFP Cores with SERPENT-DYN3-D Codes Sequence”, Annals of Nuclear Energy, **53**, pg. 354-363, 2013

41. D. Calic, A. Trkov, M. Kromar, “Neutron Multigroup Homogenized Cross Section Determination with the Monte Carlo Method”, Ljubljana 2012

42. L.K. Ghasabyan, “Use of SERPENT Monte-Carlo Code for Development of 3-D Full-Core Models of Gen-IV Fast-Spectrum Reactors and Preparation of Group Constants for Transient Analyses with PARCS/TRACE Coupled System”, Master’s Thesis, KTH Engineering Sciences, Stockholm, Sweden 2013

43. E. Fridman, S. Duerigen, Y. Bilodid, D. Kotlyar, E. Shwageraus, “Axial Discontinuity Factors for the Nodal Diffusion Analysis of High Conversion BWR Cores”, Annals of Nuclear Energy, **62**, pg. 129-136, 2013

44. S. Canepa, M. Hursin, H. Ferroukhi, A. Pautz, “Preparation of Nuclear Libraries with Deterministic and Stochastic Methods for LWR Reflectors”, M&C 2013

45. M. Hursin, A. Vasiliev, H. Ferroukhi, A. Pautz, “Comparison of SERPENT and CASMO-5M for Pressurized Water Reactors Models”, M&C 2013

46. A. Hall, Y. Xu, A. Ward, T. Downar, K. Shirvan, M. Kazimi, “Advanced Neutronics Methods for Analysis of the RBWR-AC”, Transactions of the American Nuclear Society, **108**, 2013

47. J. Leppänen, R. Mattila, M. Pusa, “Validation of the SERPENT-ARES Code Sequence Using the MIT BEAVRS Benchmark – Initial Core at HZP Conditions”, Annals of Nuclear Energy, **69**, pg. 212-225, 2014

48. S. Baier, E. Fridman, S. Kliem, U. Rohde, “Extension and Application of the Reactor Dynamics Code DYN3-D for Block-Type High Temperature Reactors”, Nuclear Engineering and Design, **271,** pg. 431-436, 2014

49. E. Nikitin, E. Fridman, K. Mikityuk, “Solution of the OECD/NEW Neutronic SFR Benchmark with SERPENT-DYN3-D and SERPENT-PARCS Cody Systems”, Annals of Nuclear Energy, **75**, pg. 492-497, 2015

50. “NESTLE: Code System to Solve the Few Group Neutron Diffusion Equation Utilizing the Nodal Expansion Method (NEM) for Eigenvalue, Adjoint, and Fixed-Source Steady-State and Transient Problems,” Version 5.2.1, June 2003. Available from Radiation Safety Information Computational Center at Oak Ridge National Laboratory as CCC-641

51. A.T. Cisneros, D. Ilas, “Neutronics and Depletion Methods for Multibatch Flouride Salt-Cooled High-Temperature Reactors with Slab Fuel Geometry”, Nuclear Technology, **183**, pg. 331-340, September 2013

52. P.J. Pappano, T.D. Burchell, J.D. Hunn, M.P. Trammell, “A Novel Approach to Fabricating Fuel Compacts for the Next Generation Nuclear Plant (NGNP)”, Journal of Nuclear Materials, **381,** pg. 25-38, 2008

53. J.D. Hunn, R.A. Lowden, J.H. Miller, B.C. Jolly, M.P. Trammell, A.K. Kercher, F.C. Montgomery, C.M. Silva, “Fabrication and Characterization of Driver-Fuel Particles, Designed-To-Fail Fuel Particles, and Fuel Compacts for the US AGR-3/4 Irradiation Test”, Nuclear Engineering and Design, **271**, pg. 123-130, 2014.

54. R.N. Morris, P.J. Pappano, “Estimation of Maximum Coated Particle Fuel Compact Packing Fraction”, Journal of Nuclear Materials, **361**, pg. 18-29, 2007

55. C. Liang, W. Ji, "A Novel Extension of Chord Length Sampling Method for TRISO-Type Applications", *Trans. Am. Nucl. Soc.*, **107**, pp. 551-553, 2012

56. J. Leppänen, M. DeHart, "HTGR Reactor Physics and Burnup Calculations Using the Serpent Monte Carlo Code" *Trans. Am. Nucl. Soc.* **101**, 2009

57. W. Ji, "Neutronics Analysis of Stochastic Distribution of Fuel Particles in Very High Temperature Gas-Cooled Reactors", Dissertation, *University of Michigan*, 2008

58. R. Sanchez, "Renormalized Treatment of the Double Heterogeneity with the Method of Characteristics", *PHYSOR* 2004

59. T. Goorley, et al., "Initial MCNP6 Release Overview", *Nuclear Technology*, **180**, pp 298-315, Dec 2012

60. "K.S. Kim, J.Y. Cho, H.C. Lee, J.M. Noh, S.Q. Zee, "Development of a Physics Analysis Procedure for the Prismatic very High Temperature Gas-Cooled Reactors", Annals of Nuclear Energy, **34**, pg. 849-860, 2007

61. K.S. Kim, "KARMA 1.2 Code User's Manual", S06NX08-A-2-TR-08, Korea Atomic Energy Research Institute, 2011

62. C.B. Davis, "Implementation of Molten Salt Properties into RELAP-3-D/ATHENA", Idaho National Engineering and Environmental Laboratory, INEEL/EXT-05-02658, 2005

63. M.S. Sohal, M.A. Ebner, P. Sabharwall, P. Sharpe, "Engineering Database of Liquid Salt Thermophysical and Thermochemical Properties", Idaho National Laboratory, INL/EXT-10-18297, 2010

64. P. Avigni, "Thermal Hydraulic Modeling of the Advanced High Temperature Reactor for the Evaluation of Steady State and Transient Conditions", Politecnico Di Milano, Master's Thesis, 2012

65. Y. Xu, V. Seker, "PARCS v3.0 U.S. NRC Core Neutronics Simulator", Department of Nuclear Engineering and Radiological Sciences University of Michigan, UM-NERS-09-0001, Dec. 17, 2014

66. K. Ottinger and G. I. Maldonado, "BWROPT: A Multi-Cycle BWR Fuel Cycle Optimization Code," Nuclear Engineering and Design, **291**, pg. 236-243, Sep. 2015

Vita

Cole Gentry was born April 30, 1985 in Chattanooga, Tennessee. Cole attended the Notre Dame High School in Chattanooga and graduate in May of 2003. Cole then attended the University of Tennessee in Knoxville where he studied Nuclear Engineering. During his undergraduate career, Cole worked several semester as an intern with the Tennessee Valley Authority (TVA) in the Nuclear Fuels Design group at the Chattanooga corporate offices, as well as the Balance of Plant and Reactor Engineering groups at the Sequoyah Nuclear Facility. Cole graduated May 2008 Summa Cum Laude and was one of four recognized as top undergraduates in the College of Engineering.

After graduating, Cole went to work as a Reactor Engineer at the TVA Sequoyah Nuclear Facility for two years before deciding to return to academia to pursue his Ph.D. Whilst in graduate school, Cole was introduced to his future wife Ashley whose father can be credited with stumping Cole with questions concerning the Uranium Pu-36 Space Modulator. After marriage, Cole and Ashley were blessed with the birth of their first son Kyle who not only brought great joy and happiness to their lives, but also served as a reminder to Cole of the importance of graduating.

In December 2015, Cole successfully defended his dissertation and has taken a position at the Oak Ridge National Labs where he wishes to continue his endeavors in the progression of nuclear engineering.